University of Catania
Ph.D. Course in Physics - XXVII cycle

Seweryn Morawiec

Self-assembled Plasmonic Nanostructures for Thin Film Photovoltaics

Doctoral Thesis

Tutor: Prof. Francesco Priolo
Supervisor: Dr. Isodiana Crupi
Coordinator: Prof. Francesco Riggi

”We can’t solve problems by using the same kind
of thinking we used when we created them.”
∼Albert Einstein

Contents

Abstract

The aim of this thesis is to explore the optical properties of localized surface plasmon resonance sustained by self-assembled metallic nanoparticles (NPs) for the light trapping application in thin film photovoltaics (PV).

In the first chapter an overview of topics from photovoltaics (PV) and plasmonics is presented serving as a background for the experimental studies described in the following chapters. First, a big challenge to balance rapidly growing global energy demand with the environmental protection and the essential role of renewable energy sources, in particular the capability of photovoltaics to provide safe and clean electricity of the future, is discussed. Among different technologies, thin films solar cells have a potential to increase the competitiveness of PV through a substantial reduction of the manufacturing cost. However, an essential step it to develop an efficient, reliable and inexpensive light trapping scheme in order to maximize absorption of the near-infrared radiation in the cell and balance the reduced volume of semiconductor material. Recently there is a growing interest in the application of subwavelength metallic NPs for light trapping as they can scatter light efficiently over a broad wavelength range of the solar spectrum, due to the to the phenomena known as localized surface plasmon (LSP) resonance, with a theoretical possibility to exceed the classical $4n^2$ limit of geometrical optics.

The experimental study begins with a systematic investigation, presented in chapter 2, of the correlation between the structural and the optical properties of self-assembled silver nanostructures fabricated on soda-lime glass by a solid-state dewetting (SSD) process, which consist in thermally-induced morphology transformation from a thin film to an array of islands or nanoparticles. It is shown that four distinct types of morphology tend to form in specific ranges of fabrication parameters, which is quantitatively summarized by a proposed structural-phase diagram and allows to identify

the fabrication conditions in which preferable, uniformly spaced and circular NPs are obtainable. The optical properties of the NPs stay in qualitative agreement with the trends predicted by Mie theory, and correlate with the surface coverage (SC) distributions and the mean SC size. The applicability of such Ag NPs in solar cells, in terms of scattering efficiencies, is discussed. Finally, the structural and optical properties of NPs formed on and embedded in aluminium doped zinc oxide (AZO) are analyzed, revealing an asymmetry in optical response for front and rear-side illumination.

In chapter 3, the properties of self-assembled NPs incorporated on the rear side of thin silicon film in two distinct arrangements, namely superstrate and substrate, are investigated as a step forward towards the implementation in thin film photovoltaics. In the superstrate configuration, the structural properties of NPs formed on a-Si film, with various fabrication parameters and AZO spacer layers, are investigated and correlated to the absorption enhancement in silicon film. The coupling efficiency increases with NPs' average size, decreases with increasing distance between silicon, and is significantly smaller for spherical than for hemispherical NPs, which stay in qualitative agreement with theoretical predictions. A novel procedure, involving a combination of phothermal deflection spectroscopy and fourier transform photocurrent spectroscopy, employed for substrate configuration films allowed for the quantification of useful and parasitic absorption. It is demonstrated that the optical losses in the NPs are insignificant in the $500-730$ nm wavelength range, beyond which they increase rapidly with increasing illumination wavelength. Furthermore, a broadband enhancement of 89.9% of useful absorption has been achieved and attributed to both the random front surface texture, originated from the conformal growth of Si on top of the NPs, and to the scattering of light by the plasmonic NPs

The first part of this chapter 4 reports a successful implementation of a plasmonic light trapping scheme implemented in a thin film a-Si:H solar cell in plasmonic back reflector (PBR) configuration. The optical properties of the PBRs are systematically investigated according to the morphology of the self-assembled silver nanoparticles (NPs), which can be tuned by the fabrication parameters. By analyzing sets of solar cells built on distinct PBRs, it is shown that the photocurrent enhancement achieved in the a-Si:H light trapping window ($600-800$ nm) stays in linear relation with the PBRs diffuse reflection. The best-performing PBRs allow a pronounced broadband photocurrent enhancement in the cells which is attributed not only to the plasmon-assisted light scattering from the NPs but also to the front surface texture originated from the conformal growth of the cell material over the particles. As a result, remarkably high values of J_{sc} and V_{oc} are achieved in comparison to those previously reported in the literature for the same type of devices.

The last part of chapter 4 presents an attempt on implementation of the plasmonic light trapping in the industrial a-Si/μc-Si double junction solar cells. The effect of annealing on the electrical performance is tested, and reveal that the fill factor, and hence the efficiency, increases in moderate annealing temperatures. The implementation of metallic NPs resulted, however, in decrease of external quantum efficiency (EQE) due to the high parasitic absorption in the NPs and corrugated back reflector. The possible solutions allowing for desirable improvements are outlined.

Finally, a summary and future perspectives are presented.

Chapter 1

Introduction

In this chapter a broad overview of topics from photovoltaics (PV) and plasmonics is discussed, providing a solid background for the original results presented in the following chapters.

A major part of energy consumed today is supplied from combustion of fossil fuels, which due to the emission of green house gases have a strong negative impact on the global climate. As the demand for energy is growing rapidly driven by the continuous growth of world's population and development of economies, the big challenge is to balance energy needs with environmental protection. This can only be achieved by a large scale deployment of renewable energy sources, among which photovoltaics will play an essential role generating clean and safe electricity of the future.

Thin film solar cells have a potential to increase the competitiveness of PV through a substantial reduction of the manufacturing cost. However, an essential step it to develop an efficient, reliable and inexpensive light trapping scheme in order to maximize absorption of the near-infrared radiation in the cell and balance the reduced volume of semiconductor material.

Plasmonics, exploiting the resonant interactions of free electrons in metals with the electromagnetic radiation, gives a unique possibility to confine and control optical energy in the subwavelength scale. Metallic nanoparticles (NPs) in particular are capable to scatter light efficiently over a broad wavelength range of the solar spectrum, due to the phenomena known as localized surface plasmon (LSP) resonance, and thus can provide efficient light trapping in thin film solar cells, with a theoretical possibility to exceed the classical $4n^2$ *limit of geometrical optics.*

1.1 Energy challenge

Development of economies and societies has always been dependent on the consumption of energy, which is embedded in all kinds of goods, and is needed to produce any kind of service. In particular, the expansion of human civilization in the 20th century was enabled by the exploitation of fossil fuels and the wide availability of highly-concentrated and low-cost energy. The continuous growth of world's population combined with the desire to rise the standards of living is resulting in a rapid growth of the energy demand.

From the beginnings of the Industrial Revolution global population increased by almost a factor of 7, from 1 up to about 6.8 billions nowadays, and is projected to peak in 2050 at around 9 billions [1]. In the same period of time the average primary energy consumption rate increased by a factor of more that 20 reaching today's level of $\sim 15\,\mathrm{TW}$. As depicted in Fig. 1.1, currently over 80% of the energy used by the mankind is provided from combustion of fossil fuels, resulting in an enormous consumption of almost 1000 barrels of oil, 93000 cubic meters of natural gas and 221 tons of coal per second [2]. Though the shares of various energy sources in total primary energy supply shift over the years, the share of fossils remains almost unchanged, while the total consumption increases significantly, e.g. it doubled in the period 1973 - 2012. Projections of the current worldwide trends show further substantial grow of the energy demand. Unless significant new policies are enacted, the major part of energy will continue to be supplied from fossils. Although the conventional energy sources are not renewable and are going to exhaust one day, existing reserves of fossil fuels and uranium ore are, despite the common believes, sufficient to sustain the global energy demand for centuries [3], especially when the technological advances and exploitation of new unconventional sources, such as shale oil and gas, are taken into account [4]. An important additional aspect driving the supply of fuels, especially oil and gas, is an uneven allocation of reserves among the globe, which results in a number of economical and political constrains determining the level of production and pricing.

The consumption of fossil fuels on a massive scale implies emission of millions of tons[1] of green house gases (GHG), namely carbon dioxide (CO_2),

---

[1] The total emission of CO_2 from fossil fuel combustion in 2012 was at the level of $31,734\,\mathrm{Mt}$ (of which 43.9% from coal, 35.1% from oil, and 20.3% from natural gas) com-

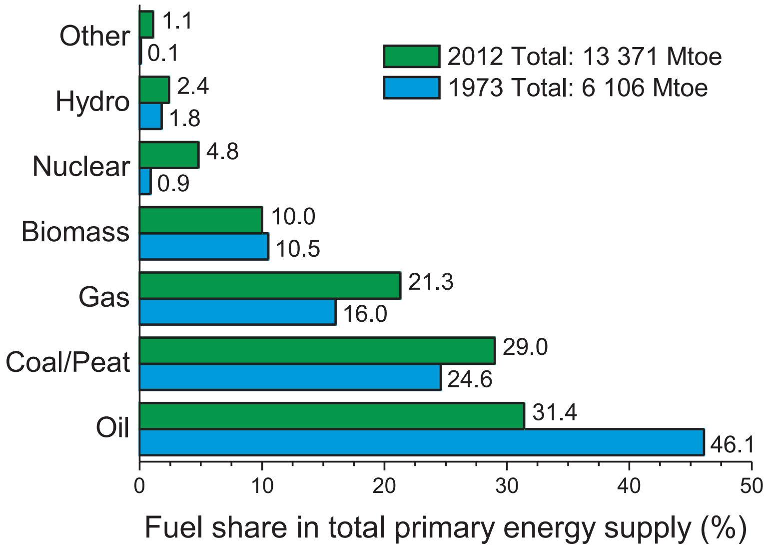

Figure 1.1: Share various sources in the total primary energy supply in 1973 and 2012 [5]. The total supply is given in units of metric tons of oil equivalent (toe) corresponding to 44.76 GJ.

methane (CH_4), and nitrous oxide (N_2O) per year. Nowadays their atmospheric concentrations greatly exceed the pre-industrial levels, for instance, as of 2010, the concentration of CO_2 increased from 275 ppm to 375 ppm. The GHG absorb and retain a part of solar radiation leading to the increase of the mean global temperature, which influences significantly the climate. The impact on the environments includes melting of Arctic ice and rising the sea level, acidification of the oceans, increased number of floods and droughts periods. Importantly, as of 2010 three-quarters of cumulative GHG emission took place after 1960, and thus most of human-induced climate changes start to be visible now. Stabilization of the GHG concentration in the atmosphere at acceptable levels requires immediate substantial reduction of the emission, meaning that the emission peak should occur in the next two decades [6]. Therefore, the big challenge is to provide sus-

---

pared to 15, 633 Mt of 1973 [5].

tainable energy for the developing world, meaning a sufficient supply with negligible long-term impact on the environment, both locally and globally.

As far as can be seen today, the energy challenge can only be met by a large scale deployment of various renewable energy sources: solar, wind, tides etc., which in comparison with today's needs have almost infinite potential. In particular, average total power arriving from the Sun to the Earth's surface, excluding reflection and absorption by the atmosphere and by clouds, is estimated at $\sim 96\,\mathrm{PW}$. Discounting the energy used by natural phenomena like the global water cycle (powered mostly by the infrared radiation), the atmospheric circulation, and energy captured by land and ocean vegetation to power photosynthesis, the mankind still have some thousands of times more energy that the current consumption to exploit [2]. Furthermore, unlike the conventional energy sources (fossil fuels, uranium ore) which are extremely concentrated and virtually absent in large areas of the planet, the solar energy is relatively fairly distributed. However, the main drawback of the solar radiation is its relatively low energy density, especially when compared with liquid fuels, which makes it impractical and economically unfavorable. Large scale incorporation of renewable technologies brings up several new technological issues, like energy storage or smart grids, being a consequence of day and year variations of produced power.

In conclusion, an extensive research on conversion technologies (photovoltaics, solar-thermal, solar fuels, artificial photosynthesis) is crucial to enable the cost-competitiveness of the solar energy with the conventional sources. As nowadays renewable technologies (with the exception of large-scale hydro-power) provide only a small fraction of about 1% of the total supply, a tremendous effort is necessary to deploy renewables on a meaningful scale and balance the future energy demands with environmental protection.

1.2 Photovoltaics

Photovoltaics has an enormous potential to become an essential energy sources of the future providing clean, safe and affordable electricity. Nonetheless, an intensive research aimed at the increase of conversion efficiency and the reduction of manufacturing costs is crucial to reach the grid parity and enable TW scale installation.

1.2.1 PV market - current status and future perspectives

Over the past decade, photovoltaics market has been growing at a remarkable rate (depicted in Fig. 1.2), starting from 1.3 GW of cumulative installed capacity in 2000 and reaching by the end of 2013 the level of 138 GW, which is equivalent of the electricity produced by 32 large coal power plants [7]. In the last years, PV, together with wind practically at the same rate, is the most exploited source of electricity in the EU. The current cumulative installed power of 81.5 GW covers about 3% of European electricity demand, which is sufficient for the needs of 26.5 million households, and contributes to the reduction of the mid-day peak demand by 6%. This is even more pronounced in the countries intensively investing in PV systems, i.e Italy, where the respective contributions reach the highest values in EU of 7.5% total and 15% of peak demand. Furthermore, after hydro and wind power, PV remains the third most important renewable energy source globally.

Although for the past years EU has been the world's leader in PV development, and still possesses the majority of over 59% of cumulative PV capacity, the rate of new installations clearly stagnated in 2012 and 2013. It should be noted, however, that the development is faster than previously expected, and many EU countries have already overtook the scenarios foreseen for 2020. With a steady growth and no major changes of policy, a share between 7% to 11% of PV in European electricity demand by 2020 appears realistic. In most countries, however, PV development remains driven by the national support schemes having a strong impact on the market and the industries. In fact, declining the support for PV resulted in the market stagnation in 2013 in several EU countries (i.e. Germany, Italy, Belgium), while the implementation of new feed-in tariff policies led to a remarkable increase of the markets in Asia (China and Japan). The European slowdown occurred simultaneously with the significant progress in Asian countries, which largely compensated and kept world's PV development on an upward trajectory. Currently, China and Japan are being ranked as the first two biggest global markets and the fast-growth trend is expected to continue in the next years [7].

Recently, the price of PV electricity for residential installations in several EU regions with high average annual irradiation has become competitive with the price of conventional power sources, as a result of both, steady increase of the conventional-electricity price and decrease of PV module costs [7]. This is an important step towards the real revolution of the global

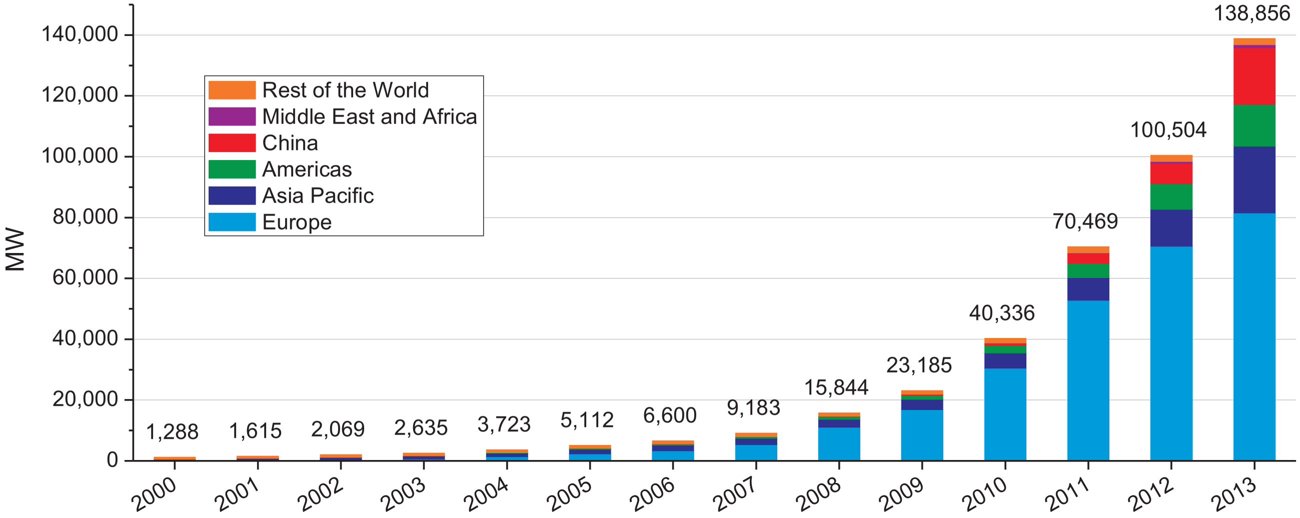

Figure 1.2: Evolution of the cumulative installed PV capacity, globally, in the years 2000 - 2013. Based on data from [7]

energy market and achievement of the TW challenge.

The Photovoltaic industry is currently in a transition from a MW scale to a mass-production scale aiming for hundreds of GW per year. The consolidation of industry together with the shift of main production sites to Asia resulted in a global overcapacity of PV modules, and thus, a big competition in terms of manufacturing costs, which in consequence led to the bankruptcy of many smaller companies over the last years. Nowadays, China, followed by Taiwan, has become the major manufacturing place for solar cells and modules [8].

1.2.2 Solar cell technologies

Development of PV is essentially focused on increasing efficiency, enhancing lifetime and reliability, and reducing material and manufacturing costs, in order to lower the energy payback time and to achieve grid parity by simply producing more energy for longer time at lower initial investment. However, several other aspects must be addressed for each PV technology once the TW scale is considered: (i) absorber material should be composed of elements with sufficient abundance, (ii) material should be processed easily, quickly and in low temperatures to assure high production throughput and low cost, (iii) the manufacturing technology itself should have low environmental impact in terms of energy usage, pollution and CO_2 emission.

PV technologies are often categorized into three groups, named after a terminology proposed by M. Green [9] first-, second-, and third-generation, accordingly to their efficiency and price per watt peak (1 Wp panel would produce 1 W under AM1.5 standardized conditions, see paragraph 1.2.3) as depicted in Fig 1.3.

First generation solar cells are primarily crystalline silicon (c-Si) and multicrystalline (mc-Si) single junction devices, with a thermodynamic efficiency limit $\sim 30\%$ under AM1.5 sunlight (see paragraph 1.2.3). Although real devices suffer from parasitic losses, record efficiencies are moving towards the theoretical limits with several up-to-date reports in the range of $24 - 25.6\%$ for cell and $21 - 23\%$ for modules [10]. This is a result of considerable improvements over simple p-n junction by advanced surface passivation, light trapping, antireflection coatings and heavily doped contact regions (e.g. Panasonic HIT cell 25.6% [11], PEARL cell 25.0% [12]). So far, the highest efficiencies of 28.8% for single-junction solar cell were achieved with gallium arsenide (GaAs) as a result of its direct bandgap,

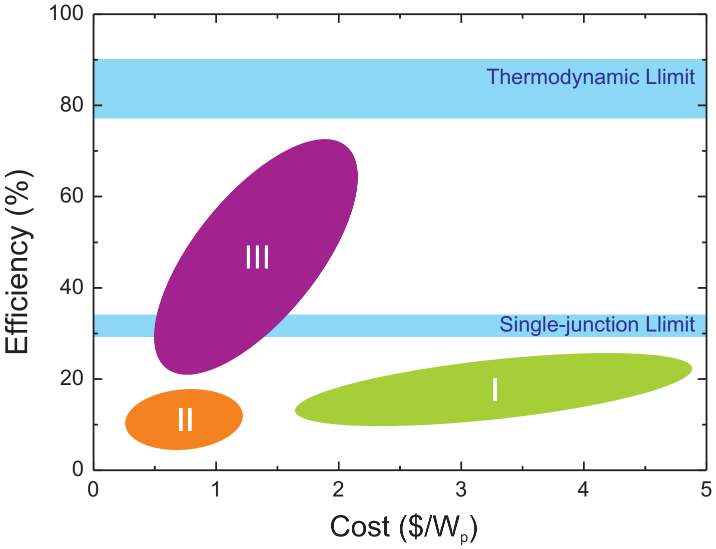

Figure 1.3: The categorization of PV technologies into first-, second- and third-generation, accordingly to their efficiency and price per watt peak ($/Wp). Based on [9]

hence high absorption, and a special solar cell design allowing for high improvements in the operating voltage [13].

The manufacturing cost of first-generation modules is, in general, decreasing linearly with cumulative global production as an effect of incremental technological improvements and economies of scale. Nonetheless, the final cost is highly dependent on Si feedstock and global economy. For example, a shortage of Si feedstock in 2005 stabilized the module prices against the cumulative production, while the economic downturn of 2008 together with increased c-Si supply drove module prices rapidly down to 1.5 $/Wp in 2010. Nonetheless, current prices evolving steadily towards 1 $/Wp are already lower than what was initially predicted for first-generation technologies. It has been argued though, that the contribution of c-Si wafers to the price of a module cannot be reduced indefinitely and prices should level off above 0.33 $/Wp in the next 10 years.

The second-generation solar cells are fabricated by large-area thin film deposition techniques on cheap foreign substrates, like glass, stainless steel, or even plastic. Even though reported efficiencies are notably lower than those of first-generation devices, elimination of the expensive single crystal substrates should bring an overall reduction of the payback-time. Up-to-date there are three well established, commercially available technologies based on hydrogenated amorphous and nanocrystalline silicon (a-Si:H/μc-Si:H), cadmium telluride (CdTe), and copper-indium-gallium selenide (CIGS) with maximum reported cell efficiencies of 13.4%, 19.6%, and 20.5%, respectively [10]. Furthermore, several emerging approaches, like organic compounds or perovskite materials, have evolved rapidly in the last years showing high potential. Nowadays, however, thin film technologies struggle to withstand the competition with the unexpectedly low price of c-Si modules dominating the PV market.

The next generation solar cells ought to combine the advantage of high efficiency and low production cost. A number of innovative concepts with theoretical efficiencies above 50%, usually intended to operate under highly concentrated sunlight, has been proposed [14]; among others this includes: spectral splitting, photon up- and down-conversion, III-V multi-junction cells, intermediate bandgap cells, extraction of hot carriers and thermal photovoltaics. Such high energy conversion efficiency is enabled by the nanofabrication techniques and exploitation of the quantum-confinement effects in semiconductor nanostructures [15]. First, the bandgap of nanocrystals and nanowires can be tuned across the visible and NIR range by their size and embedding matrix, therefore enabling perfect spectral matching between absorber and the sun spectrum. Second, the narrow bandgap semiconductor (e.g. PbS) quantum dots can be used to form an intermediate band states, in order to substantially extend the photoresponse of the cells towards NIR, while maintaining high operating voltage. Third, silicon nanocrystals can be employed to "reshape" the spectrum of sunlight in order to be more optimized, hence more efficiently converted, by the conventional single junction devices; this involves "cutting" of high-energy ultraviolet photons into multiple lower-energy ones (e.g. via space separated quantum cutting effect occurring in two coupled nonocrystals) and "pastig" together low-energy near-infrared photons (e.g. via absorption on free-carries producing hot carriers which can either be trapped and recombine radiatively at surface-related defect states, or emit photons through quantum cutting process). Nonetheless, currently most of the advanced concepts for third-generation

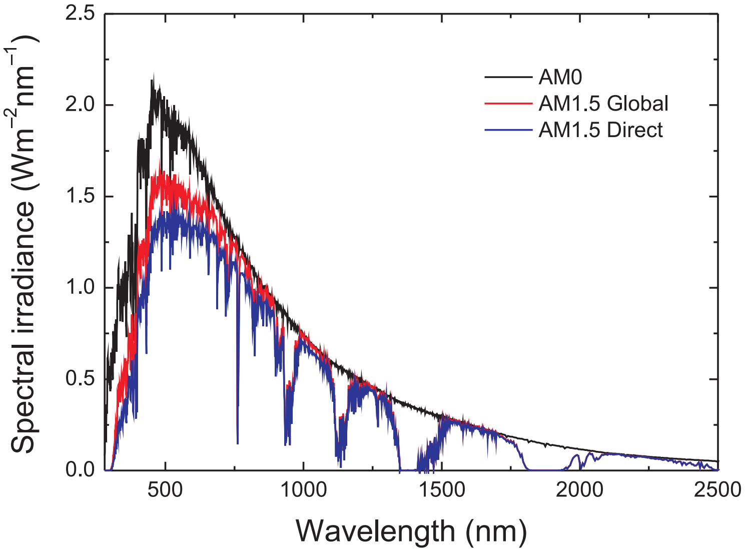

Figure 1.4: The spectral irradiance for extraterrestrial (AM0) and terrestrial global (AM1.5G) and direct (AM1.5D) solar radiation defined in the standard ASTM G173-03

photovoltaic devices are either at the basic research stage or due to the very high cost have limited applicability e.g. space technologies in the case of III-V devices.

In additions, the trends in PV development might not be, however, sufficient to meet the TW scale energy challenge, which requires breakthrough improvements of the cell performance and cost effectiveness.

1.2.3 Fundamentals of solar cell operation

Solar spectrum

The spectrum of electromagnetic radiation emitted by the Sun can be approximated with an emission from a perfect black-body at a temperature of 5780 K. Because the intensity of radiation decreases monotonically with the inverse square of the distance from the source, the irradiance just outside the Earth's atmosphere is estimated as $1,367\,\mathrm{Wm}^{-2}$. The actual spectral power density reaching the Earth's surface is attenuated by the scattering and absorption in the atmosphere and as such it depends on the latitude, time of the year, and chemical composition of the atmosphere. A convenient way to define solar radiation is the "Air Mass"[2] scale indicating the pathlength of extraterrestrial light through the atmosphere.

In order to allow for quantitative characterization and fair comparison among PV products, a standard of AM1.5 spectrum was developed by the PV industry and the American Society fo Testing and Materials (document ASTM G173-03). The standard defines spectral irradiances and photon fluxes above Earth's atmosphere (AM0) and at the 48.2° solar zenith angle with the distinction to the total radiation (AM1.5 Global) and the direct normal component only (AM1.5 Direct), depicted in Fig. 1.4. The AM1.5G spectrum entails a power flux of about $970\,\mathrm{Wm}^{-2}$.

Usable part of solar spectrum

The solar cell operation principle is given by the fact that the optical absorption of photons within any material involves an electronic transition from low energy occupied state to a high energy empty state, which in the case of semiconductors correspond to the generation of an electron-hole pair (e.g. for a molecular system this would correspond to a transition from HOMO to LUMO state). The photo-generated carriers can then be separated by the internal electric field, for instance from a p-n junction, to create a current. The thermodynamic principles, describing the intrinsic losses (i.e. Carnot efficiency) the ptotovoltaic energy conversion, define the ultimate limit of efficiency at about 86% [22]. Furthermore, the bandgap (E_g) of a semiconductor defines a threshold value for the energy of photons that can be absorbed within the material, and thus the maximum current obtainable from the solar radiation as a sum of photons with energy higher than the bandgap. At the same time, E_g determines also the maximum operating voltage of a solar cell, as all the energy of electrons excited with photons with photo-excited electrons higher than E_g is lost due to the thermalization process (electron-phonon interactions). The clear trade-off between the two effects is limiting the maximum efficiency of an ideal single-junction device to 42% [20] accessible in relatively broad bandgap range of 1.1 - 1.5 eV, which results from the fact that small drops of voltage are compen-

---

[2] Air Mass number, commonly used to refer to sun spectrum at different latitudes, is defined as: $\mathrm{AirMass} = 1/\cos\theta$, where θ is the angle of incidence towards the equator.

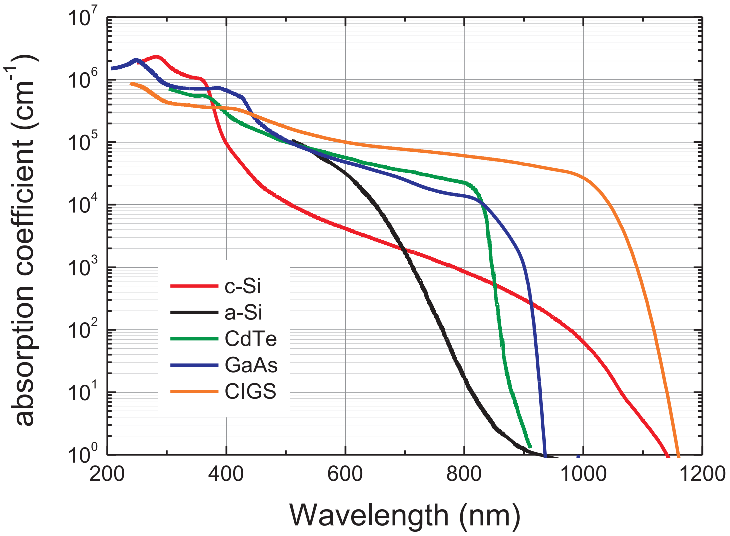

Figure 1.5: Absorption coefficients of different material used in phovotovoltaics. Data taken from Refs. [16] (c-Si), [17] (a-Si, CdTe), [18] (GaAs) and [19] (CIGS).

sated by the gain in current, and vice versa. This can be overcome, for example by increasing number of junctions made of materials with different bandgaps, leading to an effective splitting of the solar spectrum. The maximum achievable voltage from the solar cell is, however, determined by the separation of the electron and hole quasi-Fermi levels, being usually far below the bandgap energy because of the entropy losses due to the lack of emission angle restriction and incomplete light trapping. This decreases the efficiency limit down to 33.5% for a single junction solar cell with an optimum bandgap [20–22].

Basic operational parameters

Since a solar cell is essentially a diode, it can be modeled with a simple circuit shown in the inset of Fig. 1.6(a), consisting of a current source, due to light generated current, in parallel with a diode. With no illumination, the cell's current grows exponentially in forward voltage bias and saturates at small value in the opposite direction [23].

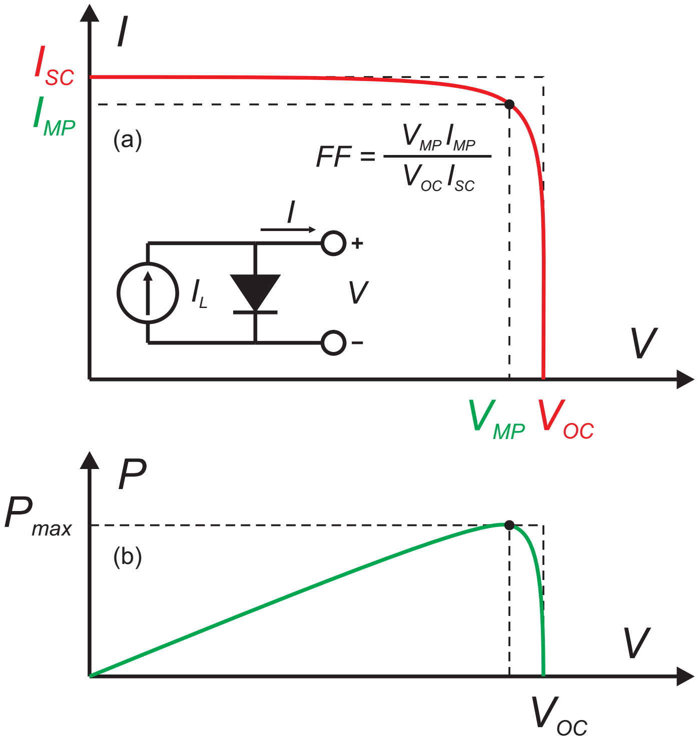

Figure 1.6: The current-voltage (I-V) and power-voltage (P-V) characteristics of illuminated solar cell showing basic operating parameters: short-circuit current (I_{SC}), open-circuit voltage (V_{OC}), maximum power (P_{max}) and fill factor (FF).

The current-voltage (I-V) characteristic of an ideal solar cell (photodiode) under illumination is depicted in Fig. 1.6(a). At small applied voltages, the diode current is negligible and the diode is dominated by the photo-induced current. When the applied voltage is high enough so that the diode current (recombination current) becomes significant, the solar cell current drops quickly since voltage is driving the current in the opposite direction. The relation is given by:

$$I = I_L - I_0(\mathrm{e}^{qV/nk_BT} - 1) \tag{1.1}$$

where I_L in the maximum current produced by the cell, I_0 is the dark saturation current, q is the elementary charge ($1.602 \times 10^{-19}\,\mathrm{C}$), k_B is the Boltzmann constant ($8.617 \times 10^{-5}\,\mathrm{eVK^{-1}}$), T is the temperature and n is the diode ideality (quality) factor. The I_L and I_0 are in general given by rather complex expressions that depend on the solar cell structure, material properties (i.e. carrier lifetimes), and the operating conditions. The n factor has typical values between 1 and 2, with $n \approx 1$ for diode dominated by recombination in the quasi-neutral regions and $n \to 2$ when recombination in the depletion region dominates.

The *short-circuit current* (I_{SC}) corresponds to the condition when the impedance of the load that the solar cell is driving is negligible. For an ideal device without parasitic resistances the I_{SC} equals the total current produced by photon excitation I_L.

Current produced by the cell is proportional to the amount of light-generated carriers and internal carrier collection efficiency. The collection efficiency depends on the material quality (minority carrier lifetime) and device structure (i.e. doping levels, thickness of each layers). On the other hand, the generation of photo-carriers depends on material absorption coefficient, reflection at the surface, shadowing by the contacts and other sources parasitic absorption. As such an important parameter describing the cell performance is the *external quantum efficiency* (EQE) defined as the ratio of number of electrons extracted from the cell to the number of incident photons impinging onto the cell. Once the EQE spectrum for a solar cell is measured, the I_{SC} can be calculated as its integral convoluted with an AM1.5 photon flux.

The *open-circuit voltage* (V_{OC}) is defined as the voltage across the solar cell when no current passes through ($I = 0$). This implies that the light-induced current is counter balanced by the opposite current driven by the voltage, which gives a logarithmic proportionality of V_{OC} to the I_L and to the reciprocal of the I_0:

$$V_{OC} = \frac{nk_BT}{q} \ln \frac{I_L + I_0}{I_0} \approx \frac{nk_BT}{q} \ln \frac{I_L}{I_0} \tag{1.2}$$

where $I_L \gg I_0$. Clearly, the V_{OC} is increased with the reduction of the saturation current, which decreases with increasing minority carrier lifetime and thus is proportional to non-radiative recombination, both in the bulk, through Auger and defect-mediated ShockleyReadHall (SRH) processes, and at the surfaces. In other words, high V_{OC} is obtainable when, in open circuit condition, all non-radiative recombination paths are suppressed and all photo-generated carries recombine radiatively, hence best

PV material is characterized by high radiation yield [21].

Of particular interest is the point on the I-V curve for which the power (P) produced by the cell and delivered to the load, plotted in Fig. 1.6(b), reaches the maximum value ($P_{max} = V_{MP}I_{MP}$). The two rectangular areas defined by $V_{OC}I_{SC}$ and $V_{MP}I_{MP}$ provide a convenient way of characterizing the maximum power point, by the *fill factor* (FF) parameter:

$$FF = \frac{V_{MP}I_{MP}}{V_{OC}I_{SC}} \tag{1.3}$$

The FF is also interpreted as a measure of the squareness of the IV curve and by definition has values lower than 1.

The most important figure of merit for a solar cell is its *power conversion efficiency*, η, which is defined as the ratio of the maximum electrical power output to the solar power input (P_{in}):

$$\eta = \frac{P_{max}}{P_{in}} = \frac{V_{OC}I_{SC}FF}{P_{in}} \tag{1.4}$$

The standard characterization conditions for solar cells are: illumination with AM1.5 spectrum and irradiance of $1\,\mathrm{kWm^{-2}}$, commonly referred to as "1 sun", in ambient temperature of 25°C.

Shunt and series resistance

Efficiency of the solar cells is reduced by the dissipation of power in the internal resistances, which can be modelled by a circuit with parallel shunt resistance (R_{SH}) and series resistance (R_S), shown in Fig. 1.7(a). The I-V curve is now given by the relation:

$$I = I_L - I_0\left(\exp\left(\frac{q(V + IR_S)}{nk_BT}\right) - 1\right) - \frac{V + IR_S}{R_{SH}} \tag{1.5}$$

For an ideal cell, R_{SH} would be infinite and thus does not provide and alternative path along which current could flow, whereas R_S would be zero giving no voltage drop before the load. The presence of parasitic resistances results in a significant decrease of the fill factor, and hence the efficiency. In general, decline of shunt resistance has no impact on the I_{SC}, but reduces the V_{OC}. On the contrary, the incline of series resistance has no effect on the V_{OC}, but reduces the I_{SC}. The effect of R_S and R_{SH} on the I-V curve

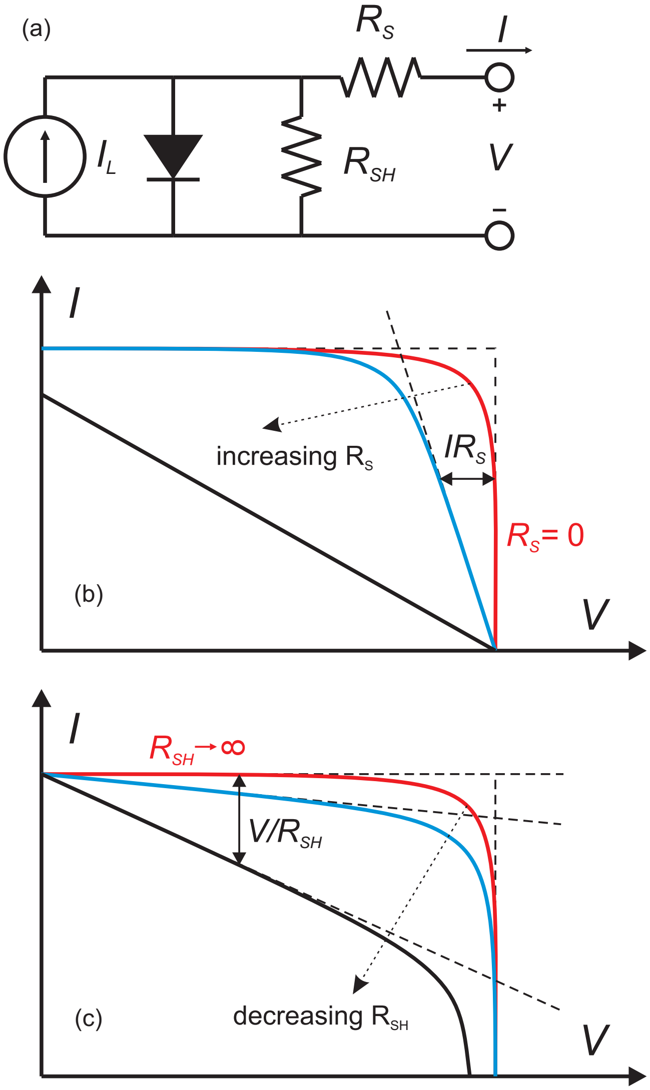

Figure 1.7: (a) Circuit model of a solar cells with parasitic resistances: parallel R_{SH} and series R_S; (b-c) The effect of R_S and R_{SH} on the I-V characteristic of a solar cell

is depicted in Fig. 1.7(b) and Fig. 1.7(c), respectively.

Main sources of R_S comes from the transverse flow of current in the solar cell to the metallic contacts, occurring either in the emitter layer or in transparent conductive oxide (TCO) contacts. The R_{SH} originates from the imperfections of the p-n junction allowing for the flow of current in the direction opposite to I_L.

1.2.4 Light trapping

One path to reduce the cost of solar cells is to minimize the amount of materials used for the fabrication by making the absorber layer thinner. This approach applies to both, traditional wafer based and thin film solar cells. However, as the absorption coefficient decreases significantly with increasing illumination wavelength, thin cells suffer from weak absorption of the near-bandgap photons (visible and UV photons are usually absorbed in the single pass through the device). This effect is especially pronounced in materials with indirect bandgap, like c-Si.

Nonetheless, the absorption can be greatly increased by applying effective *light trapping*. This means to force long-wavelength photons to travel, within the solar cell material, distances much longer than the actual device thickness, since the longer is the optical path length the higher is the probability of absorption. This is usually achieved by the scattering of incident light at the interfaces, either in transmission at the front surface or in reflection at the rear one, as shown schematically in Fig. 1.8 in the ray optics limit. In addition, when the angle at which light is scattered is equal or greater than the critical angle for total internal reflection ($\theta_c \approx 16°$ for the Si/air interface), the light can be coupled to the guided modes [24] and trapped within the absorber, unless a re-scattering event at the angle within the escape cone occurs before absorption.

The additional benefits of the lower volume of the semiconductor are: (i) the increase of V_{OC}, due to lower non-radiative recombination, and (ii) improved carrier collection efficiency due to the increased ratio between carrier diffusion lengths and the thickness of absorber. In case of a-Si:H based devices, reduced volume also results in decreased light-induced conductance degradation known as Stabler-Wronski effect. The trade-off between lower absorption and aforementioned beneficial effects results in the existence of the optimum thickness, at around $10\,\mu$m, to maximize the efficiency of c-Si solar cell with perfect light trapping [25]. In fact, an efficiency of 19% has

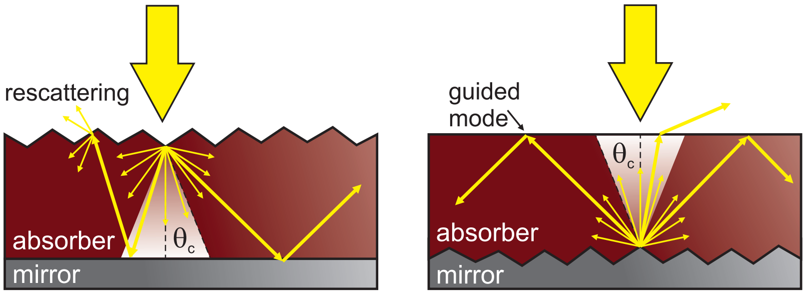

Figure 1.8: Schematic illustration of optical path length enhancement and coupling to the guided mode, within the ray optics regime, resulting from scattering of light at randomly textured front- and rear interface.

recently been achieved with only a 43 μm thick c-Si, fabricated by low-cost lift-off technique of epitaxial silicon [26]. To compare, conventional manufacturing process of c-Si solar cells requires $\sim 300\,\mu$m thick wafers to achieve required absorption and rigidity.

Lambertian limit

The radiant intensity (power per unit solid angle per unit area) of light reflected from an ideal diffusely reflecting surface, or equally light emitted by an ideal diffuse radiator, is given by the Lambertian cosine law:

$$I = I_0 \cos(\theta) \tag{1.6}$$

where θ is the angle between the observer's line and the normal direction. A property of such surface is a constant radiance (brightness) at any observation angle, as although the emitted power is reduced by cosine of angle, the apparent size of the source is increased by the same factor.

Yablonovitch [27] has shown that within the limits of statistical ray optics and in the weak absorption regime, the ideal Labmertian scattering at the front interface with a perfect mirror on the back side can provide an effective optical path length enhancement of $4n^2 \sin(\theta)$, where n is the refractive index. This result, is often referred to as Lambertian, or Yablonovitch, or $4n^2$ limit of light trapping. For a c-Si ($n \approx 3.5$) the enhancement can be as high as ×50.

Approaches to light trapping

The optimization of light trapping schemes in thin film solar cells has been intensively investigated in the recent years [15] and a number of approaches has been proposed, among others: random texturing [25, 26], nanophotonic structures [28], diffraction gratings [29], dielectric particles [30], and last but not least plasmonic nanostructures [31], reviewed in details in the next section. It remains clear that for thin films the problem should be treated in wave optics regime as the scattering features have sizes on the order of wavelength or smaller. Computational studies reveal that appropriate design of nanophotonic structures allows to exceed the classical $4n^2$ limit [32].

It has been demonstrated that for c-Si Labmertian limit can be achieved with both random texturing [33] and regular inverted pyramid texturing [34]. Such approach is however not suitable for thin film cells as it requires deep etching of the material, often exceeding the thickness of thin film absorbers.

Nonetheless, nearly perfect anti-reflection of c-Si wafer can be achieved by applying nanophotonic structures [28]. In the experiment, the incorporation of sub-wavelength Si nanocylinders combined with a conventional anti-reflection coating resulted in the reduction of average reflectance of c-Si wafer from 32.2 down to 1.3% termed "black silicon".

In the case of a-Si:H or μc-Si:H based devices the texturing is realized by the deposition on textured substrates, as any attempt of an etching process would result in the destruction of the p-i-n junction. The highest currents of 17.5 mA/cm^2 and 17.1 mA/cm^2 from 280 nm thick a-Si:H cells were recently achieved with nanodomes [35] and random texturing [36], respectively. The later work attempts also to quantify the comparison between periodic and random texturing. Though the theory proves periodic structure to be superior, the experimental comparison revels the same performance of both structures. On the industrial scale light trapping is realized by deposition on intentionally roughened material either the transparent conductive oxide (TCO) front contact, in the superstrate cell configurations [37], or the metallic back reflector in the substrate configurations [38]. Any of the above approaches is however limited by the electrical properties of the material, as the introduction of roughness during the film growth results in the creation of defects and as a consequence increased recombination in the bulk and surface of the silicon layers.

Therefore, the optimized solution should provide effective light trapping while keeping the film flat, in order to maximize both the photo-generated current and the operating voltage.

1.3 Plasmonics

Plasmonics exploits the physics of collective oscillations of free electrons in metals, induced by the interactions with electromagnetic radiation. Incident light can be either coupled to the metal-dielectric interface in a form of propagating waves Surface Plasmon Polariton (SPP) waves, or confined in the nano-scale metallic structures at Localized Surface Plasmon Resonance (LSPR), which give a possibility to control optical energy in the subwavelength scale allowing for breaking the diffraction limit of dielectric photonics.

1.3.1 Electrodynamics of metals

The high density of free carriers in metals results in small spacings of the electron energy levels compared to thermal excitation energy $k_B T$ at room temperature, and thus, even for nanostructures with sizes on the order of a few nanometers, the interaction of metals with the electromagnetic field can be described with a set of classical macroscopic Maxwell equations [39]:

$$\nabla \cdot \mathbf{D} = \rho \qquad \nabla \times \mathbf{E} = -\frac{\partial \mathbf{B}}{\partial t} \tag{1.7}$$

$$\nabla \cdot \mathbf{B} = 0 \qquad \nabla \times \mathbf{H} = \mathbf{J} + \frac{\partial \mathbf{D}}{\partial t} \tag{1.8}$$

describing the link between electric field $\mathbf{E}$, dielectric displacement $\mathbf{D}$, magnetic field $\mathbf{H}$ and magnetic induction $\mathbf{B}$ with the charge and current densities, ρ and $\mathbf{J}$ respectively. Since the considerations can be limited to nonmagnetic media, the response of material can be described with electric polarization $\mathbf{P}$, being the volume density of electric dipole moments inside the material caused by the alignment of microscopic dipoles with the electric field, via:

$$\mathbf{D} = \varepsilon_0 \mathbf{E} + \mathbf{P}, \tag{1.9}$$

where ε_0 is the electric permittivity of vacuum. In the linear and isotropic media, the aggregate response of charges to the electric field is described by the material dielectric constant ε or relative permittivity with:

$$\mathbf{D} = \varepsilon_0 \varepsilon \mathbf{E} \tag{1.10}$$

leading to the expression:

$$\mathbf{P} = \varepsilon_0 (\varepsilon - 1) \mathbf{E} \tag{1.11}$$

Therefore, the optical properties of materials are described with a dielectric function $\varepsilon(\omega)$ of angular frequency ω, which provides the basis for a variety of phenomena occurring due to the dependence of ε on frequency. In general, $\varepsilon(\omega) = \varepsilon_1(\omega) + i\varepsilon_2(\omega)$ is a complex function, where the real part (ε_1) describes the strength of the polarization induced by an external electric field and the imaginary part (ε_2) describes the losses encountered in polarizing the material. At optical frequencies, $\varepsilon(\omega)$ can be experimentally determined from reflectivity measurements at varying angles and polarizations (ellipsometry). The ε_1 and ε_2 are directly related to the complex refractive index $\tilde{n}(\omega) = n(\omega) + i\kappa(\omega)$ via:

$$\varepsilon_1 = n^2 - \kappa^2 \qquad \varepsilon_2 = 2n\kappa \tag{1.12}$$

$$n^2 = \frac{\varepsilon_1}{2} + \frac{1}{2}\sqrt{\varepsilon_1^2 + \varepsilon_2^2} \qquad \kappa = \frac{\varepsilon_2}{2n} \tag{1.13}$$

where κ is the extinction coefficient describing the exponential attenuation of the electromagnetic field in the medium (by $I(x) = I_0 e^{-\alpha x}$) through the following link with the absorption coefficient α:

$$\alpha(\omega) = \frac{2\kappa(\omega)\omega}{c} \tag{1.14}$$

Since the conduction electrons in metals have nearly a continuum of available states, the optical properties of metals can be explained by a classical Drude model of free-electron gas moving against crystal lattice of positive ions. In the model, the details of lattice potential are approximated by an effective mass of electrons m, while the electron-electron and electron-phonon interactions, as well as scattering on lattice defects or grain boundaries, are described by damping occurring with a characteristic frequency Γ with typical values on the order of $10^{14}\,\mathrm{s}^{-1}$ at room temperature.

For a harmonic time dependence of the driving field, motion of electrons

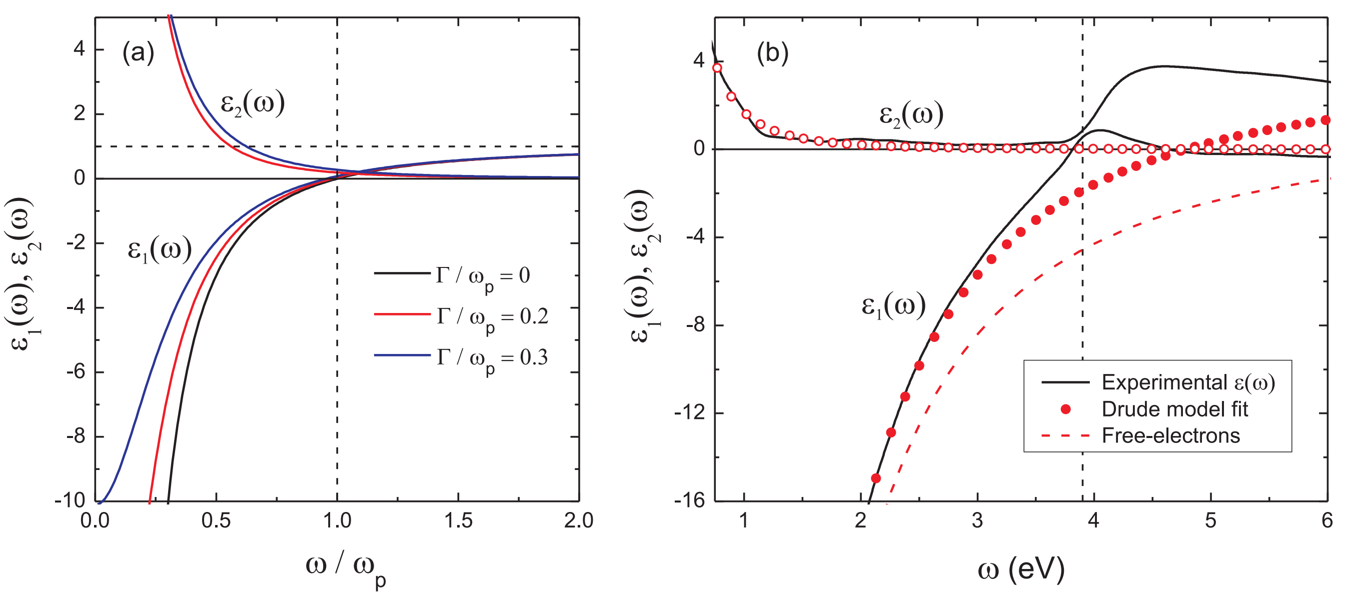

Figure 1.9: (a) Real ε_1 and imaginary ε_2 parts of the dielectric function of an electron gas with different values of damping Γ. (b) Drude model fit to the experimental data of Ag [40] according to the equations 1.20 with the following fitting parameters $\varepsilon_{int} = 3.7$, $\omega_p = 9.2\,\text{eV}$, $\Gamma = 0.02\,\text{eV}$. The dashed curve represents contribution of free-electrons to ε_1. The threshold frequency for interband transition at 3.9 eV being a limit for the validity of free-electron model is indicated.

can be written as:

$$m\frac{\mathrm{d}^2x}{\mathrm{d}t^2} + m\Gamma\frac{\mathrm{d}x}{\mathrm{d}t} = -e\ \mathbf{E_0}\mathrm{e}^{-i\omega t} \tag{1.15}$$

and the solution is given by:

$$\mathbf{x}(t) = \frac{e}{m(\omega^2 + i\Gamma\omega)}\mathbf{E}(t). \tag{1.16}$$

The displaced electrons contribute to the macroscopic polarization by the relation $\mathbf{P} = -ne\mathbf{x}$, with n being the electron concentration and e the elementary charge, explicitly given by:

$$\mathbf{P} = -\frac{ne^2}{m(\omega^2 + i\Gamma\omega)}\mathbf{E} \tag{1.17}$$

Consequently, comparison with equation 1.11 yields an expression for the dielectric function of the free electron gas:

$$\varepsilon(\omega) = 1 - \frac{\omega_p^2}{\omega^2 + i\Gamma\omega}, \tag{1.18}$$

where $\omega_p = ne^2/\varepsilon_0 m$ is the plasma frequency of the electron gas. The real and imaginary parts of the free-electron dielectric function with different values of damping were plotted in Fig. 1.9(a). Due to the strong dependence of ε on frequency, metals show considerably different optical properties across the electromagnetic spectrum. For frequencies up to the visible part of the spectrum metals are highly reflective and the propagation of electromagnetic waves through them is limited only to skin depth on the order of nanometers This is a direct consequence of the high negative values of their real part of the dielectric function below the plasma frequency. Notably, for high frequencies approaching ω_p the damping starts to be negligible resulting in ε_2 approaching zero. At ultraviolet frequencies (above ω_p), metals acquire dielectric character and allow the propagation of electromagnetic waves with attenuation dependent on their electronic structure.

In the case of noble metals (e.g. Cu, Ag, Au) atoms consists of completely filled 3d-, 4d-, and 5d-shells having just a single electron in the 4s-, 5s-, and 6s-bands. Although, the optical response is essentially determined by the s-shell, the filled d-band close to the Fermi surface causes a residual

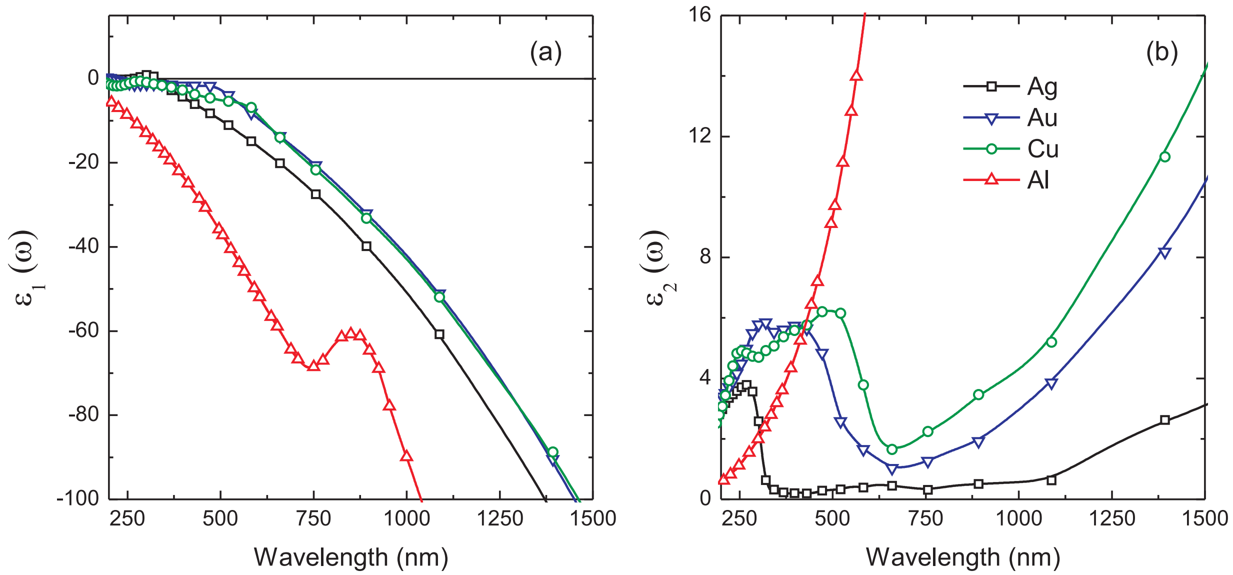

Figure 1.10: Experimental values of (a) real ε_1 and (b) imaginary ε_2 parts of the dielectric function of metals considered for plasmonic applications in visible spectral range. Data taken from Refs. [40] (Ag, Au, Cu) and [41] (Al).

polarization background due to ion cores. This effect can be described by adding a constant to the dielectric function, which leads to:

$$\varepsilon(\omega) = \varepsilon_{int} - \frac{\omega_p^2}{\omega^2 + i\Gamma\omega}, \tag{1.19}$$

giving explicitly:

$$\varepsilon_1(\omega) = \varepsilon_{int} - \frac{\omega_p^2}{\omega^2 + \Gamma^2} \qquad \varepsilon_2(\omega) = \frac{\omega_p^2\Gamma}{\omega(\omega^2 + \Gamma^2)}. \tag{1.20}$$

Drude model fit to the experimental data of Ag [40] according to the equations 1.20 with the following values of parameters $\varepsilon_{int} = 3.7$, $\omega_p = 9.2\,\mathrm{eV}$, $\Gamma = 0.02\,\mathrm{eV}$, is depicted in Fig. 1.9(b). In the NIR and visible spectral range, free electrons resembles well the optical properties of Ag. In general however, the optical response of metals is strongly influenced by the interband transitions of bound electrons leading to a considerable increase in ε_2. Thus, the threshold frequency of the transitions between electronic bands sets the limit for the validity of the free electron model. The dielectric functions of silver, gold, copper, and aluminum - the main candidates for plasmonic applications in the visible spectral range - are shown in Fig. 1.10. Clearly, the values of ε_2 increase significantly above the threshold for interband transitions, which for the case of silver and gold, the two material of the highest importance for plasmonics, are 3.9 eV and 2.3 eV resulting in much higher losses observed for gold in the visible range.

1.3.2 Localized Surface Plasmon Resonance

Localized surface plasmons are non-propagating excitations of the conduction electrons of metallic nanoparticles in an oscillating electromagnetic field, schematically shown in Fig. 1.11. The interactions with fixed background of positively charged ion cores gives a restoring force on the driven electrons so that a resonance can arise, leading to field amplification both inside and in the near-field zone outside the particle. The plasmon resonances can be excited by direct illumination, in contrast to the propagating SPPs requiring the phase-matching condition. For noble metals, silver and gold, the resonance is observed in the visible region of the electromagnetic spectrum.

In the first-order approach, the interaction of a particle of size d with

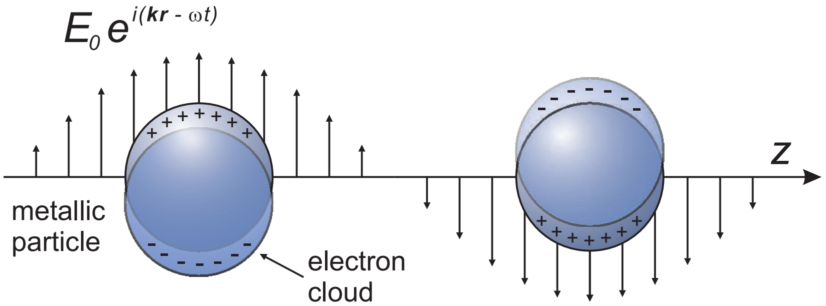

Figure 1.11: Sketch of a Localized Surface Plasmon Resonance (LSPR) mechanism - excitation of an electron cloud of a metallic nanosphere placed in an oscillating electromagnetic field.

the electromagnetic field can be analyzed by assumption that the particle is much smaller than the illumination wavelength ($d \ll \lambda$) in the surrounding medium, which implies that the phase of harmonic electromagnetic field is nearly constant over the particle volume. As such, the scattering problem can be simplified to a particle in an electrostatic field, known as quasi-static approximation [42].

Let's consider a homogeneous, isotropic sphere of radius a located at the origin in a uniform, static electric field as depicted in Fig. 1.12. The surrounding medium is taken to be isotropic and non-absorbing with dielectric constant ε_m and the sphere is described by a complex dielectric function $\varepsilon(\omega)$. The electric field is parallel to the z-direction at sufficient distance from the sphere. In the electrostatic approximation,

$$\mathbf{E}(\mathbf{r}, t) = E_0 e^{i(\mathbf{k}\cdot\mathbf{r} - \omega t)} \quad \longrightarrow \quad \mathbf{E} = E_0 \hat{z}, \tag{1.21}$$

light scattering problem is addressed by solving Laplace equation for potential Φ (from which one can calculate the electric field):

$$\nabla^2 \Phi = 0 \qquad \mathbf{E} = -\nabla \Phi. \tag{1.22}$$

Due to the azimuthal symmetry of the problem, the general solution is

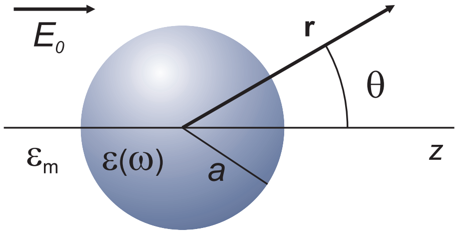

Figure 1.12: Sketch of a spherical particle with radius a and complex dielectric function $\varepsilon(\omega)$ placed in homogeneous medium ε_m. Geometry used for quasi-static approximation calculations.

of the form:

$$\Phi(r,\theta) = \sum_{l=0}^{\infty} \left[A_l r^l + B_l r^{-l(l+1)} \right] P_l(\cos\theta), \tag{1.23}$$

where $P_l(\cos\theta)$ are the Legendre Polynomials of order l, and θ is the angle between the position vector $\mathbf{r}$ at the z-axis.

The coefficients A_l and B_l are determined from the boundary conditions: (i) at $r \to \infty$ and (ii) from equality of potentials, tangential components of the electric field, and normal components of the displacement field at $r = a$. Without presenting the detail calculations, the potentials inside (Φ_{in}) and outside (Φ_{out}) the sphere can be written as:

$$\Phi_{in} = -\frac{3\varepsilon_m}{\varepsilon + 2\varepsilon_m} E_0 r \cos\theta \tag{1.24}$$

$$\Phi_{out} = -E_0 r \cos\theta + \frac{\varepsilon - \varepsilon_m}{\varepsilon + 2\varepsilon_m} E_0 a^3 \frac{\cos\theta}{r^2}. \tag{1.25}$$

Physically, the applied field induces a dipole moment

$$\mathbf{p} = 4\pi\varepsilon_0\varepsilon_m a^3 \frac{\varepsilon - \varepsilon_m}{\varepsilon + 2\varepsilon_m} \mathbf{E_0} \tag{1.26}$$

at the center of the particle, and thus Φ_{out} can be interpreted as a superposition of the applied field and that of a dipole:

$$\Phi_{out} = -E_0 r \cos\theta + \frac{\mathbf{p} \cdot \mathbf{r}}{4\pi\varepsilon_0\varepsilon_m r^3} \tag{1.27}$$

This leads to an expression for (complex) polarizability α, defined via $\mathbf{p} = \varepsilon_0 \varepsilon_m \alpha \mathbf{E_0}$, of a small sphere with sub-wavelength diameter in the electrostatic approximation:

$$\alpha = 4\pi a^3 \frac{\varepsilon - \varepsilon_m}{\varepsilon + 2\varepsilon_m} \tag{1.28}$$

It is apparent that the polarizability is enhanced when the condition $|\varepsilon + 2\varepsilon_m|$ is minimized, which in particular is satisfied by negative values of ε. According to the free-electron model the real part of the dieletric function for metals is negative for frequencies lower than the plasma frequency (ω_p) which enables (in an oscillating field) a strong resonance of α known as a dipole mode of localized surface plasmon resonance (LSPR). The magnitude of α at the resonance is however limited by the incomplete vanishing of its denominator $\mathrm{Im}[\varepsilon] \neq 0$. In the case of small or slowly-varying $\mathrm{Im}[\varepsilon]$ the resonance condition simplifies to, so called Fröhlich relation:

$$\mathrm{Re}[\varepsilon(\omega)] = -2\varepsilon_m, \tag{1.29}$$

Due to the decrease of $\mathrm{Re}[\varepsilon(\omega)]$ with decreasing frequency, equation 1.29 shows also that in general the spectral position of the plasmon resonance red-shifts with increased ε_m, or equivalently refractive index n of the surrounding medium.

The distribution of the electric field inside $\mathbf{E_{in}}$ and outside $\mathbf{E_{out}}$, evaluated from respective potentials, is given by:

$$\mathbf{E_{in}} = \frac{3\varepsilon_m}{\varepsilon + 2\varepsilon_m} \mathbf{E_0} \tag{1.30}$$

$$\mathbf{E_{out}} = \mathbf{E_0} + \frac{3\mathbf{n}(\mathbf{n} \cdot \mathbf{p}) - \mathbf{p}}{4\pi\varepsilon_0\varepsilon_m} \, \frac{1}{r^3} \tag{1.31}$$

As expected, the resonance of α implies also a resonant enhancement of both the internal and external fields. This near-field enhancement sets the basis on which many of the applications of metal nanoparticles in optical devices and sensors rely on.

The above considerations show that in quasistatic-approximation a small sphere ($a \ll \lambda$) can be represented as an ideal dipole. This allows to extend the model for the time-varying electric fields but still neglecting spatial retardation effects over the particle volume. Thus, under plane-wave illumination $\mathbf{E}(\mathbf{r}, t) = \mathbf{E_0} e^{-i\omega t}$ the fields induce an oscillating dipole moment $\mathbf{p}(t) = \varepsilon_0 \varepsilon_m \alpha \mathbf{E_0} e^{-i\omega t}$ with α given by electrostatics equation 1.28. The radiation of this dipole leads to scattering of the plane wave by the sphere and the corresponding cross sections for scattering and absorption C_{Scatt} and C_{Abs}, determined via the Poynting-vector of such an oscillating electric dipole, are given by:

$$C_{Scatt} = \frac{k^4}{6\pi} |\alpha|^2 = \frac{8\pi}{3} k^4 a^6 \left| \frac{\varepsilon - \varepsilon_m}{\varepsilon + 2\varepsilon_m} \right| \tag{1.32}$$

$$C_{Abs} = k \ \mathrm{Im}[\alpha] = 4\pi k a^3 \ \mathrm{Im} \left[\frac{\varepsilon - \varepsilon_m}{\varepsilon + 2\varepsilon_m} \right] \tag{1.33}$$

As can be seen, the resonantly enhanced polarizability results in resonant enhancement of the efficiency with which a metal nanoparticle scatters and absorbs light. However it is important to note that the cross-sections for absorption scales with particle volume ($\propto a^3$) while the cross-sections for scattering scales with squared volume ($\propto a^6$). Therefore, the optical response of small particles is dominated by absorption, while due to the rapid increase of C_{Scatt} with NP size, the response of big particles is driven by scattering.

Though the theory of dipole particles outlined above is strictly valid only for vanishingly small particles, it assures a reasonably good agreement for spheres with dimensions below 100 nm illuminated with visible or near-infrared radiation and is adequate for the purpose of this chapter. The rigorous solution of Maxwell equations for the case of spherical particle with arbitrary size can be done with an approach known as Mie theory [43], consisting in representation of the internal and scattered fields as a set of normal modes described by vector harmonics. The scattering, absorption and extinction cross sections for silver nanoparticles, calculated with the Mie theory, are presented and discussed in chapter 2, section 2.3. On the whole, calculation of the optical response of a non-ellipsoidal particle placed in a non-homogeneous medium, i.e. at the interface between two materials, requires mesh-type numerical approaches, like finite difference or finite element methods in time or frequency domain.

1.3.3 Plasmonic light trapping

Light-trapping geometries

The unique properties of plasmonic resonances discussed in the previous section can be exploited for the light trapping in thin film solar cells, which in the last years emerged as a broad research field [31]. The pioneering work on the enhancement of light coupling into thin film silicon due to the resonant scattering from subwavelength metallic nanoparticles was done in 1998 by Stuart and Hall [44], who showed up to 18 fold photocurrent enhancement of a Si-on-insulator photodetector structure with dense silver nanoparticle arrays placed on the top surface of the device. The applications of plasmonic scattering for PV appeared only after 2005 with several demonstrations of photocurrent enhancements in silicon solar cells [45–47] supported by theoretical works [48, 49].

Improvement of absorption in reduced volumes of semiconductor material with plasmonic excitations can be achieved by taking advantage of:

1. Near-field enhancement, schematically shown in Fig. 1.13(a). Nanoparticles can act as an antenna for the incident light concentrating the energy in the local electric field of the surface plasmon mode, which is most pronounced for small particles ($5 - 20\,\mathrm{nm}$). However, for the energy conversion to be efficient, the absorption rate of the semiconductor must exceed the reciprocal of plasmon decay time (typical lifetimes $10 - 50\,\mathrm{fs}$). This approach is particularly suitable for materials where small carrier diffusion lengths require ultra-thin absorbers for the effective collection of photocarriers, i.e. organic semiconductors, for which an increase in efficiency by a factor of 1.7 has been demonstrated [50].

2. Surface Plasmon Polaritons (SPP), schematically shown in Fig. 1.13(b). Incident light can be coupled, e.g. using metallic gratings in rear mirror, into electromagnetic waves traveling along the interface between the metal back contact and the absorber layer. Notably, in this configuration the incident light is effectively turned by 90° and absorbed along the lateral direction of the solar cell. The penetration depth of evanescent fields into the semiconductor is much larger than into the metal allowing for the major part of energy to be absorbed in the semiconductor if only its absorption coefficient is sufficiently higher

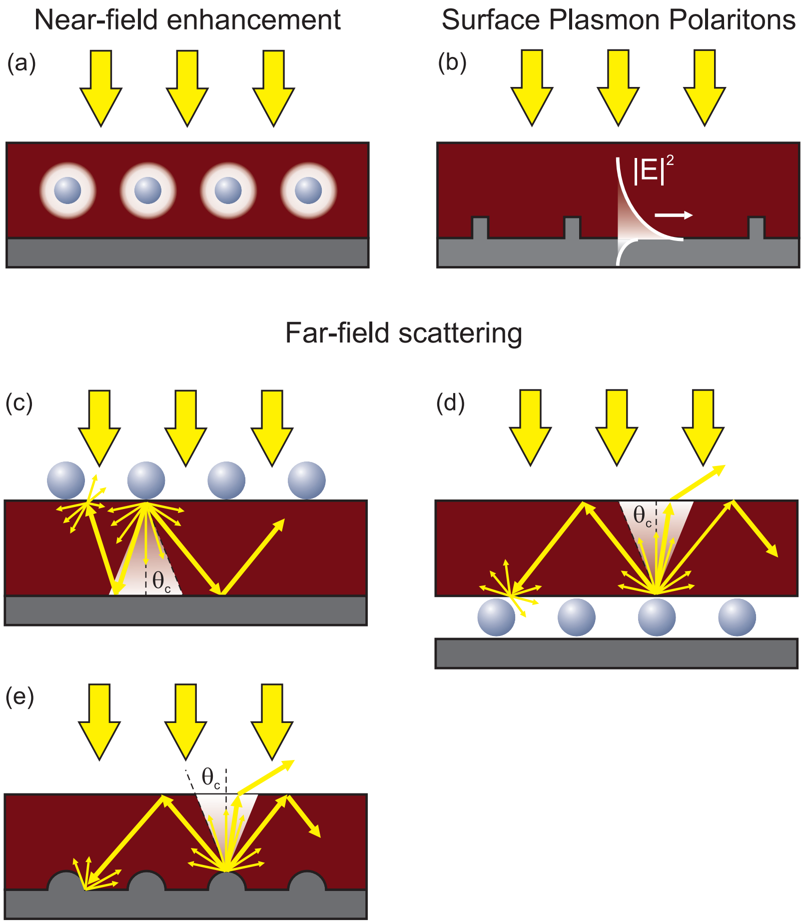

Figure 1.13: Schematic illustration of plasmon-induced light trapping in thin film solar cells due to: (a) near-field enhancement, (b) surface plasmon polaritons (SPP), and (c-e) far-field scattering from metallic nanoparticles placed either on the front (c) or on the rear (d) side of the cell, and from corrugated back reflector (e).

than the one of metal. However, in visible and NIR spectral range SPPs suffer from relatively high ohmic losses reducing the propagation lengths and consequently limiting the applicability in solar cells.

3. Far-field scattering, schematically shown in Figs. 1.13(c-e). Subwavelength metallic nanoparticles can scatter light efficiently over a broad wavelength range of the solar spectrum due to the localized surface plasmon resonances. In addition, when NPs are placed close to the interface between two dielectrics, the scattering occurs preferentially into the material with higher refractive index, i.e. silicon. Such scattered light is redirected away from the specular direction effectively increasing the optical path length at the wavelengths that are normally poorly absorbed in the photovoltaic material. Furthermore, light scattered at angles beyond the critical angle for the total internal reflection ($\theta_c \simeq 16°$ for the Si/air interface) can be coupled into the guided mode and remain trapped in the cell. Nonetheless, all beneficial effects outlined above come with the cost of parasitic absorption occurring in the NPs. The optical properties of the NPs are strongly dependent on their geometry (size and shape) and on the refractive index of the surrounding mediums. Therefore, the challenge is to design NPs properly for (i) maximized scattering and minimized absorption, (ii) broad spectral response, (iii) broad angular distribution of scattered light, (iv) absorption outside the useful wavelength range, (v) weak dependence on polarization and angle of incidence. Moreover, to be directly applicable in the photovoltaic industry, the NPs fabrication method needs to be reliable, low-cost and scalable up to square meter sizes.

The latter light trapping scheme has been widely investigated in the recent years and recognized as the most promising for PV applications, having also a considerable number of experimentally proven photocurrent and efficiency enhancements of thin film solar cells. Thus, a certain optimization guidelines, concerning NPs' geometry device configuration, can be extracted from the literature.

Size. The theoretical studies show that the scattering efficiency (ratio between scattering and extinction of light) increases with increasing NP size and saturates at values close to unity. In addition, the spectral position of LSP resonance shifts towards longer wavelengths and broadens significantly [51]. Thus, for solar cells applications big NPs, with sizes of $100 - 200\,\text{nm}$, are generally preferable. Bigger sizes may result in a shift of resonance outside the wavelength range of interest and decrease the coupling.

Shape. The cross-section shape of NP determines the spectral response and more importantly the coupling efficiency to the underlying high refractive index layer. Computational studies reveal that the most desirable are geometries with high contact area to the substrate (cylinder or hemisphere), which allow for $85 - 90\%$ of incident light being scattered into the substrate [49].

The highest combination of scattering and coupling efficiencies was found for cylindrical NPs placed directly on the rear side of Si substrate with diameters bigger than 100 nm and heights lower than 50 nm. In this case, the angular distribution of scattered light at resonance is similar to the ideal Lambertian case [52].

Environment. High refractive index of embedding medium is useful for the red shift of LSP resonance. In addition, when the NP are placed close to the interface between two dielectric materials, a strong preferential scattering towards high refractive index material occurs. Therefore, for rear located NPs, the coupling efficiency increases significantly with decreasing spacing layer between Si and the NPs, which has been demonstrated experimentally [53] and theoretically [52] and can be explained by an overlap between NP near field and the substrate. In case of front located NPs, the spacer layer can be beneficial as it reduces the destructive interference between incident and reflected field which influences the driving field of NPs [53].

Device configuration. The high optical losses in the NPs at short wavelengths, leading to the decrease of EQE when incorporated on the front side of device, can be suppressed by placing them on the rear side of the solar cell, so that they interact only with the long-wavelength photons which are not absorbed during the first pass through the cell absorber material [53, 54].

The a-Si:H technology gives an opportunity to incorporate plasmonic nanostructures at the rear side by using them as a substrate for the deposition of p-i-n layers. Such configuration has been widely investigated resulting in experimental demonstration of high photo-generated currents, for instance, $16.9\,\mathrm{mA/cm^2}$ and $21\,\mathrm{mA/cm^2}$ have been achieved as the result of light trapping provided by nanopatterned back reflector in ultra-thin a-Si:H [55] and μc-Si:H solar cells [56], respectively. The nano-patterning is done, however, with complicated and expensive techniques, like electron beam lithography or nanoimprint lithography. An alternative approach takes advantage of self assembled NPs fabricated in the, so called, plasmonic back reflector (PBR) configuration consisting of the stack: glass substrate, flat mirror, spacer layer, NPs and cover layer. It has been demonstrated that PBR can provide efficient light trapping, comparable to state-of-art random-texturing [57], resulting in photocurrents of 15.6 mA/cm^2 [58] achieved with a-Si:H solar cell [58] and 25.5 mA/cm^2 with μc-Si:H [59].

References

[1] British petroleum, "BP Statistical Review of World Energy." [Online]. Available: www.bp.com

[2] N. Armaroli and V. Balzani, "Solar energy basis," in *Energy for a Sustainable World: From the Oil Age to Sun-Powered Future.* Wiley-VCH Verlag GmbH & Co. KGaA, 2011, pp. 157–165.

[3] V. S. Arunachalam and A. Bharadwaj, "The global energy landscape and energy security," in *Fundamentals of Materials for Energy and Environmental Sustainability*, D. S. Ginley and D. Cahen, Eds. Cambrige University Press, 2012, pp. 26–35.

[4] X. C. K. Russell R. Chianelli and S. A. Holditch, "Petroleum and natural gas," in *Fundamentals of Materials for Energy and Environmental Sustainability*, D. S. Ginley and D. Cahen, Eds. Cambrige University Press, 2012, pp. 106–116.

[5] IEA International Energy Agency, "Key World Energy Statistics 2014." [Online]. Available: www.iea.org

[6] F. M. Orr and S. M. Benson, "Sustainability and energy conversion," in *Fundamentals of Materials for Energy and Environmental Sustainability*, D. S. Ginley and D. Cahen, Eds. Cambrige University Press, 2012, pp. 36–47.

[7] EPIA European Photovoltaic Industry Association, "Global Market Outlook For Photovoltaics 2014-2018." [Online]. Available: www.epia.org

[8] European Commission Joint Research Centre, "JRC Scientific and Policy Reports. PV Status Report 2012," 2012. [Online]. Available: iet.jrc.ec.europa.eu/remea/sites/remea/files/pv_status_report_2013.pdf

[9] M. A. Green, "Photovoltaics for the 21st century II," *Eletrochem. Soc. Proc.*, vol. 10, pp. 30–45, 2001.

[10] M. A. Green, K. Emery, Y. Hishikawa, W. Warta, and E. D. Dunlop, "Solar cell efficiency tables (version 44)," *Progress in Photovoltaics: Research and Applications*, vol. 22, no. 7, pp. 701–710, 2014.

[11] Panasonic Press Release, "Panasonic HIT solar cell achieves worlds highest energy conversion efficiency of 25.6% at research level," 2014. [Online]. Available: http://news.panasonic.com/press/news/official.data/data.dir/2014/04/en140410-4/en140410-4.html

[12] J. Zhao, A. Wang, M. A. Green, and F. Ferrazza, "19.8% efficient honeycomb textured multicrystalline and 24.4% monocrystalline silicon solar cells," *Applied Physics Letters*, vol. 73, no. 14, pp. 1991–1993, 1998.

[13] B. Kayes, "27.6% conversion efficiency, a new record for single-junction solar cells under 1 sun illumination," *Proceedings of the 37th IEEE Photovoltaic Specialists Conference, 2011*, 2011.

[14] J.-F. Guillemoles, "Future concepts for photovoltaic energy conversion," in *Fundamentals of Materials for Energy and Environmental Sustainability*, D. S. Ginley and D. Cahen, Eds. Cambrige University Press, 2012, pp. 26–35.

[15] F. Priolo, T. Gregorkiewicz, M. Galli, and T. F. Krauss, "Silicon nanostructures for photonics and photovoltaics," *Nature Nanotechnology*, vol. 9, pp. 19–32, 2014.

[16] M. A. Green, "Self-consistent optical parameters of intrinsic silicon at 300k including temperature coefficients," *Solar Energy Materials and Solar Cells*, vol. 92, no. 11, pp. 1305 – 1310, 2008.

[17] PV Education. [Online]. Available: pveducation.org

[18] D. Aspnes and A. Studna, "Dielectric functions and optical parameters of Si, Ge, GaP, GaAs, GaSb, InP, InAs, and InSb from 1.5 to 6.0 ev," *Physical Review B*, vol. 27, no. 2, p. 9851009, 1983.

[19] M. Alonso, M. Garriga, C. Durante Rincn, E. Hernndez, and M. Len, "Optical functions of chalcopyrite CuGaxIn1-xSe2 alloys," *Applied Physics A*, vol. 74, no. 5, pp. 659–664, 2002.

[20] W. Shockley and H. J. Queisser, "Detailed balance limit of efficiency of p-n junction solar cells," *Journal of Applied Physics*, vol. 32, no. 3, pp. 510–519, 1961.

[21] O. D. Miller, E. Yablonovitch, and S. R. Kurtz, "Strong internal and external luminescence as solar cells approach the Shockley-Queisser limit," *Photovoltaics, IEEE Journal of*, vol. 2, no. 3, pp. 303–311, 2012.

[22] A. Polman and H. A. Atwater, "Photonic design principles for ultrahigh-efficiency photovoltaics," *Nature Materials*, vol. 11, p. 174177, 2012.

[23] J. L. Gray, "The physics of the solar cell," in *Handbook of Photovoltaic Science and Engineering*, A. Luque and S. Hegedus, Eds. John Wiley & Sons Ltd, 2003, pp. 61–112.

[24] P. N. Saeta, V. E. Ferry, D. Pacifici, J. N. Munday, and H. A. Atwater, "How much can guided modes enhance absorption in thin solar cells?" *Opt. Express*, vol. 17, no. 23, pp. 20 975–20 990, 2009.

[25] P. Kowalczewski, A. Bozzola, M. Liscidini, and L. Claudio Andreani, "Light trapping and electrical transport in thin-film solar cells with randomly rough textures," *Journal of Applied Physics*, vol. 115, no. 19, 2014.

[26] J. H. Petermann, D. Zielke, J. Schmidt, F. Haase, E. G. Rojas, and R. Brendel, "19%-efficient and 43m-thick crystalline si solar cell from layer transfer using porous silicon," *Progress in Photovoltaics: Research and Applications*, vol. 20, no. 1, pp. 1–5, 2012.

[27] E. Yablonovitch, "Statistical ray optics," *Journal of the Optical Society of America*, vol. 72, no. 7, pp. 899–907, 1982.

[28] P. Spinelli, M. Verschuuren, and A. Polman, "Broadband omnidirectional antireflection coating based on subwavelength surface mie resonators," *Nature Communications*, vol. 3, no. 692, 2012.

[29] E. R. Martins, J. Li, Y. Liu, V. Depauw, Z. Chen, J. Zhou, and T. F. Krauss, "Deterministic quasi-random nanostructures for photon control," *Nature Communications*, vol. 4, no. 2665, 2013.

[30] J. Grandidier, D. M. Callahan, J. N. Munday, and H. A. Atwater, "Light absorption enhancement in thin-film solar cells using whispering gallery modes in dielectric nanospheres," *Advanced Materials*, vol. 23, no. 10, pp. 1272–1276, 2011.

[31] H. A. Atwater and A. Polman, "Plasmonics for improved photovoltaic devices," *Nature Materials*, vol. 9, pp. 205–213, 2010.

[32] D. M. Callahan, J. N. Munday, and H. A. Atwater, "Solar cell light trapping beyond the ray optic limit," *Nano Letters*, vol. 12, no. 1, pp. 214–218, 2012.

[33] P. Kowalczewski, M. Liscidini, and L. C. Andreani, "Engineering gaussian disorder at rough interfaces for light trapping in thin-film solar cells," *Optics Letters*, vol. 37, no. 23, pp. 4868–4870, 2012.

[34] A. Mavrokefalos, S. E. Han, S. Yerci, M. S. Branham, and G. Chen, "Efficient light trapping in inverted nanopyramid thin crystalline silicon membranes for solar cell applications," *Nano Letters*, vol. 12, no. 6, pp. 2792–2796, 2012.

[35] J. Zhu, C.-M. Hsu, Z. Yu, S. Fan, and Y. Cui, "Nanodome solar cells with efficient light management and self-cleaning," *Nano Letters*, vol. 10, no. 6, pp. 1979–1984, 2010.

[36] C. Battaglia, C.-M. Hsu, K. Sderstrm, J. Escarr, F.-J. Haug, M. Charrire, M. Boccard, M. Despeisse, D. T. L. Alexander, M. Cantoni, Y. Cui, and C. Ballif, "Light trapping in solar cells: Can periodic beat random?" *ACS Nano*, vol. 6, no. 3, pp. 2790–2797, 2012.

[37] J. Müller, B. Rech, J. Springer, and M. Vanecek, "TCO and light trapping in silicon thin film solar cells," *Solar Energy*, vol. 77, no. 6, pp. 917–930, 2004.

[38] K. Sderstrm, F.-J. Haug, J. Escarr, C. Pahud, R. Biron, and C. Ballif, "Highly reflective nanotextured sputtered silver back reflector for flexible high-efficiency nip thin-film silicon solar cells," *Solar Energy Materials and Solar Cells*, vol. 95, no. 12, pp. 3585 – 3591, 2011.

[39] S. A. Maier, "Electromagnetics of metals," in *Plasmonics: Fundamentals and Applications.* Springer US, 2007, pp. 5–19.

[40] P. B. Johnson and R. W. Christy, "Optical constants of the noble metals," *Physical Review B*, vol. 6, pp. 4370–4379, 1972.

[41] E. D. Palik, Ed., *Handbook of Optical Constants of Solids Vol I.* Academic Press, 1985.

[42] S. A. Maier, "Localized surface plasmons," in *Plasmonics: Fundamentals and Applications.* Springer US, 2007, pp. 65–88.

[43] C. F. Bohren and D. R. Huffman, *Absorption and Scattering of Light by Small Particles.* Wiley-VCH Verlag GmbH, 2007.

[44] H. R. Stuart and D. G. Hall, "Island size effects in nanoparticle-enhanced photodetectors," *Applied Physics Letters*, vol. 73, no. 26, 1998.

[45] D. M. Schaadt, B. Feng, and E. T. Yu, "Enhanced semiconductor optical absorption via surface plasmon excitation in metal nanoparticles," *Applied Physics Letters*, vol. 86, no. 6, 2005.

[46] D. Derkacs, S. H. Lim, P. Matheu, W. Mar, and E. T. Yu, "Improved performance of amorphous silicon solar cells via scattering from surface plasmon polaritons in nearby metallic nanoparticles," *Applied Physics Letters*, vol. 89, no. 9, 2006.

[47] S. Pillai, K. R. Catchpole, T. Trupke, and M. A. Green, "Surface plasmon enhanced silicon solar cells," *Journal of Applied Physics*, vol. 101, no. 9, 2007.

[48] K. R. Catchpole and A. Polman, "Plasmonic solar cells," *Opt. Express*, vol. 16, no. 26, pp. 21 793–21 800, 2008.

[49] ——, "Design principles for particle plasmon enhanced solar cells," *Applied Physics Letters*, vol. 93, no. 19, 2008.

[50] A. J. Morfa, K. L. Rowlen, T. H. Reilly, M. J. Romero, and J. van de Lagemaat, "Plasmon-enhanced solar energy conversion in organic bulk heterojunction photovoltaics," *Applied Physics Letters*, vol. 92, no. 1, 2008.

[51] T. L. Temple and D. M. Bagnall, "Broadband scattering of the solar spectrum by spherical metal nanoparticles," *Progress in Photovoltaics: Research and Applications*, vol. 21, no. 4, pp. 600–611, 2013.

[52] F. J. Beck, S. Mokkapati, and K. R. Catchpole, "Light trapping with plasmonic particles: beyond the dipole model," *Opt. Express*, vol. 19, no. 25, pp. 25 230–25 241, 2011.

[53] S. Pillai, F. J. Beck, K. R. Catchpole, Z. Ouyang, and M. A. Green, "The effect of dielectric spacer thickness on surface plasmon enhanced solar cells for front and rear side depositions," *Journal of Applied Physics*, vol. 109, no. 7, 2011.

[54] Z. Ouyang, X. Zhao, S. Varlamov, Y. Tao, J. Wong, and S. Pillai, "Nanoparticle-enhanced light trapping in thin-film silicon solar cells," *Progress in Photovoltaics: Research and Applications*, vol. 19, no. 8, pp. 917–926, 2011.

[55] V. E. Ferry, M. A. Verschuuren, M. C. v. Lare, R. E. I. Schropp, H. A. Atwater, and A. Polman, "Optimized spatial correlations for broadband light trapping nanopatterns in high efficiency ultrathin film a-Si:H solar cells," *Nano Letters*, vol. 11, no. 10, pp. 4239–4245, 2011.

[56] U. W. Paetzold, E. Moulin, D. Michaelis, W. Bttler, C. Wchter, V. Hagemann, M. Meier, R. Carius, and U. Rau, "Plasmonic reflection grating back contacts for microcrystalline silicon solar cells," *Applied Physics Letters*, vol. 99, no. 18, 2011.

[57] H. Tan, R. Santbergen, A. H. M. Smets, and M. Zeman, "Plasmonic light trapping in thin-film silicon solar cells with improved self-assembled silver nanoparticles," *Nano Letters*, vol. 12, no. 8, pp. 4070–4076, 2012.

[58] H. Tan, R. Santbergen, G. Yang, A. Smets, and M. Zeman, "Combined optical and electrical design of plasmonic back reflector for high-

efficiency thin-film silicon solar cells," *Photovoltaics, IEEE Journal of*, vol. 3, no. 1, pp. 53–58, 2013.

[59] H. Tan, L. Sivec, B. Yan, R. Santbergen, M. Zeman, and A. H. M. Smets, "Improved light trapping in microcrystalline silicon solar cells by plasmonic back reflector with broad angular scattering and low parasitic absorption," *Applied Physics Letters*, vol. 102, no. 15, 2013.

Chapter 2

Correlation between structural and optical properties of self-assembled silver nanoparticles

In this chapter, a detailed, systematic study of the correlation between the structural and the optical characteristics of self-assembled silver nanostructures is reported. First, a phenomenology of a solid-state dewetting (SSD) process, which consist in thermally-induced morphology transformation from a thin film to an array of islands or nanoparticles (NPs), is presented. This is followed by a study of the optical characteristics, computed with the analytical Mie formalism, for single, spherical Ag NPs of different diameters and different surrounding media. This provides a theoretical background of the localized plasmonic resonance and serves as a first-order approximation for interpretation of the experimental results.

It is then shown that four distinct types of morphologies tend to form in specific ranges of fabrication parameters. These can quantitatively be summarized by a proposed structural-phase diagram and allows to identify the conditions for preferable, uniformly spaced circular NPs. The optical properties of the NPs stay in qualitative agreement with the trends predicted by Mie theory, and correlate with the surface coverage (SC) distributions and the mean SC size. The applicability of such Ag NPs in solar cells, in terms of scattering efficiencies, is then discussed. In the last paragraph, properties of NPs embedded in aluminium doped zinc oxide (AZO) are analysed as a step forward towards the implementation in thin film photovoltaics.

2.1 Solid-state dewetting

Solid-state dewetting (SSD) is a process of morphology transformation from a thin film to an array of islands or droplets due to a thermal treatment, in which the film remains in the solid-state. The driving force of the phenomena is the minimization of the free surface energy of the film, the substrate and the film-substrate interface [1].

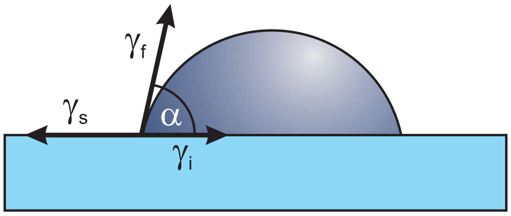

Figure 2.1: The equilibrium shape (a spherical cap with contact angle θ) of an island with an isotropic surface energy supported on a rigid substrate. γ_f, γ_s and γ_i are the surface energies of the island, the substrate and the island-substrate interface, respectively.

The energy minimization condition for an island with an isotropic surface energy per unit area, γ_f, supported on a rigid substrate with surface energy per unit area γ_s, gives an equilibrium shape of a spherical cap with contact angle θ, schematically shown in Fig. 2.1, defined by the Young-Laplace equation:

$$\gamma_s = \gamma_i + \gamma_f \cos\theta \tag{2.1}$$

where γ_i is the surface energy of the island-substrate interface. In general, if the condition:

$$\gamma_s - \gamma_i - \gamma_f > 0 \tag{2.2}$$

is satisfied the film is stable and will not dewet; otherwise, the film is metastable and will dewet when the rates of necessary kinetic process are sufficiently high.

Thin films are generally metastable in the as-deposited state as they usually form in conditions of atomic motion limited to, depending on the deposition technique, values as low as a nanometer. Therefore, most films would spontaneously dewet to form islands when heated to temperatures at which atom mobilities are sufficiently high to provide effective mass transport. This can occur at temperatures well below the melting point of the material. The SSD process evolves through several steps: first, the process either initiates on holes preexisting in the film or, more likely, proceeds through the formation of new holes, which requires a certain incubation time; second, once stable holes are present, their edges start to retract leaving uncovered areas of the substrate, which eventually impinge to form elongated strands of material; third, the process continues through a Rayleigh-Plateau-like instabilities in which strands decompose into single islands; and fourth, the shape of islands evolves towards the one defined by thermodynamic equilibrium. At this point, the structure reaches the final, stable surface coverage. Each of these steps has different dependencies on time and dimensions, although all are limited by the rate of surface self-diffusion, which on the other hand, increases exponentially with increasing temperature [1].

The threshold temperature at which dewetting is observed, T_D, decreases with decreasing film thickness, t_f. Owing to the high surface-to-volume ratio of thin films, the driving force for dewetting is higher in thinner films and as such the hole formation is more probable and the holes tend to be more closely spaced. T_D is also significantly lower for materials with low melting temperatures and tends to be higher for covalently bonded materials than for metals [1].

In polycrystalline films, the holes are preferentially formed by the grain boundary grooving process, in particular, the boundary triple junctions provide locations at which holes are more likely to form first [2]. The number of grooves per area increases with decreasing film thickness, and thus, the number of holes, that form during dewetting, scales inversely with t_f. In addition, the grain size of a polycrystalline film can strongly affect SSD. In general, the formation of holes requires an energetic cost associated with an increase in the surface area and hence grooving-induced dewetting occurs only when the grain size exceeds a certain critical value. The normal grain growth, however, stagnates when the grain size reaches approximately twice the film thickness and, in most cases, such films are expected to be stable with respect to grain boundary groove formation. Nonetheless, in high-purity metallic films normal or abnormal grain growth can occur at temperatures as low as $0.2T_m$ (T_m - melting temperature in Kelvins) which can trigger dewetting [1].

As-deposited metallic films are usually in the state of compressive stress on the order of 100 MPa for thermal evaporation and of 1 GPa for sputtering, depending on the materials and deposition conditions [3]. Such residual thermal stress, however, does not significantly contribute to the driving force for hole formation and growth. Nevertheless, compressive stress can lead to local delamination of the film from the substrate, which can promote dewetting. In addition, when the film is heated below T_D, a relaxation of compressive stress can occur and result in the formation of hillocks. During cooling down, a tensile stress can develop leading to grain thinning and possible hole formation, often near hillocks. Therefore, the thermal history of a film may affect whether there are holes present in the film, when it is subsequently heated to sufficiently high temperatures to allow dewetting [1].

The thermodynamics and kinetics of SSD process has been widely studied over the past few decades, firstly as a degradation mechanism of integrated circuits and microsystems [2] and recently as a large-area manufacturing method of NPs arrays [4] with many potential applications including, e.g. optical sensors [5], catalyst growth of carbon nanotubes [6] and semiconductor nanowires [7], and formation of networked structures for electrodes in fuel cells [8]. Fabrication of metallic NPs by SSD also satisfies the main requirements of photovoltaic industry: simplicity, low-cost, reliability and direct scalability up to solar panel size [9].

2.2 Nanoparticle fabrication and characterization techniques

2.2.1 Thin film deposition and thermal treatment

Silver (Ag) and aluminum doped zinc oxide (AZO) films were deposited on soda-lime glass substrates using a magnetron sputtering system, which is fully compatible with the industrial manufacturing lines of thin film solar cells. Silver is the material of choice for NPs fabrication, because of its high radiative efficiency and the lowest imaginary permittivity in the visible and near-infrared (NIR) spectrum among the materials commonly used in plasmonics [10, 11]. For the samples presented in section 2.4, the deposition of Ag was carried out at a working pressure of 1.8×10^{-2} mbar in Ar atmosphere with a RF power density of $0.37\,\mathrm{W/cm^2}$. For the samples presented in section 2.5 the depositions of Ag and AZO were carried out at a working pressure of 1.0×10^{-2} mbar in Ar atmosphere with a RF power density of 1 and $2.8\,\mathrm{W/cm^2}$, respectively. Furthermore, a new deposition procedure of Ag has been developed allowing, first, high thickness uniformity over the

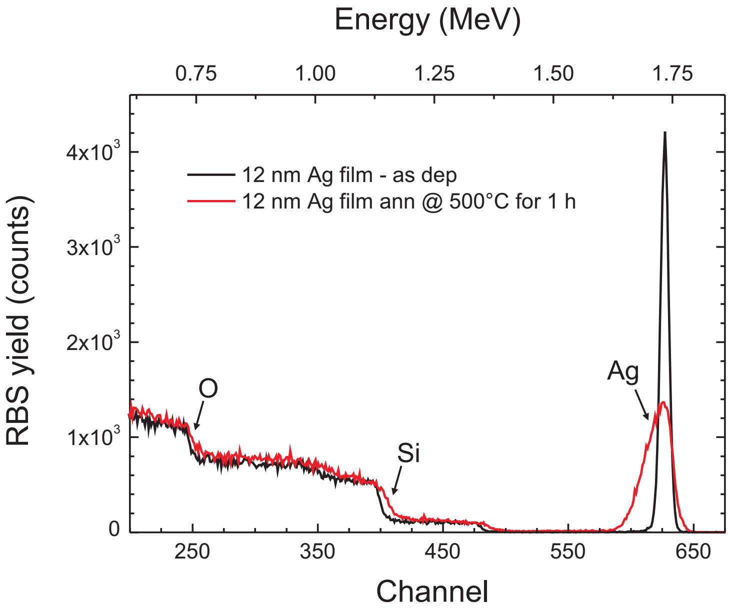

Figure 2.2: RBS spectra of as-deposited 12 nm thick Ag film (black line), and after annealing at 500°C for 1 h (red line). Arrows indicate signal from Ag and elements present in the substrate (Si, O). The doses of Ag were measured as 68.9×10^{15} and 70.2×10^{15} Ag/cm^2, respectively.

2.5×2.5 cm^2 substrate area; and second, high precision of ± 0.35 nm of film thickness among up to 9 substrates processed in one deposition run.

The sputter deposition method of Ag films employed in this work should be beneficial compared to more conventionally-used thermal evaporation technique. The average energy of sputtered species is on the order of several eV, which is an order of magnitude higher than the energy of thermal evaporation [12]. Furthermore, it increases significantly with decreasing working pressure, due to the lowered probability of collisions between atoms. According to the Structure-Zone Model (SZM) [3] for sputter deposition, the relatively high power and low pressure used in the sputtering conditions of this work should result in higher surface mobility of adatoms and, as a consequence, improved quality films in terms of crystallinity and number of voids. A better crystalline quality of the precursor film is expected to result in improved quality of the NPs material.

As-deposited films were found to be continuous except for the thinnest one (6 nm) having a discontinuous, networked morphology. The thicknesses of the Ag and AZO layers were determined from Rutherford Backscattering Spectrometry (RBS, 2.0 MeV He^+ beam in random configuration, at 165° backscattering angle) assuming the Ag density of 5.85×10^{22} Ag/cm^3 and Zn density in AZO of 3.22×10^{22} Ag/cm^3. The relative error of the thickness measurements was estimated at a level of 3%. Fig. 2.2 shows a typical RBS spectrum of a flat Ag film (black line) deposited on soda-lime substrate. Arrows indicate signal from Ag and elements present in the substrate (Si, O).

The post-deposition annealing, in which self-assembled NPs are formed by SSD from the topmost Ag layer, was done at a temperature, T_A, in the range between 200 and 500°C under the flow of nitrogen (2.5 lpm) for 1 h. Due to the film percolation and formation of Ag islands in the SSD process, a drop in the peak counts together with a significant peak broadening was observed in the RBS spectrum, as shown in Fig. 2.2 (red line). The drop of peak counts results from a lower surface coverage, while the peak broadening is due to the thickening of Ag in the NPs points. Furthermore, up to 500°C no significant out-diffusion of Ag atoms occurs during the annealing process as the doses of Ag atoms (obtained from the peak integral) before and after annealing remained approximately unchanged (about 7×10^{16} Ag/cm^2).

For simplicity we shall refer to samples deposited on glass substrate using the abbreviated notation $\mathrm{Ag}_{\mathrm{x\_y}}$, where x is the value of the precursor film thickness in nm and y the annealing temperature in °C.

2.2.2 Statistical analysis of SEM images

The structural properties of the nanostructures were investigated by Scanning Electron Microscopy (SEM) using a field emission Zeiss Supra 25 system. In order to minimize charging effects related to the use of insulating substrates, the measurements were conducted with a low acceleration voltage of 2.5 - 3 kV with an aperture size of 30 μm, and a working distance of around 8 mm using the secondary electron detector.

The statistical analysis of the NPs was based on the digital analysis of SEM images conducted with the Gatan Digital Microscope software package. The particles' area and their in-plane diameter, defined as the longest distance between any two points along the selection boundary, also known as Feret diameter or maximum calliper, which for simplicity we should call particle size, were extracted and used to prepare histograms of NPs counts and surface coverage distributions. The crucial point of the analysis is the determination of the contrast threshold that defines the distinction between the particles and the background. The accuracy of this approach was estimated at two pixels, which corresponds to 14 nm after conversion from pixel to metric units.

2.2.3 Integrated spectrophotometry

The optical properties were measured using a Varian Cary 500 double beam UV-Vis-NIR spectrophotometer equipped with a 4-inch integrating sphere. The geometry of the integrating sphere used allows the collection of the diffused light at angles above 2.1° away from the normal direction together or apart from the specular part in both transmission and reflection mode. The integrated measurements of the total and diffused transmission (T_{Total} and T_{Diff}, respectively) as well as the total and diffused reflection (R_{Total} and R_{Diff}, respectively) were performed, parasitic absorption in the NPs (Abs) was calculated as:

$$Abs = 100\% - T_{Total} - R_{Total} - Abs_{Substrate} \tag{2.3}$$

and the extinction (Ext), representing all types of interaction between light and NPs, as:

$$Ext = Abs + R_{Total} + T_{Diff} - Ext_{Substrate} \tag{2.4}$$

where the background effect of the substrate has been subtracted from original measurements.

2.3 Theoretical background

As discussed in the introduction, for application in solar cells it is important to study the far-field optical properties of NPs. In any far-field application, however, the scattering and absorption of NPs as well as the directionality of scattered light, can limit the parameter space where NPs can provide improvements to the properties of the surrounding receiving materials. Therefore, a theoretical study is important prior to any practical implementation [13].

The amount of light scattered (absorbed) by a NP is determined by its scattering (absorption) cross-section, C_{Scatt} (C_{Abs}), a quantity with dimensions of an area given by the ratio between the energy scattering (absorption) rate, W_{Scatt} (W_{Abs}), and the incident irradiance, I_0 [14]:

$$C_{Scatt} = \frac{W_{Scatt}}{I_0} \qquad C_{Abs} = \frac{W_{Abs}}{I_0} \tag{2.5}$$

In the literature of single particle scattering, however, it is more usual to represent the dimensionless scattering (absorption) efficiency, Q_{Scatt} (Q_{Abs}), which is the ratio between C_{Scatt} (C_{Abs}) and the particle cross-sectional area, A:

$$Q_{Scatt} = \frac{W_{Scatt}}{I_0 A} \qquad Q_{Abs} = \frac{W_{Abs}}{I_0 A} \tag{2.6}$$

Extinction efficiency (Q_{Ext}) is then calculated as a sum of the two, scattering and absorption efficiencies:

$$Q_{Ext} = Q_{Scatt} + Q_{Abs} \tag{2.7}$$

Figure 2.3 depicts the far-field characteristics (Q_{Scatt}, Q_{Abs} and Q_{Ext}), computed using the analytical Mie theory formalism [14], of a single, spherical Ag NPs with distinct diameters, D: (a) 10 nm, (b) 50 nm, (c) 100 nm, (d) 200 nm. The particles are taken to be embedded in a uniform medium with refractive index $n_m = 1.25$ in order to model the effective medium for NPs supported on glass substrate and surrounded by air [15].

Particles much smaller than the wavelength (e.g. $D = 10$ nm) scatter in the electrostatic regime as dipoles. The amount of light that they radiate through scattering is low, since most of the impinging light is absorbed inside the particle material (parasitic absorption). Therefore, in the case of Fig. 2.3(a), $Q_{Ext} \simeq Q_{Abs} \gg Q_{Scatt}$. As the size increases, Q_{Scatt} becomes higher and Q_{Abs} lower. In the $D = 50$ nm case, shown in Fig. 2.3(b), both these quantities are similar and there is an increase in the maximum extinction cross section (C_{Ext}) by two orders of magnitude relative to the smallest particles. A further increase in the particle size to $D = 100$ nm, Fig. 2.3(c), leads to the appearance of a quadrupole mode and to a red-shift in the dipolar resonance. For sizes of 100 nm or higher, $Q_{Abs} \ll Q_{Scatt}$ especially at the dipolar mode. Furthermore, the dipolar mode of Q_{Scatt} is located at longer wavelengths than the respective Q_{Abs} mode. These effects are even more evidenced when the size is increased to $D = 200$ nm, Fig. 2.3(d), namely there is a pronounced red-shift of the Q_{Scatt} peaks relative to the

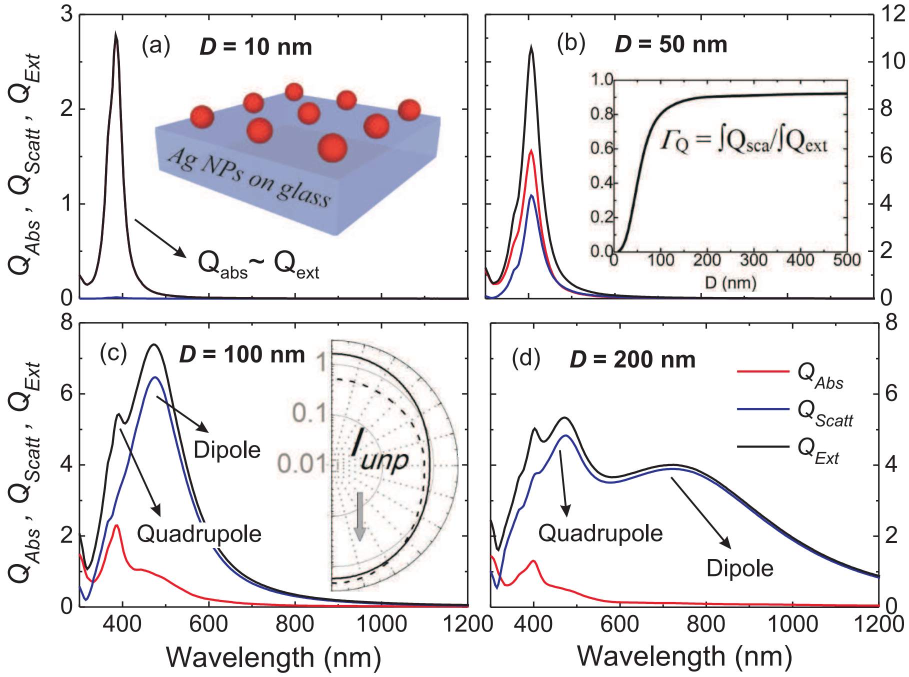

Figure 2.3: Spectra of the extinction (Q_{Ext}), scattering (Q_{Scatt}) and absorption (Q_{Abs}) efficiencies of individual Ag NPs, computed with Mie theory. The NPs are taken to be spherical with diameter D, and immersed in a medium with refractive index $n_m = 1.25$ corresponding to the effective refractive index surrounding NPs deposited on glass. The diameters of the NPs are (a) 10, (b) 50, (c) 100 and (d) 200 nm. The inset in (b) plots the ratio between the integrals of Q_{Scatt} and Q_{Ext} over the represented spectral range, as a function of the particle diameter. The log-scale polar plot in (c) shows the dimensionless unpolarized scattered irradiance I_{unp} at the Q_{Ext} peaks (in solid/dashed line for the dipole/quadrupole peak), revealing the preferential forward scattering of light at the quadrupole mode. The grey arrow indicates the illumination direction.

previous cases, the quadrupolar peak intensity increases and the dipolar peak becomes smaller and broader.

The performance of the particles as broadband scatterers can be evaluated by the quantity $\mathit{\Gamma}_Q$:

$$\mathit{\Gamma}_Q = \frac{\int Q_{Scatt}}{\int Q_{Ext}}, \tag{2.8}$$

which is the integral of Q_{Scatt} divided by the integral of Q_{Ext} over the investigated wavelength range. This quantity, plotted in the inset of Fig. 2.3(b), increases with the particle size, since the bigger the particle the more dominant is Q_{Scatt} relative to Q_{Abs}. However, there is also an increasing number of higher-order modes appearing in the Q_{Scatt} spectrum which leads to the observed saturation of $\mathit{\Gamma}_Q$ for diameters above $\sim 150\,\mathrm{nm}$. Above such size the resonant character of the particles starts vanishing and their spectra become more size-independent in the integrated wavelength range.

The inset in Fig. 2.3(c) shows the dimensionless unpolarized scattered irradiance I_{unp} at the Q_{Ext} peaks (in solid/dashed line for the dipole/quadrupole peak) and the grey arrow indicates the illumination direction. This reveals that at the dipole mode scattering of light is uniformly distributed over the angles, while at the quadrupole it is preferentially scattered in forward direction. Such effect becomes more pronounced (not shown) as the particle size increases. Although the maximum values of Q_{Scatt} tend to decrease with increasing NPs' size (above 50 nm), the absolute values of the cross-section C_{Scatt} increase (see Table 2.1).

The far-field optical properties of single, spherical particles with diameters (a) 10, (b) 50, (c) 100 and (d) 200 nm embedded in AZO (refractive index approximately 2.05 at 500 nm) are shown in Fig. 2.4. Also in this case, the optical response of the smallest particles ($D = 10\,\mathrm{nm}$, Fig. 2.4(a)) is dominated by the parasitic absorption, which decreases substantially with increasing particle size. The scattering part start to play a dominant role for NPs bigger than 100 nm.

In addition to Figs. 2.3 and 2.4 the comparison between the NPs placed on glass and the NPs embedded in AZO, in terms of spectral position of dipole (λ_d) and quadrupole (λ_q) peaks and respective values of scattering, absorption and extinction cross-sections is summarized in Table 2.1. AZO is a material with a higher refractive index than the one of effective medium used for NPs deposited on glass and as such it impacts significantly the resonance characteristics obtained for same sizes of NPs causing namely:

Table 2.1: Values of scattering (C_{Scatt}), absorption (C_{Abs}) and extinction (C_{Ext}) cross-sections of single, spherical nanoparticles with diameter D, computed using the analytical Mie formalism, at dipole (λ_d) and quadrupole (λ_q) extinction peaks. Parameter $\mathit{\Gamma}_C$ describes the scattering performance as the ratio between scattering and absorption cross-sections ($\mathit{\Gamma}_C = C_{Scatt}/C_{Abs}$)

		Quadrupole mode					Dipole mode				
D		λ_q	C_{Scatt}	C_{Abs}	C_{Ext}	$\mathit{\Gamma}_C$	λ_d	C_{Scatt}	C_{Abs}	C_{Ext}	$\mathit{\Gamma}_C$
nm		nm	$10^{-14}\,\mathrm{m}^2$				nm	$10^{-14}\,\mathrm{m}^2$			
10	Glass						384	1×10^{-4}	0.02	0.02	0.01
	AZO						484	2×10^{-3}	0.06	0.06	0.04
50	Glass						406	0.87	1.22	2.08	0.41
	AZO						536	1.85	0.78	2.63	0.70
100	Glass	391	2.55	1.71	4.26	0.60	472	5.07	0.74	5.80	0.87
	AZO	506	4.32	1.48	5.81	0.74	663	4.98	0.38	5.37	0.93
150	Glass	421	8.44	2.49	10.9	0.77	578	8.44	0.39	8.87	0.96
	AZO	581	10.1	1.02	11.1	0.91	826	8.08	0.27	8.35	0.97
200	Glass	471	15.2	1.60	16.8	0.91	722	12.2	0.36	12.6	0.97
	AZO	670	14.9	0.84	15.7	0.95	1012	11.7	0.34	12.0	0.97

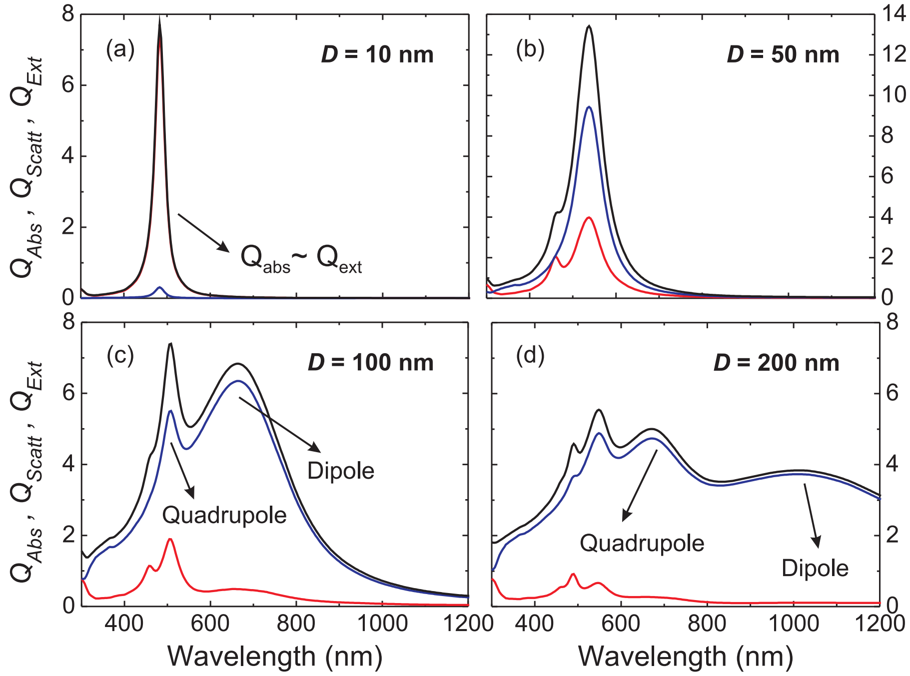

Figure 2.4: Spectra of the extinction (Q_{Ext}), scattering (Q_{Scatt}) and absorption (Q_{Abs}) efficiencies of individual Ag NPs, computed with Mie theory. The NPs are taken to be spherical with diameter D, and immersed aluminium doped zinc oxide (AZO). The diameters of the NPs are (a) 10, (b) 50, (c) 100 and (d) 200 nm.

(i) the red-shift of the plasmonanic resonance; (ii) spectral broadening; (iii) the increase of the resonance intensity C_{Ext} for NPs smaller than 100 nm; and (iv) the presence of high order modes in the spectra of smaller particles.

The scattering performance can be evaluated by considering a parameter $\mathit{\Gamma}_C$, defined as the ratio between scattering and absorption cross-sections at the wavelength of dipole or quadrupole mode:

$$\mathit{\Gamma}_C = \frac{C_{Scatt}}{C_{Abs}} \tag{2.9}$$

The most significant effect of higher refractive index is that the $\mathit{\Gamma}_C$ is readily increased for scattering at the dipole mode, for NPs smaller than 100 nm, as well as at the quadrupole mode for bigger NPs. The effect originates from both, increased C_{Scatt} and increased spectral separation between scattering and absorption peaks. In the view of application in photovoltaics, the gain in Γ_C results in the desirable suppression of parasitic absorption.

NPs formed by post-deposition annealing of a thin film have, in general, a hemispherical shape which cannot be accounted for with Mie theory since it is only valid for spherical geometries. In addition, the assumption of a uniform effective medium surrounding the particles neglects the refractive index discontinuity at the interface with air. Such discontinuity causes a preferential forward scattering of the light to the higher-index medium, and also originates backreflected fields (retarded potentials) that may disturb the internal and scattered field produced by the NPs. Therefore, the Mie analysis presented in this section is only intended to provide a first-order estimation of the NP sizes that should be aimed for the fabrication process, and to assist in the interpretation of the optical results.

2.4 Nanoparticles formed on glass substrate

2.4.1 Structural properties

Figure 2.5 shows SEM images, together with corresponding size distributions and SC histograms, for a thickness, t_{Ag}, of 7.5 nm and three different annealing temperatures, T_A. In the low annealing temperature regime, up to 250°C, the formation of irregular and elongated clusters occurs. In this case, due to uncertainties in definition of particle size, histograms are not available. With increasing T_A from 250 to 350°C both the size and shape uniformity of the particles increase significantly. A further increment in T_A up to 450°C initiates an aggregation process of NPs as evidenced by the strong decrease in the number of particles smaller than 60 nm. Therefore, both particle counts and surface coverage distributions become narrower, more symmetric and closer to Gaussian distributions. Although in both samples $\mathrm{Ag}_{7.5\_350}$ and $\mathrm{Ag}_{7.5\_450}$ the maximum size of NPs is 180 nm, the mean SC size of NPs, determined by the maximum of Gaussian single-peak fitting to the SC distribution, was found to increase from 75.1 ± 0.8 to 86 ± 0.5 nm. At the same time, the full width at half maximum (FWHM) decreased from 51 to 41.5 nm. In addition, the total SC decreases from 26.6% for $\mathrm{Ag}_{7.5\_350}$ to 24.2% for $\mathrm{Ag}_{7.5\_450}$, and since no noticeable loss of silver occurred during the annealing process, it can be concluded that the mean height of the particles increases with T_A. Furthermore, the shape

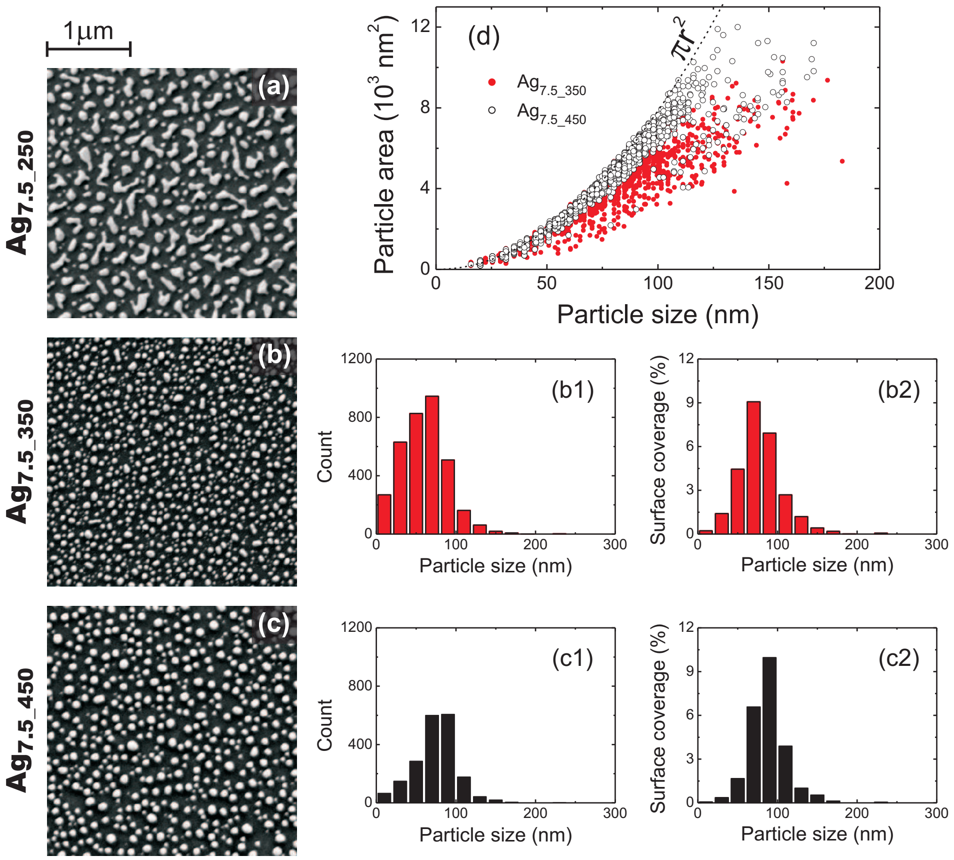

Figure 2.5: SEM images of Ag NPs formed after annealing of 7.5 nm thick precursor film for (a) 1 h at 250°C, (b) 350°C and (c) 450°C. Size (in-plane diameter) and surface coverage (SC) distributions of samples Ag$_{7.5\_350}$ and Ag$_{7.5\_400}$ (with well-defined NP size) are shown in (b1, b2) and (c1, c2), respectively. (d) The dependence of the particle area against particle size for the same precursor film thickness (7.5 nm) and different annealing temperatures, 350°C and 450°C. Points for perfectly round NPs should lie along the dashed πr^2 curve.

uniformity in terms of in-plane roundness of the particles increases with annealing temperature, as shown in the plot of particle area against particle size (longitudinal diameter) in Fig. 2.5(d). The particles that are perfectly round should lie along the dashed πr^2 curve in the plot. For both samples $\mathrm{Ag}_{7.5\_350}$ and $\mathrm{Ag}_{7.5\_450}$ particles with diameter below 60 nm are approximately round, whereas bigger particles are more elongated. Nonetheless, the roundness of NPs is significantly increased when T_A increases to 450°C.

A similar evolution of NPs' morphology was also observed for thicker precursor films. Fig. 2.6 shows SEM images, together with corresponding size distributions and SC histograms, for a t_{Ag} of 10.5 nm annealed in the same range of temperatures as 7.5 nm samples. First, up to the T_A of 250°C a formation of irregular NPs was observed whereas the well defined and ellipsoidal NPs were obtained from T_A of 350°C. With a further increase of T_A up to 450°C size uniformity of the NPs increases and the number of small particles decreases which exhibits in the narrowing of the particle counts distribution. Furthermore, the mean SC size of NPs increases from 136 ± 0.8 up to 149 ± 0.5 nm, with almost unchanged FWHM of 78.5 nm, and the total SC decreases from 25.1% for $\mathrm{Ag}_{10.5\_350}$ to 23.5% for $\mathrm{Ag}_{10.5\_450}$. Therefore the mean height of the NPs is expected to increases with T_A. Similarly to the case of 7.5 nm, the NPs smaller than 100 nm are approximately round for both $\mathrm{Ag}_{10.5\_350}$ and $\mathrm{Ag}_{10.5\_450}$ while the bigger NPs are rounder when formed at 450°C as shown in Fig. 2.6(d). Recently, Sun et. al. [16] reported similar temperature-dependent morphology evolution (decrease of surface coverage and increase of height and circularity of NPs) of nanostructures fabricated by rapid thermal annealing of thin gold films.

Figure 2.7 shows SEM images and the corresponding histograms for NPs prepared from t_{Ag} of 16 nm annealed at T_A of 250°C, 400°C and 500°C. For this thickness a T_A of 200°C was found to be a threshold value for nanostructure formation, below which the morphology of the film does not change significantly with respect to the as deposited film. Thinner films annealed at 200°C (samples $\mathrm{Ag}_{7.5\_200}$, $\mathrm{Ag}_{10.5\_200}$ and Ag_{12_200}) form irregular nanocluster structures similar to the already discussed $\mathrm{Ag}_{7.5\_250}$ and $\mathrm{Ag}_{10.5\_250}$. The same type of NPs morphology was observed for a t_{Ag} of 16 nm above the threshold temperature, Fig. 2.7(a). An increase of T_A up to 400°C leads to the formation of two distinctive types of NPs, which originates a double-peak distribution in the SC histogram and is evident in the SEM image of Fig. 2.7(b). The values of the mean SC size for the small

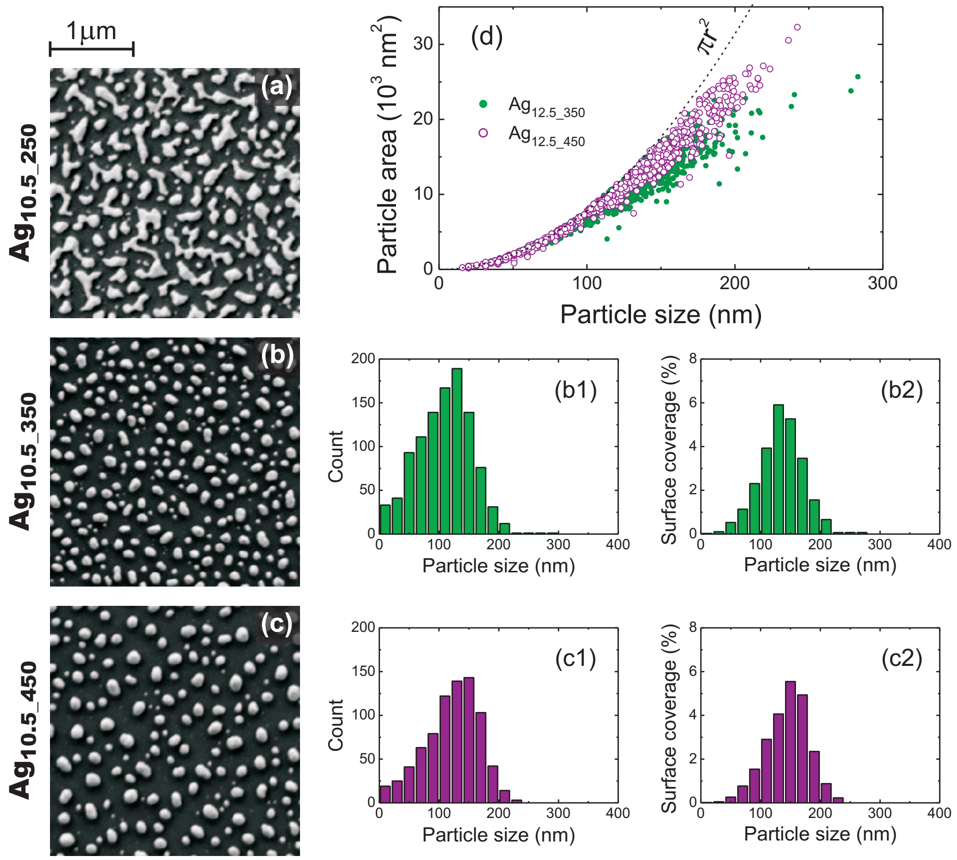

Figure 2.6: SEM images of Ag NPs formed after annealing of 10.5 nm thick precursor film for (a) 1 h at 250°C, (b) 350°C and (c) 450°C. Size (in-plane diameter) and surface coverage (SC) distributions of samples $\mathrm{Ag}_{10.5\_350}$ and $\mathrm{Ag}_{10.5\_450}$ (with well-defined NP size) are shown in (b1, b2) and (c1, c2), respectively. (d) The dependence of the particle area against particle size for the same precursor film thickness (10.5 nm) and different annealing temperatures, 350°C and 450°C. Points for perfectly round NPs should lie along the dashed πr^2 curve.

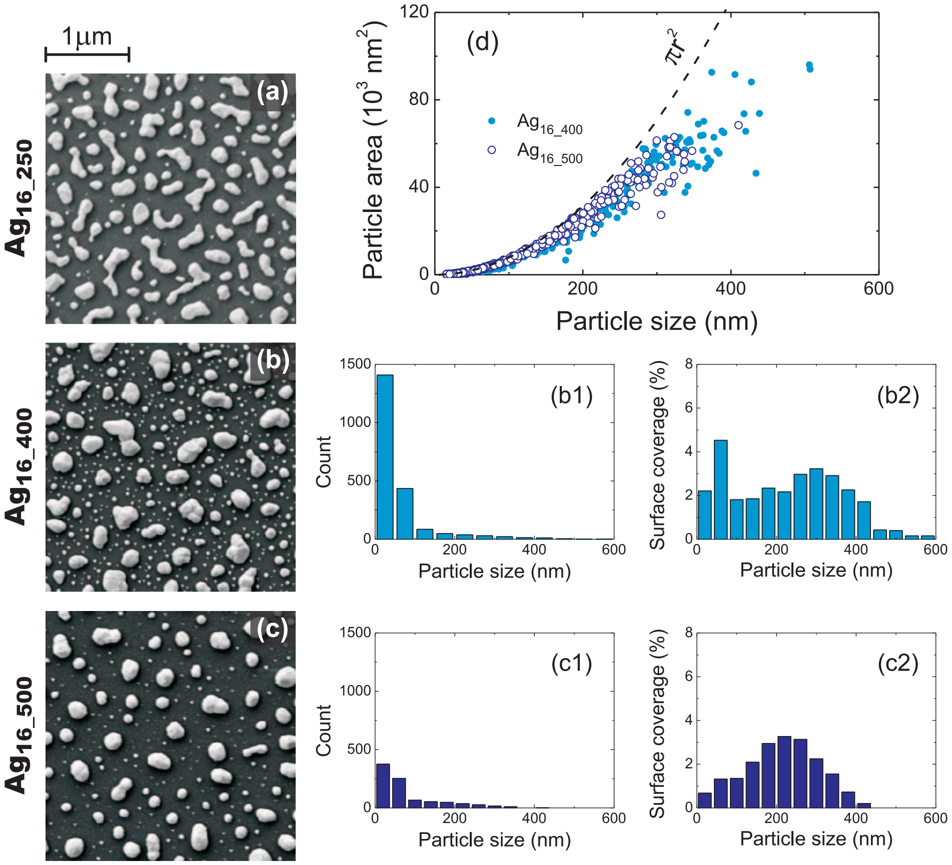

Figure 2.7: SEM images of Ag NPs formed after annealing of 16 nm thick precursor film for (a) 1 h at 250°C, (b) 400°C and (c) 500°C. Size (in-plane diameter) and surface coverage (SC) distributions of samples Ag_{16_400} and Ag_{16_500} (with well-defined NP size) are shown in (b1, b2) and (c1, c2), respectively. (d) The dependence of the particle area against particle size for the same precursor film thickness (16 nm) and different annealing temperatures, 400°C and 500°C. Points for perfectly round NPs should lie along the dashed πr^2 curve.

and large NPs can be found from a double Gaussian peak fitting. In case of sample Ag_{16_500}, a great number of small NPs with a mean SC size of $53 \pm 3\,\text{nm}$ is spread among a fewer number of much larger particles with a mean SC size of $280 \pm 8\,\text{nm}$. Such morphology was not observed for films thinner than 16 nm.

Further increase of T_A up to 500°C causes a rapid decline of the number of small NPs and a transition to a single-peak SC distribution, Fig. 2.7(c2). Since there is no significant loss of Ag during the annealing, and the total SC is reduced (from 26% for Ag_{16_400} to 19.5% for Ag_{16_500}), the mean height of the NPs is increased also in this case. This is accompanied by a slight increase of the NPs roundness, as shown on the plot of particle area vs. particle size in Fig. 2.7(d). The observed mechanism of nanostructure evolution can be explained in terms of the Ostwald ripening process. The surface mobility of silver atoms is proportional to the annealing temperature. Thus, for sufficiently high T_A, the surface diffusion length is higher than the average distance between the particles allowing their aggregation and the formation of more energetically favored big particles. High atomic diffusion at high temperature also allows the formation of uniform round-shaped NPs, since it tends to minimize the particles surface tension.

After the structural analysis of more than 30 samples, it was concluded that the obtained nanostructures can be categorized according to their morphology into four groups: thin films (F), irregular NPs (I), double-peak (D) and single-peak (S) distributions. Each group is formed in a specific range of fabrication parameters (precursor film thickness and annealing temperature) that can be represented as a certain area on the t_{Ag} against T_A diagram shown in Fig. 2.8. Such graph can be considered as a structural-phase diagram of nanostructure formation. It should be clarified that the classification was found to be independent of the bin width in the SC histograms. The temperature threshold for dewetting increases with film thickness, in agreement with the dependence found by Kim et. al. [17]. For layers thinner than 12 nm, the D-type structure is not formed at all or formed in a very narrow temperature range, thus, a direct transition from I-type to S-type nanostructure with increasing T_A was observed. Above 12 nm D-type nanostructures are formed between I-type and S-type regions, whose domain widens significantly with increasing t_{Ag}. Therefore, since the annealing temperature is limited to 500°C, S-type structures were not obtained above 16 nm. It was also observed that extended annealing time does not

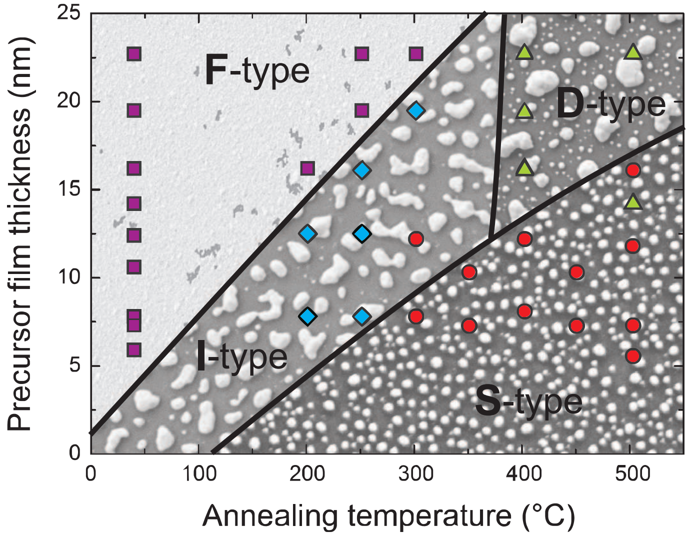

Figure 2.8: Structural-phase diagram of NPs formation. The morphology of annealed thin films can be categorized into four groups: thin film (F-type, violet squares), irregular NPs (I-type, blue diamonds), double-peak surface coverage size distribution (D-type, green triangles) and single-peak surface coverage size distribution (S-type, red circles). Each type is formed in a specific range of fabrication conditions. The background SEM images illustrate each type of morphology.

change the temperature threshold for film dissolution, neither the transition from I to S or D-type nanostructure.

Figure 2.9 shows the mean size of the SC distributions as a function of t_{Ag}. When the NPs are characterized by a D-type distribution, the mean SC size was shown for both the small and large particle peak. An almost linear increase in the mean SC size with the precursor film thickness was observed, regardless of the annealing temperature. This demonstrates that the initial film thickness is the main parameter determining the mean SC size, whereas the annealing temperature is responsible for obtaining round NPs. A linear dependence of average particle size against precursor film thickness for dewetted gold films has also been obtained by Kojima et. al. [18]. Additionally, for the D-type structures the mean SC size of the small particles remains almost constant regardless of the precursor film thickness.

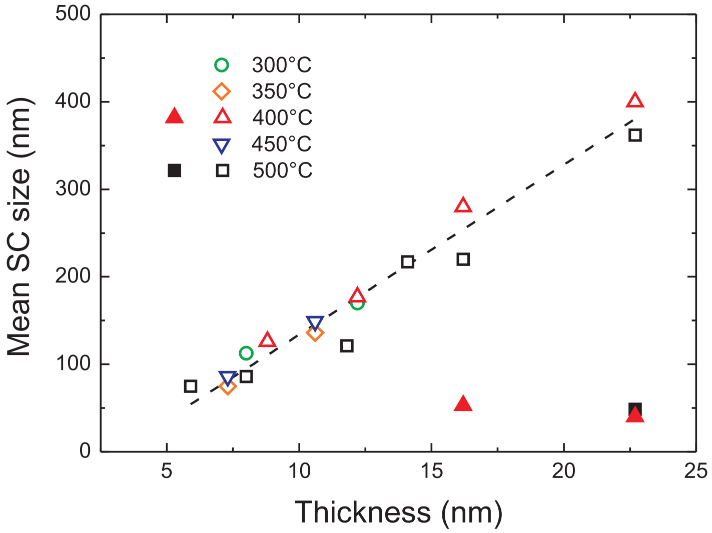

Figure 2.9: Dependence of the mean surface coverage (SC) size on film thickness for well-defined Ag NPs (S and D-type). The solid symbols indicate the mean SC size of the small particles peak in D-type distribution.

2.4.2 Optical properties

The optical properties of the nanostructures discussed in the previous section are shown in Fig. 2.10, for t_{Ag} of 7.5 nm in the left column, 10.5 nm in the center column and 16 nm in the right column, which corresponds to the nanostructures shown in Figs. 2.5, 2.6 and 2.7, respectively. The background effects of the glass substrate, in terms of its reflection and absorption, were subtracted from the raw optical measurements. Therefore, the plots presented in Fig. 2.10 show the optical properties of the NPs only, though in the presence of the glass substrate. However, in certain wavelength ranges where NPs interact strongly with incident light, such subtraction can cause a slight underestimation of the total reflection from the NPs. For this reason, the diffused reflection of sample Ag_{16_500} exhibits higher values than the total one in the near UV. Furthermore, the absorption spectrum of soda-lime glass has a sharp edge at 350 nm so below this value the absorption of NPs is masked by the substrate. As such, data below 350 nm have no

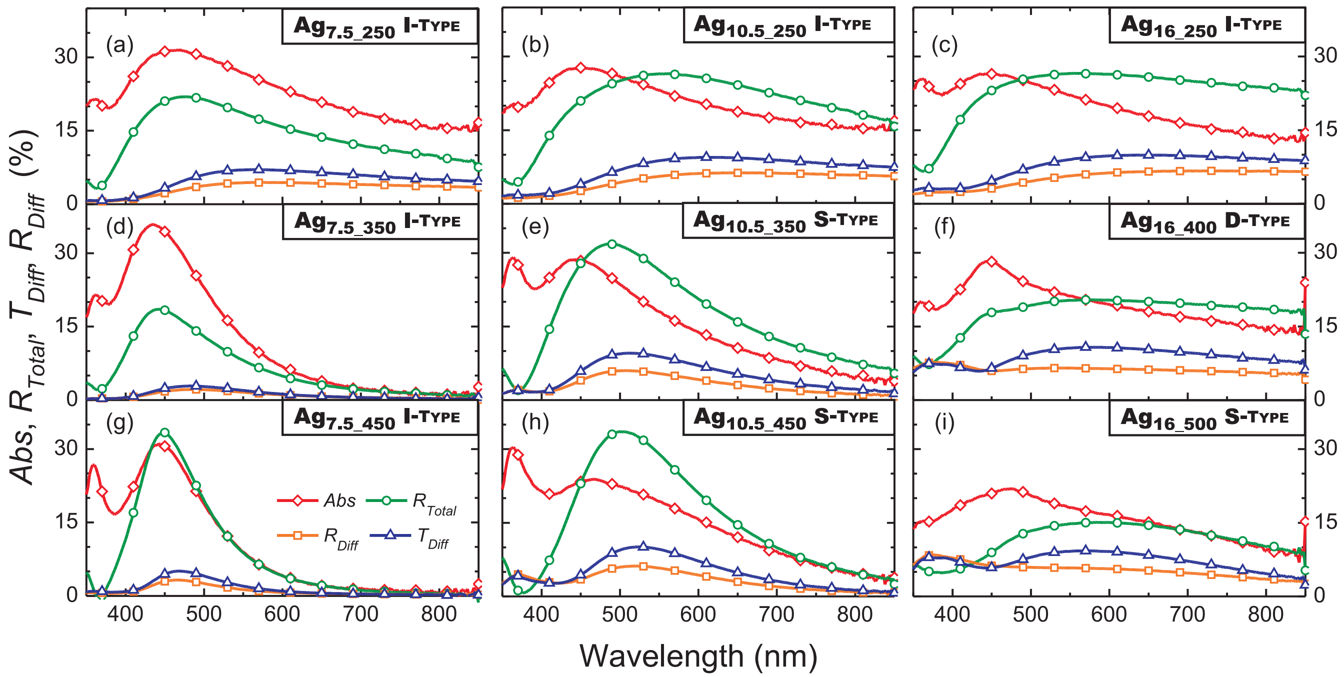

Figure 2.10: Absorption (*Abs*), total reflection (R_{Total}) and diffused parts of transmission (T_{Diff}) and reflection (R_{Diff}) of 7.5 nm (left column), 10.5 nm (center column), and 16 nm (right column) thick Ag precursor film annealed in the range of temperatures between 250°C and 500°C

significance and are not shown.

All investigated I-type nanostructures, in particular samples $\mathrm{Ag}_{7.5\_250}$, $\mathrm{Ag}_{10.5\_250}$ and Ag_{16_250}, exhibit optical features with wide spectral response, as expected from the large spread in NPs size and shape. As the NPs become bigger with increasing t_{Ag} a broadening of the R_{Total} and Abs spectra was observed. The total reflection of Ag_{16_250}, as well as the diffused parts of reflection and transmission, are roughly doubled with respect to $\mathrm{Ag}_{7.5\_250}$ and almost the same with respect to $\mathrm{Ag}_{10.5\_250}$, whereas the absorption is only slightly smaller. The absorption of the NPs in sample $\mathrm{Ag}_{7.5\_250}$ clearly dominates over their scattering properties in all the investigated wavelength range, while for $\mathrm{Ag}_{10.5\_250}$ and Ag_{16_250} the reflection is higher than absorption for wavelengths above 500 nm.

For t_{Ag} of 7.5 and 10.5 nm the increase in T_A leads to a clear narrowing of the spectral response, which is related to the formation of the S-type structure with higher size and shape homogeneity. For both thicknesses, comparison between samples formed at 350°C and 450°C shows a clear decrease of absorption and increase of reflection and scattering for higher T_A, which results from the increased mean size of the NPs as well as from the reduction in the number of small particles (size < 60 nm). On the other hand, the spectral narrowing of the optical characteristics results from narrower size distribution and increased roundness of the NPs. Two distinguishable peaks are present in the spectra (most clearly seen in Abs spectra): a narrow peak at approximately 360 nm and a broad one at longer wavelengths. The later one corresponds to the dipolar mode of the big NPs and clearly red-shifts with increasing NP size (for R_{Total} from ~ 450 for $\mathrm{Ag}_{7.5\_450}$ to ~ 510 nm for $\mathrm{Ag}_{10.5\_450}$). On the other hand, the peak remains at approximately the same wavelengths with increasing T_A because there is not only an increase in the particle size (which red-shifts the resonance) but also a reduction in the elongation of the particles shape and increase of their height making them more spherical (which blue-shifts the resonance). The short wavelength peak, however, can originate from three different effects: a plasmonic resonance of the small NPs (dominated by absorption), a quadrupole mode sustained by the bigger NPs and a mode related to the shorter diameter of ellipsoidal NPs. We attribute this peak to the quadrupole mode as it becomes more evidenced with increasing particle size but not with the increasing number of small particles. For spherical particles such mode should be excited by the particles with sizes close to or above 100 nm, as shown in the computed plot of Fig. 2.31(c).

The nanostructures fabricated from t_{Ag} of 16 nm have a wide optical response, regardless of the annealing temperature. The increase of T_A from 250°C to 500°C leads to a reduction in the parasitic absorption with only a slight decrease in diffused reflection and transmission. The decrease in total reflection intensity with increasing T_A can be, however, related to a decrease in the total surface coverage from 31.5% for Ag_{16_250} to 19.5% for Ag_{16_500}. These structures exhibit a less clear distinction between the resonance peaks, as compared with $\mathrm{Ag}_{7.5}$ and $\mathrm{Ag}_{10.5}$ samples. This is because the sizes of the particles in Ag_{16} samples are bigger and less homogeneous, so their scattering spectra present additional higher-order modes which reduce in the resonant character of the NP structures.

All investigated D-type nanostructures, in particular sample Ag_{16_400}, have a characteristic absorption peak in the wavelength range $400-475$ nm. The main difference between sample Ag_{16_400} and Ag_{16_500} is the presence of a great number of small NPs with a size distribution ranging from 0 to 100 nm and a SC peak at 60 nm. This distribution is comparable to sample $\mathrm{Ag}_{7.5\_500}$, which has a sharp resonance peak in Abs and R_{Total} with a maximum at 450 nm. Therefore, it can be concluded that the absorption peak present in Ag_{16_400} is directly related to the small NPs peak in the surface coverage histogram. The lack of an analog feature in the Abs spectra of the S-type sample Ag_{16_500}, as well as the decrease of R_{Total} in the wavelength range $375-525$ nm compared to Ag_{16_400}, supports the above hypothesis. The absorption of Ag_{16_500} is reduced with respect to sample Ag_{16_400} in the whole investigated spectral range. For wavelengths below 500 nm, such reduction is attributed to the lower number of small NPs. For wavelengths above 500 nm the reduction should be due to the decrease in the mean SC size and to the fact that the big NPs become more spherical (with higher height/width ratio) which leads to a blue-shift of their dipolar resonance.

For a certain refractive index surrounding media, the plasmonic resonance can be tuned by the NPs' size and shape. Fig. 2.11 depicts the spectral red-shift of the dipolar resonance wavelength, in terms of the position of the extinction (*Ext*) peak, with increasing mean SC size of the NPs. Approximately linear correlation was found to hold, apart from samples annealed at 300°C having resonance at shorter wavelengths than samples annealed at higher temperatures. This can be due to different mean height of the NPs. By increasing the mean SC size from 80 to 220 nm the resonance shifts from

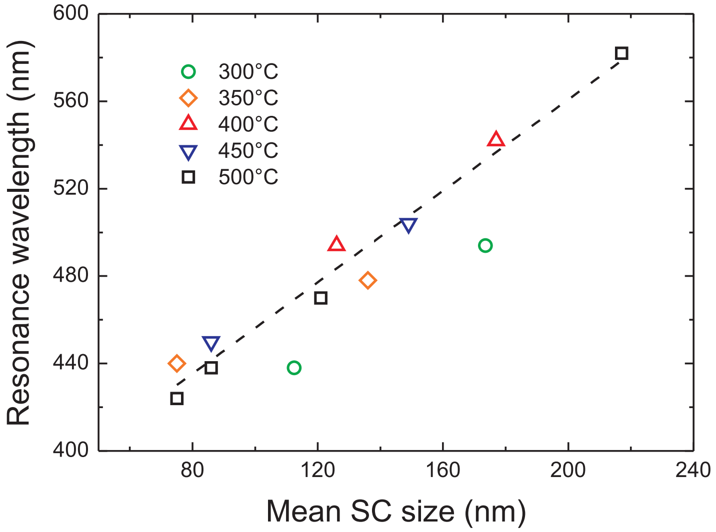

Figure 2.11: Dependence of the resonance wavelength, in terms of extinction peak position, on the mean surface coverage (SC) size.

420 up to 580 nm which gives an average shift of 1.05 ± 0.07 nm/nm determined from a linear fit for samples annealed in the 350 − 500°C range. The linear relation reveals that the main parameter determining the resonance wavelength is the size of the NPs, which is directly proportional to the precursor film thickness, whereas the variations in NPs' shape play only a second order role.

The important issue affecting the optical properties of NPs is a tarnishing of silver when stored in air. Silver is well known to react with hydrogen sulfide (H_2S), present in the atmosphere due the air pollution, to form a metallic silver core- and silver sulfide shell structure (Ag^0/Ag_2S) [19, 20]. As Ag_2S is a strongly absorbing material in the visible range, the sulfidation of the NPs results in a considerable decrease of the plasmonic resonance strength, namely in the reduction of R_{Total}, R_{Diff} and T_{Diff} and increase of Abs. Such ageing effect is depicted in Fig. 2.12, on the example of NPs formed from 12 nm thick Ag film annealed at 400°C, by comparing their optical properties immediately after fabrication and after 8 weeks storage

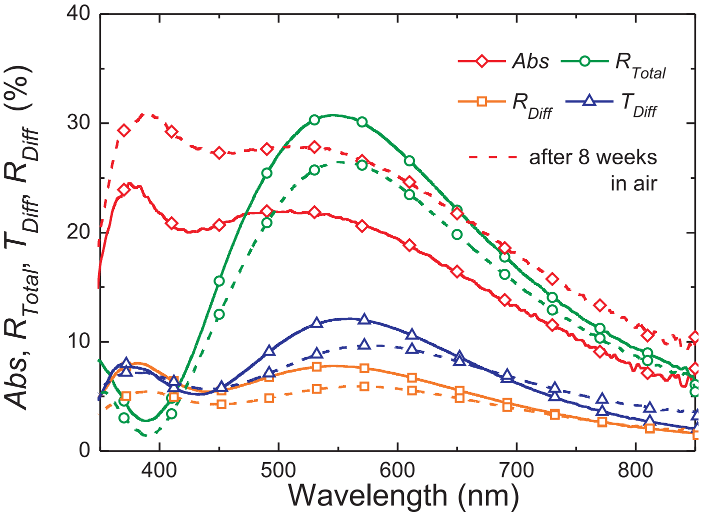

Figure 2.12: The effect of silver tarnishing (sulfidation) on the optical properties of the NPs fabricated from 12 nm thick Ag film annealed at 400°C for 1 h. Solid lines correspond to the measurements done immediately after fabrication, and dashed to the measurements after 8 weeks storage in air.

in air atmosphere. In addition a slight 10 nm red-shift of the *Ext* peak was observed after storage.

2.4.3 Discussion of optical results

One of the main conclusions that can be drawn from the optical data is that, for all types of nanostructures, small (size < 60 nm) particles do not significantly contribute to the optical properties in Fig. 2.10 (in particular to parasitic absorption) for wavelengths above 600 nm. That is shown in the computed efficiencies of Fig. 2.3(a,b), which vanish for wavelengths above 600 nm. Even below this wavelength, at their plasmonic resonance, the maximum C_{Ext} of particles with size below 60 nm is considerably smaller than that of the bigger particles such as those of Fig. 2.3(c,d). This means that the small particles provide relatively little interaction with the incoming light, so their far-field optical effects are small in comparison with those of the bigger particles. Therefore, the big particles have the strongest impact on the scattering properties of the nanostructures, even though the total number of big (size $>$ 60 nm) particles is lower than that of small ones (see size distribution histograms of Figs. 2.5, 2.6 and 2.7). As scattering and absorption tend to increase with the particle size, the measured optical features are mostly determined by the particles that cover the largest area of the sample. So, the surface coverage size distribution is the key parameter to describe the correlation between the morphology and optical response of the NP structures. For instance, in the case of the D-type structures, there can be a significant contribution from the small particles only for wavelengths below 600 nm and only if their SC is comparable to that of the big particles.

According to the theoretical results described in section 2.3, the optical properties of spherical NPs with diameter above 100 nm should be dominated by scattering, especially in the visible and NIR region. However, all our fabricated samples suffer from high parasitic absorption which extends over the wavelength range of the reflection and transmission peaks in Fig. 2.10. This unexpectedly high absorption can be attributed to the polycrystalline nature of the material forming the NPs, since collectively oscillating electrons lose their energy in interactions with grain boundaries, defects or surface roughness [11]. Consequently, energy dissipation inside polycrystalline material causes an increase in the light absorption and a decrease in the scattering intensity at the plasmonic resonance [9, 21]. It has been found that, due to this effect, surface plasmon propagation lengths are several times longer in single crystal nanowires than in polycrystalline ones [22]. In this respect, colloidal NPs synthetized chemically are advantageous as, due to their highly crystalline structure [23], the optical properties closely match electrodynamic calculations [24].

As previously referred, the quantities plotted in Fig. 2.10 present a broad dipole peak and another peak at shorter wavelengths caused by higher-order plasmonic modes sustained by the big NPs. These modes scatter the light more preferentially along the forward direction, while the dipolar mode scatters more uniformly over all angles [14], as seen in the polar plot of Fig. 2.3(c). As such, for the application of these structures in solar cells it is advantageous to make use of their dipolar resonance, since it is preferable to scatter the light rays at angles the further away as possible from the incidence direction in order to increase their optical path length inside the cell material.

Another relevant aspect to the application in PV, is the increase in the spectral separation between the scattering and absorption peaks as the particle size increases. This effect is seen in the Mie plots of Fig. 2.3, which show that when the size is increased the Q_{Scatt} peaks red-shift significantly, whereas the Q_{Abs} peak remains at approximately the same wavelengths. The same trend is observed for the measured peaks. For NPs with the mean SC size smaller than 90 nm (i.e samples $\text{Ag}_{7.5\_350}$ and $\text{Ag}_{7.5\_450}$) both Abs and R_{Total} are peaked at the same wavelength while for bigger mean SC sizes the two peak start to separate spectrally and the separation increases with increased NPs' size (i.e samples $\text{Ag}_{10.5\_450}$ and Ag_{16_500}). This effect is advantageous for incorporation NPs in the rear side of the solar cell, as they only interact with the wavelengths that are not absorbed in a first pass through the cell material (typically those above 500 nm for a-Si:H thin-films). Therefore, if the particles absorption peak is located below 500 nm and the scattering peak above such wavelength, they should not cause significant light dissipation in the cell while contributing to the light trapping.

2.4.4 Evaluation of scattering performance

The most important issue for application in solar cells is the competition between optical losses and scattering properties of the NPs. While scattering is beneficial for photocarrier generation, parasitic absorption in the NPs obviously leads to a drop in the solar cell efficiency. Therefore, the scattering performance, γ_{scatt}, of the nanostructures was evaluated as:

$$\gamma_{scatt} = \frac{T_{Diff} + R_{Diff}}{Abs + T_{Diff} + R_{Diff}} \tag{2.10}$$

Figure 2.13 shows γ_{scatt} as a function of the wavelength for four different Ag thicknesses annealed at 450°C and 500°C. With increasing t_{Ag} from 7.5 nm to 23 nm, the maximum values of γ_{scatt} are almost tripled together with significant spectral broadening. As mentioned previously, we attribute this behavior to the increase in the mean SC size of the nanoparticles with increasing precursor film thickness, as shown in Fig. 2.9. An important quantity of interest is the integrated scattering performance $\mathit{\Gamma}_{scatt}$ over the whole measured wavelength range ($350 - 850$ nm), defined as:

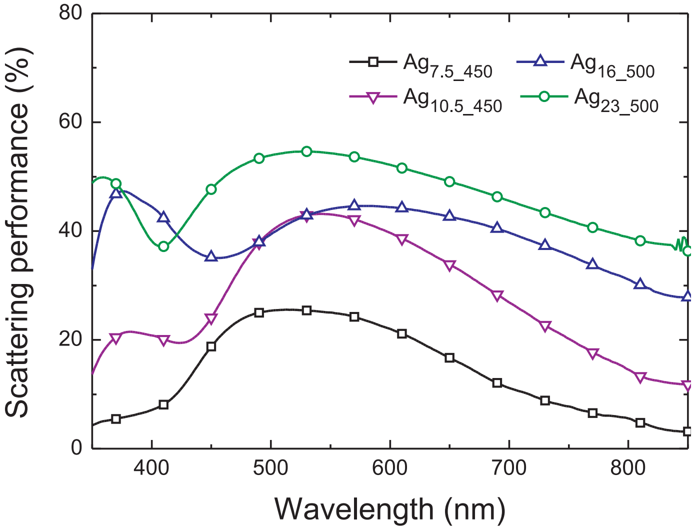

Figure 2.13: Spectra of the scattering performance of Ag NPs formed from precursor film thicknesses of 7.5, 10.5, 16 and 23 nm after annealing at 450°C and 500°C.

$$\Gamma_{scatt} = \frac{\int T_{Diff} + \int R_{Diff}}{\int Abs + \int T_{Diff} + \int R_{Diff}} \tag{2.11}$$

This quantity is plotted in Fig. 2.14 as a function of the mean SC size. We observe a saturation behavior for mean SC size higher than 160 nm. However, the most efficient nanostructure (sample Ag_{23_250}) exhibits a broad size distribution, up to 800 nm.

Γ_{scatt} can be compared with the quantity Γ_Q plotted in the inset of Fig. 2.3(b) and described in section 2.3. Both quantities increase with the particle size, as the bigger is the particle the more dominant is the scattering with respect to absorption. For sizes above 150 nm Γ_{scatt} and Γ_Q start saturating as higher-order modes appear in the Q_{Scatt} spectrum, leading to the smoothening of the resonant character of the particles. However, the computed Γ_Q line in Fig. 2.3(b) lies above the Γ_{scatt} points in Fig. 2.14, mostly due to the unexpectedly high parasitic absorption of the self-assembled NPs

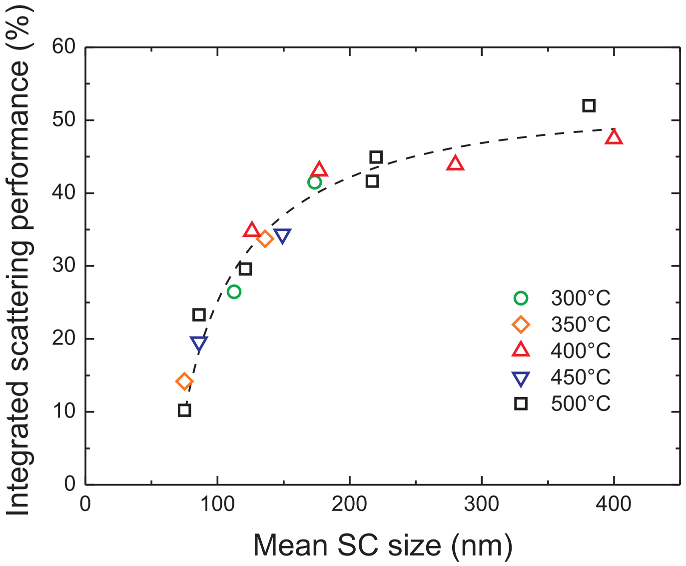

Figure 2.14: Correlation between the integrated scattering performance and the mean surface coverage (SC) size of well-defined Ag NPs (S-type and D-type) fabricated by the SSD process.

According to the results of Fig. 2.11, any of the samples with mean SC sizes above $\sim 200\,\text{nm}$ can exhibit the maximum light scattering over the broad spectral range analyzed $(350-850\,\text{nm})$. Nevertheless, for application in photovoltaics, it is preferable to use the smallest possible particle size in order to reduce the costs of the device, minimize the roughness produced by the NPs in the cell, and minimize the processing temperature. As such, the most advantageous particle sizes lie close to the knee of the $\mathit{\Gamma}_{scatt}$ curve, such as the samples produced with $t_{Ag} = 16\,\text{nm}$ which have mean SC sizes around 200 nm.

2.4.5 Applicability

Parasitic absorption in metallic nanostructures can be a major obstacle for achieving efficient light trapping in thin film solar cells if the benefit coming from light scattering cannot exceed losses in the nanostructures. Thus, it is preferable to incorporate the NPs in the back reflector of the solar cells so that they only interact with the wavelengths that are not fully absorbed in a single pass through the cell. Moreover, the high scattering intensity is desirable at angles away from the normal incidence direction to force the light rays to traverse a longer path inside the cell material.

A typical configuration of such a plasmonic back reflector (PBR) consists of a flat silver mirror and a layer of Transparent Conductive Oxide (TCO) with embedded metallic NPs. The whole structure can be supported on top of a substrate such as glass (shown schematically in the inset of Fig. 2.15). The parameters commonly used to describe the scattering properties of BRs are the total R^{PBR}_{Total} and diffuse reflection R^{PBR}_{Diff}. Total reflection tells how a particular BR is close to the perfect mirror and thus determines the parasitic absorption (losses) with the relation: $Abs^{PBR} = 100\% - R^{PBR}_{Total}$. The most important parameter, however, is the diffused reflection as it describes the amount of light that is scattered away from the incident direction and thus the amount of sunlight which has increased probability of being absorbed due to the longer path in the solar cell material. A first order estimation of the suitability of a specific NP structure for implementation in a PBR can be determined considering that a perfectly flat mirror, with reflectivity of 1, is placed beneath the particles. The R^{PBR}_{Total} and R^{PBR}_{Diff} of such simplified PBR structure are calculated by taking into account multiple reflections between the Ag mirror and the NPs:

$$\begin{aligned}
R^{PBR}_{Total} &= R_{Total} + T^{2}_{Total}\sum_{n=0} R^{n}_{Total} \\
R^{PBR}_{Spec} &= (R_{Total} - R_{Diff}) + (T_{Total} - T_{Diff})^{2}\sum_{n=0}(R_{Total} - R_{Diff})^{n} \\
R^{PBR}_{Diff} &= R^{PBR}_{Total} - R^{PBR}_{Specular} \qquad (2.12)
\end{aligned}$$

where R^{PBR}_{Spec} represents the specular reflectivity and R_{Total}, T_{Total}, R_{Diff} and T_{Diff} are taken from the measurements.

Figure 2.15 shows the reflections obtained from equations 2.12 for NPs with the mean SC size ranging from 86 to 280 nm together with an I-type NPs (sample Ag_{16_250}). The R^{PBR}_{Total} calculated for sample $Ag_{7.5\_450}$ shows a deep minimum at 450 nm corresponding to the *Ext* peak of plasmonic resonance, and close to 100% reflection of a perfectly flat Ag mirror for out-of-resonance wavelengths. At the same time R^{PBR}_{Diff} reaches values of

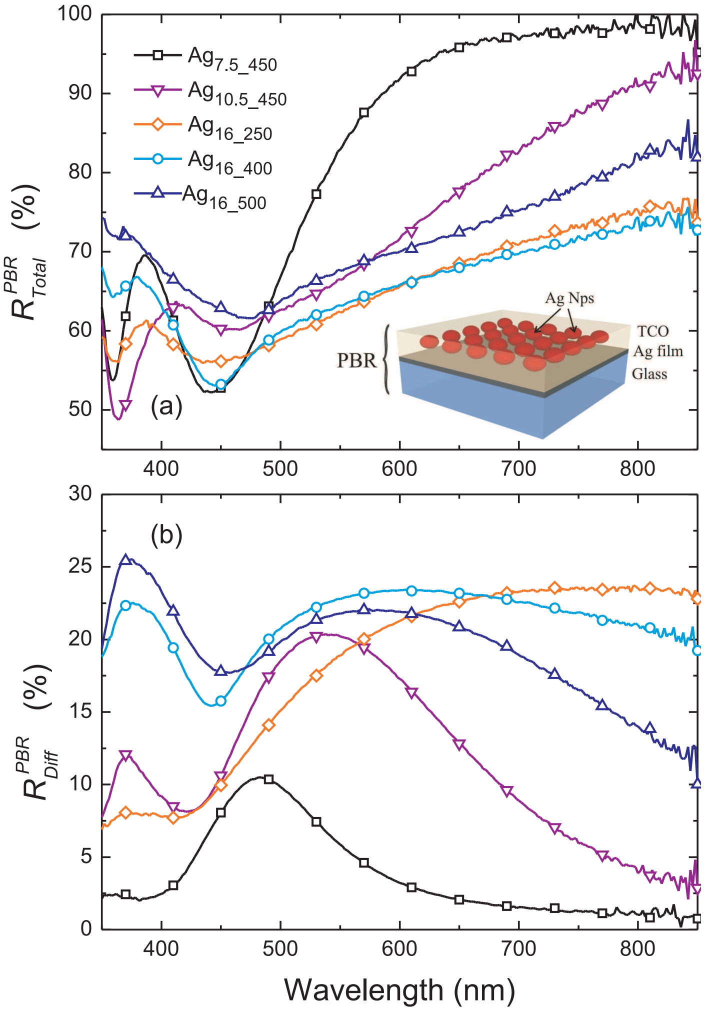

Figure 2.15: Estimated (a) total and (b) diffuse reflection, according to equations 2.12, for samples $Ag_{7.5\_450}$, $Ag_{10.5\_450}$, Ag_{16_250}, Ag_{16_400}, Ag_{16_500} incorporated in an ideal plasmonic back reflector (PBR) shown schematically in the inset.

$\sim 10\%$ peaked at 482 nm. An increase of the mean SC size together with NPs flattening (sample Ag_{16_400}) leads to a considerable increase of light diffusion up to 23.5% together with significant spectral broadening. The I-type NPs, on the other hand, show high values of R_{Diff}^{PBR} only in the NIR range. Although samples Ag_{16_400} and Ag_{16_250} are expected to be suitable for diffuse reflection, they suffer from higher parasitic absorption than samples $\mathrm{Ag}_{10.5\_450}$ and Ag_{16_500}, which results in lower values of R_{Total}^{PBR} in the whole investigated spectral range.

The above analysis shows that the big and flattened particles are more beneficial for scattering of long wavelengths and thus, they are more suitable for application in solar cells. In addition, the small NPs should not significantly affect the performance of the PBR since the related reduction in reflection occurs only for wavelengths that are normally absorbed in the first pass through the cell and do not reach the back reflector.

The simplified PBR structure analyzed in this section allows a qualitative assessment of the reflective properties of the fabricated NP structures for implementation in a real solar cell BR. However, in a real device the particles would be embedded in a TCO medium with refractive index higher than the measured case of NPs on glass, which would red-shift the peaks obtained in Fig. 2.15. In addition, the presence of the absorbing cell material on top of the PBR would also influence its scattering properties. Such effects have not been taken into account in the present analysis, since it is only intended to provide a practical first-order evaluation of the performance of the produced NP structures to assist in the optimization of the fabrication conditions.

2.5 Nanoparticles formed on AZO-coated glass substrate

Aluminium doped zinc oxide (AZO) is an important material commonly used in thin film silicon solar cell technology as a thin contact layer placed between n-type Si and the metallic mirror. This provides a barrier for diffusion of metal atoms into the absorber, an improved band alignment, and a lower parasitic loses in the mirror in comparison to the metal deposited directly on silicon [25]. As discussed in the introduction chapter, the NPs would be preferably located at the rear side of the cell and embedded in the AZO layer between Si and back reflector. An encapsulation of the NPs in

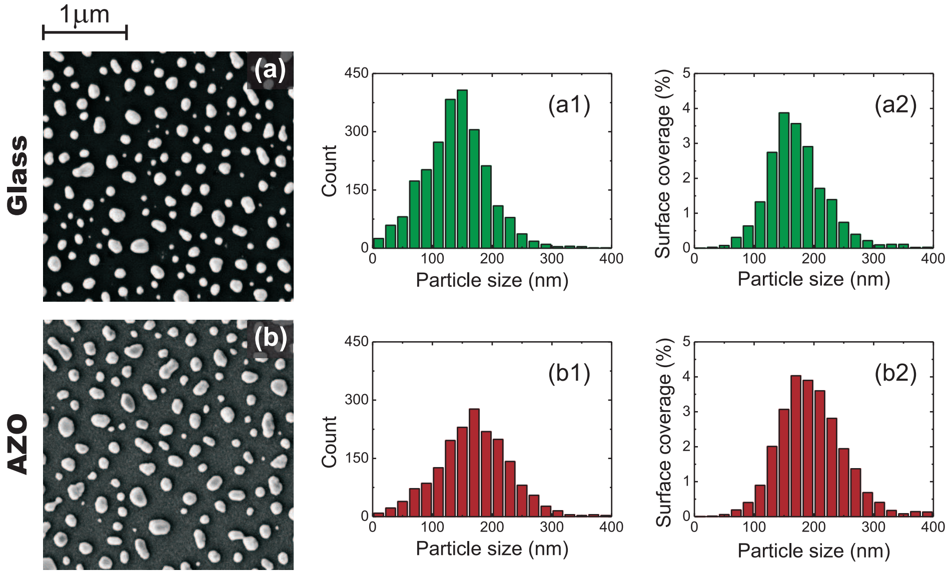

Figure 2.16: SEM images of Ag NPs formed on (a) bare glass and (b) glass coated with 50 nm of AZO after annealing of 12 nm thick precursor film for 1 h at 400°C. The corresponding NPs' size (in-plane diameter) and surface coverage (SC) distributions are shown in (a1, b1) and (a2, b2), respectively.

zinc oxide leads also to their improved stability against the sulfidation occurring in atmospheric air. It is therefore important to study the properties of self-assembled Ag NPs formed on- and embedded in the AZO.

2.5.1 Structural properties

Figure 2.16 depicts the SEM images together with the corresponding size and surface coverage distributions of NPs, formed from 12 nm thick Ag film annealed at 400°C, fabricated in the exact same process on (a) bare glass and (b) glass coated with 50 nm of AZO. Nanoparticles formed on AZO tend to be larger than those formed on glass, though the maximum sizes of NPs are approximately the same in both cases. The average NPs' size and the mean SC size, determined from Gaussian-type peak fitting, increase from 139 ± 2 nm to 169 ± 2 nm and from 164 ± 2 nm to 190 ± 1 nm, respectively. Furthermore, the relative number of small particles as well as the overall number of particles is reduced on AZO. As a result, the SC distribution is better fitted with a lognormal than with gaussian type single-peak curve. In addition, the total surface coverage increases from 20.3% to 26.1%, which reveals that NPs formed on AZO also tend to be more flat than those formed on glass substrate. All the morphological differences described above can be attributed to the higher surface free energy of AZO than glass.

2.5.2 Optical properties

Besides the important morphological changes, formation of the NPs on AZO-coated glass influences also their optical properties due to the increase of the effective refractive index, n_{eff}, of the medium surrounding the NPs. Fig. 2.17 shows the comparison between the extinction (*Ext*) spectra of particles formed in the same process on bare glass, on glass coated with 50 nm thick AZO, and NPs formed on 50 nm thick AZO coated with another 50 nm thick AZO layer - labelled as NPs embedded in AZO. The *Ext* peak was found to red-shift from 555 nm for NPs on glass, to 643 nm for NPs on AZO, and to 733 nm for NPs embedded in AZO. Furthermore, a slight rise of the peak intensity and a significant peak broadening were observed. The differences between the first two cases can originate from both, the increased n_{eff} and the increased mean NPs size. However, the differences between the last two are purely an effect of a higher refractive index. Observed trends stay in qualitative agreement with those predicted by the analytical Mie theory formalism discussed in section 2.3. Both effects of the spectral red-shift and broadening, are advantageous for application in PV due to the better spectral matching of the plasmonic resonance with the wavelengths that are normally poorly absorbed in silicon.

As the contribution of the substrate has not been subtracted from the measurements shown in Fig. 2.17, absorption edges of glass and AZO are clearly observed at 350 nm and 400 nm respectively. Moreover, the out-of-resonance values of *Ext* approach the values of the total reflection of the substrate.

The optical properties of the NPs were measured in two distinct configurations: front-side illumination - when the incident light impinges the NPs first, and rear side illumination when the incident light impinges the glass substrate first. The two configurations correspond to the way in which NPs interact with the sunlight in the substrate and superstrate thin film solar cells, respectively. The *Ext* spectra for front- and rear-side illumination, shown in Fig. 2.17 with solid and dashed lines respectively, were found

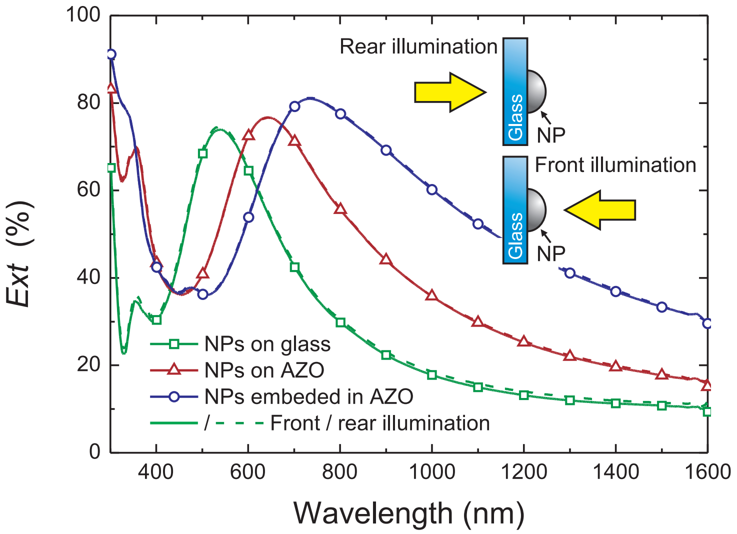

Figure 2.17: Extinction (*Ext*) measurements of NPs formed from 12 nm thick Ag film annealed at 400°C for 1 h in three different configurations: NPs on glass, NPs on 50 nm thick AZO, and NPs embedded in 100 nm thick AZO. Solid lines correspond to the front- and dashed to the rear-side illumination. Contribution of the substrate has not been subtracted from the measurements.

to remain almost identical in the whole investigated spectral range. This reveals that the resonance strength is equal in both cases. Nevertheless, significant differences were observed for the single components of the extinction, depicted in Fig. 2.18 for the three samples described previously. The main drawback of rear side illumination is a clearly lower R_{Total}, which for constant *Ext* leads to a notably higher *Abs*. On the other hand, the T_{Diff} is slightly increased and R_{Diff} is almost doubled while their spectral shape is moderately narrower.

The main effects of the higher refractive index are in agreement with those previously discussed for *Ext*, namely the red-shift and the spectral broadening of the resonance characteristics in both illumination conditions.

The asymmetry between the two illumination configurations should be attributed to the asymmetry of the refractive index around NPs as well as to the hemispherical cross-section shape of the NPs. Apparently, when illumi-

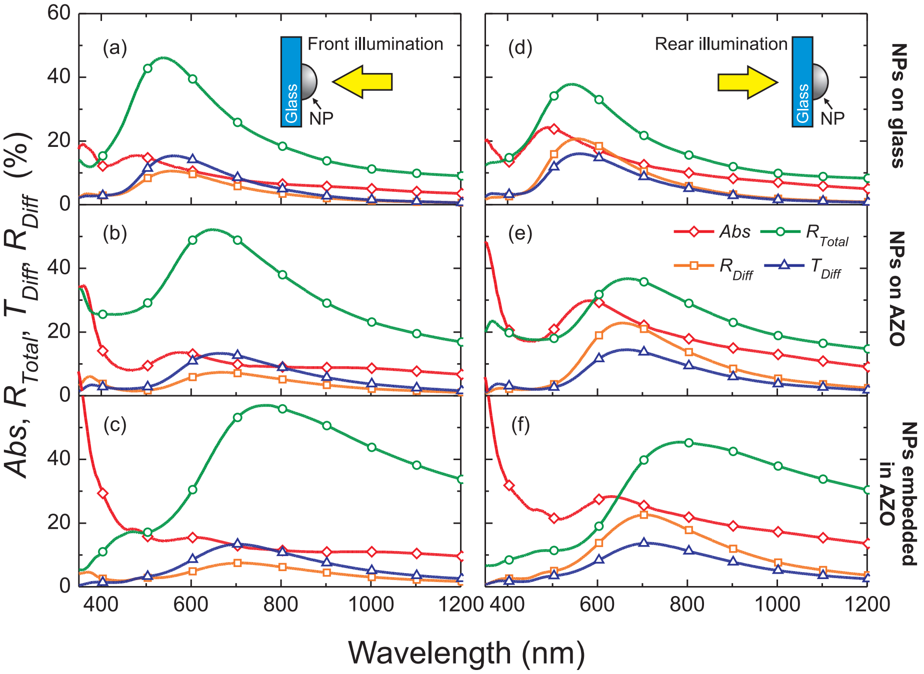

Figure 2.18: Absorption (*Abs*), total reflection (R_{Total}) and diffused parts of transmission (T_{Diff}) and reflection (R_{Diff}) of NPs formed from 12 nm thick Ag film annealed at 400°C for 1 h in three different configurations: NPs on glass (upper row - (a), (d)), NPs on 50 nm thick AZO (middle row - (b), (e)), and NPs embedded in 100 nm thick AZO (bottom row - (d), (f)). Left column corresponds to the front- and right column to the rear-side illumination. Contribution of the substrate has not been subtracted from the measurements.

nated from the rear side the sharp corners of the NPs act more pronouncedly as so called 'hot spots' increasing the resonant interactions, which gives rise to both, absorption and scattering.

The effects described above stay in good agreement with the results of Pennanen and Toppari [26], who investigated the efficiency of light coupling into a planar waveguide due to gold nanodisks, and found that forward scattering is approximately equal regardless the illumination direction while the backscattering is much stronger towards the high refractive index material, which in consequence leads to clearly higher coupling efficiencies for the rear side illumination condition. Those results suggest that, for the measurements performed by the author, at least a fraction of back reflected

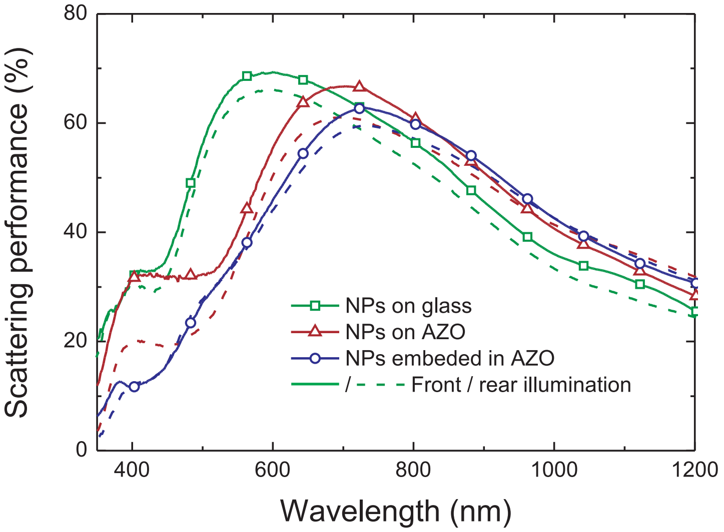

Figure 2.19: Scattering performance (γ_{scatt}), defined with equation 2.10, of NPs formed from 12 nm thick Ag film annealed at 400°C for 1 h in three different configurations: NPs on glass, NPs on 50 nm thick AZO, and NPs embedded in 100 nm thick AZO. Solid lines correspond to the front- and dashed to the rear-side illumination. Contribution of the substrate has not been subtracted from the measurements, and thus, contributes to the γ_{scatt}.

light (R_{Total}) is coupled into the glass substrate and is not collected in the integrating sphere which results in an artificial rise of Abs for the rear side illumination.

Figure 2.19 depicts the scattering performance (γ_{scatt}), defined with equation 2.10, for the three samples being analysed. The maximum of γ_{scatt} curve red-shifts similarly to the Ext peak, however, due to the higher parasitic absorption in the NPs the maximum values are moderately reduced. It should be noted, though, that since the contribution of the substrate has not been subtracted from the measurements, the absorption of the AZO, even if relatively small, slightly lowers the values of γ_{scatt}. Even though the scattering is more pronounced for the rear-side illumination, the cost of higher Abs associated with the gain in scattering results in the systematically higher values of γ_{scatt} in the opposite, front-side illumination condition.

Nonetheless, as discussed above a fraction of high *Abs* might be an artifact related to the configuration of the measurements, and if so, the plasmonic light trapping should be more efficient in the superstrate solar cells.

The maximum values γ_{scatt} for NPs formed on glass substrate presented in this section are of about 25% higher than corresponding values presented in section 2.4.2 (Fig. 2.13) for similar NPs' sizes. This improvement is attributed to the better crystalline quality of the precursor films originated from the deposition with higher power and lower working pressure with respect to the previous samples (section 2.2). This is expected to result in improved quality of the NPs material, which leads to less dissipative interactions at the plasmonic resonances and thus lower parasitic absorption [9, 21].

2.6 Conclusions

In this chapter, a systematic study of the structural and optical properties of self-assembled silver nanostructures according to the fabrication parameters of solid-state dewetting process is presented and discussed.

Four distinct types of morphology, obtained in specific ranges of fabrication conditions, are defined and summarized quantitatively through a structural-phase diagram of nanostructure formation. It was verified that the main quantity for the correlation between the statistical parameters and the optical properties of the nanostructures is the surface coverage size distribution. It is also concluded that the small (size $< 60\,\text{nm}$) particles are not responsible for the optical response of the nanostructures for wavelengths above 600 nm, and thus should not significantly affect the performance of such structures when incorporated in thin film solar cells.

According to electromagnetic calculations, the Ag NPs that allow the best far-field scattering performance are those with sizes above 100 nm, since only with such big sizes the light radiated through scattering can considerably exceed the light absorbed in the NPs material. However, our experiments evidence that even the NPs fabricated with such big sizes suffer from high parasitic absorption, which can be a drawback for the implementations of this approach in thin film phovoltaics. The origin of this unexpectedly high absorption can be attributed to the polycrystalline structure of the NPs, which leads to an increase in the energy dissipated inside the NP material at their plasmonic resonance. Nonetheless, despite such high dissipation, the scattering efficiency of the fabricated nanostructures is demonstrated to increase with mean surface coverage size and saturate for sizes above 160 nm, in accordance to what is expected from Mie theory results. Particles with sizes in this saturation regime are experimentally shown to provide considerable diffuse reflection for a broad range of wavelengths in the visible and near-infrared, which motivates the further development of the present approach towards its application in solar cell fabricated on plasmonic back reflectors.

Particles formed on AZO tend to be bigger and flatter than those formed on glass, and have broad resonance in the NIR range which makes them more suitable for application in PV. The experiment revealed also that scattering is more pronounced in the rear illumination condition whereas, due to the cost of the higher parasitic absorption, the scattering performance is higher in the opposite front-side illumination.

References

[1] C. V. Thompson, “Solid-state dewetting of thin films,” *Annual Review of Materials Research*, vol. 42, no. 1, pp. 399–434, 2012.

[2] D. Srolovitz and M. Goldiner, “The thermodynamics and kinetics of film agglomeration,” *JOM*, vol. 47, no. 3, pp. 31–36, 1995.

[3] M. Ohring, “Chapter 9 - Film structure,” in *Materials Science of Thin Films (Second Edition)*, second edition ed., M. Ohring, Ed. San Diego: Academic Press, 2002, pp. 495 – 558.

[4] D. Gentili, G. Foschi, F. Valle, M. Cavallini, and F. Biscarini, “Applications of dewetting in micro and nanotechnology,” *Chem. Soc. Rev.*, vol. 41, pp. 4430–4443, 2012.

[5] “Recent trends on nanocomposites based on cu, ag and au clusters: A closer look,” *Coordination Chemistry Reviews*, vol. 250, no. 1112, pp. 1294 – 1314, 2006.

[6] M. Chhowalla, K. B. K. Teo, C. Ducati, N. L. Rupesinghe, G. A. J. Amaratunga, A. C. Ferrari, D. Roy, J. Robertson, and W. I. Milne, “Growth process conditions of vertically aligned carbon nanotubes using plasma enhanced chemical vapor deposition,” *Journal of Applied Physics*, vol. 90, no. 10, pp. 5308–5317, 2001.

[7] V. Schmidt, J. V. Wittemann, S. Senz, and U. Gsele, "Silicon nanowires: A review on aspects of their growth and their electrical properties," *Advanced Materials*, vol. 21, no. 25-26, pp. 2681–2702, 2009.

[8] "Porous model type electrodes by induced dewetting of thin Pt films on YSZ substrates," *Solid State Ionics*, vol. 181, no. 12, pp. 7 – 15, 2010.

[9] S. Morawiec, M. J. Mendes, S. Mirabella, F. Simone, F. Priolo, and I. Crupi, "Self-assembled silver nanoparticles for plasmon-enhanced solar cell back reflectors: correlation between structural and optical properties," *Nanotechnology*, vol. 24, no. 26, p. 265601, 2013.

[10] N. C. Lindquist, P. Nagpal, K. M. McPeak, D. J. Norris, and S.-H. Oh, "Engineering metallic nanostructures for plasmonics and nanophotonics," *Reports on Progress in Physics*, vol. 75, no. 3, p. 036501, 2012.

[11] P. West, S. Ishii, G. Naik, N. Emani, V. Shalaev, and A. Boltasseva, "Searching for better plasmonic materials," *Laser & Photonics Reviews*, vol. 4, no. 6, pp. 795–808, 2010.

[12] M. Ohring, "Chapter 4 - Discharges, plasmas, and ion-surface interactions," in *Materials Science of Thin Films (Second Edition)*, second edition ed., M. Ohring, Ed. San Diego: Academic Press, 2002, pp. 145 – 202.

[13] M. Schmid, R. Klenk, M. C. Lux-Steiner, M. Topi, and J. Kr, "Modeling plasmonic scattering combined with thin-film optics," *Nanotechnology*, vol. 22, no. 2, p. 025204, 2011.

[14] C. F. Bohren and D. R. Huffman, *Absorption and Scattering of Light by Small Particles.* Wiley-VCH Verlag GmbH, 2007.

[15] V. D. Miljković, T. Shegai, P. Johansson, and M. Käll, "Simulating light scattering from supported plasmonic nanowires," *Optics Express*, vol. 20, no. 10, pp. 10 816–10 826, 2012.

[16] H. Sun, M. Yu, G. Wang, X. Sun, and J. Lian, "Temperature-dependent morphology evolution and surface plasmon absorption of ultrathin gold

island films," *The Journal of Physical Chemistry C*, vol. 116, no. 16, pp. 9000–9008, 2012.

[17] H. C. Kim, T. L. Alford, and D. R. Allee, "Thickness dependence on the thermal stability of silver thin films," *Applied Physics Letters*, vol. 81, no. 22, pp. 4287–4289, 2002.

[18] Y. Kojima and T. Kato, "Nanoparticle formation in Au thin films by electron-beam-induced dewetting," *Nanotechnology*, vol. 19, no. 25, p. 255605, 2008.

[19] J. L. Elechiguerra, L. Larios-Lopez, C. Liu, D. Garcia-Gutierrez, A. Camacho-Bragado, and M. J. Yacaman, "Corrosion at the nanoscale: the case of silver nanowires and nanoparticles," *Chemistry of Materials*, vol. 17, no. 24, pp. 6042–6052, 2005.

[20] M. Mcmahon, R. Lopez, I. Meyer, H.M., L. Feldman, and J. Haglund, R.F., "Rapid tarnishing of silver nanoparticles in ambient laboratory air," *Applied Physics B*, vol. 80, no. 7, pp. 915–921, 2005.

[21] C. Pahud, O. Isabella, A. Naqavi, F.-J. Haug, M. Zeman, H. P. Herzig, and C. Ballif, "Plasmonic silicon solar cells: impact of material quality and geometry," *Optics Express*, vol. 21, no. S5, pp. A786–A797, 2013.

[22] H. Ditlbacher, A. Hohenau, D. Wagner, U. Kreibig, M. Rogers, F. Hofer, F. R. Aussenegg, and J. R. Krenn, "Silver nanowires as surface plasmon resonators," *Physical Review Letters*, vol. 95, p. 257403, 2005.

[23] D. D. Evanoff and G. Chumanov, "Size-controlled synthesis of nanoparticles. 1. silver-only aqueous suspensions via hydrogen reduction," *The Journal of Physical Chemistry B*, vol. 108, no. 37, pp. 13 948–13 956, 2004.

[24] ——, "Size-controlled synthesis of nanoparticles. 2. measurement of extinction, scattering, and absorption cross sections," *The Journal of Physical Chemistry B*, vol. 108, no. 37, pp. 13 957–13 962, 2004.

[25] U. Palanchoke, V. Jovanov, H. Kurz, P. Obermeyer, H. Stiebig, and D. Knipp, "Plasmonic effects in amorphous silicon thin film solar cells

with metal back contacts," *Optics Express*, vol. 20, no. 6, pp. 6340–6347, 2012.

[26] A. M. Pennanen and J. J. Toppari, "Direct optical measurement of light coupling into planar waveguide by plasmonic nanoparticles," *Optics Express*, vol. 21, no. S1, pp. A23–A35, 2013.

Chapter 3

Absorption enhancement in silicon films via plasmonic scattering

In this chapter, an absorption enhancement in thin silicon films due to the plasmonic scattering is presented. The self-assembled silver nanoparticles (NPs) are incorporated on the rear side of the films, however, in two distinct arrangements corresponding to superstrate and substrate configuration solar cells.

The structural properties of NPs formed on a-Si film by solid-state dewetting, with various precursor film thicknesses and AZO spacer layers, are investigated and correlated with the absorption enhancement in silicon film. The coupling efficiency has been found to increase with NPs' average size and saturate above $180\,\mathrm{nm}$*, to decrease with increasing thickness of the spacer between silicon and NPs and to saturate above* $50\,\mathrm{nm}$*, and to be significantly smaller for spherical than for hemispherical NPs, which stay in qualitative agreement with theoretical predictions.*

A novel procedure, involving a combination of phothermal deflection spectroscopy and fourier transform photocurrent spectroscopy, employed in this work allowed for the quantification of useful and parasitic absorption in $0.9\,\mu\mathrm{m}$ *thick* μ*c-Si:H deposited on a plasmonic back reflector. It is demonstrated that the optical losses in the NPs are insignificant in the* $500-730\,\mathrm{nm}$ *wavelength range, beyond which they increase rapidly with increasing illumination wavelength. Furthermore, a broadband enhancement of* 89.9% *of useful absorption has been achieved and attributed to both the random front surface texture, originated from the conformal growth of Si on top of the NPs, and to the scattering of light by the plasmonic NPs.*

3.1 Nanoparticles in superstrate configuration

3.1.1 Sample preparation

The $230 \pm 10\,\mathrm{nm}$ thick hydrogenated amorphous silicon (a-Si:H) films were deposited on glass substrates using plasma-enhanced chemical vapour deposition (PECVD) system. Self-assembled silver nanoparticles (NPs) formed by solid-state dewetting (SSD) process were incorporated directly on the a-Si, or with an aluminium doped zinc oxide (AZO) spacer layer. The deposition of Ag and AZO films was done with RF magnetron sputtering at a working pressure of $2.5 \times 10^{-3}\,\mathrm{mbar}$ in Ar atmosphere with RF power density of 1 and $2.16\,\mathrm{W/cm^2}$, respectively. A procedure allowing for high uniformity and high precision of Ag thickness (t_{Ag}) among respective samples was employed. The post-deposition annealing, in which NPs are formed by the SSD from the thin Ag layer, was done at 450°C in the flow of nitrogen (1 lpm) for 1 h.

Thicknesses of Ag and AZO layers were determined using Rutherford Backscattering Spectrometry (RBS, 2.0 MeV He^+ beam) assuming the Ag density of $5.85 \times 10^{22}\,\mathrm{Ag/cm^3}$ and Zn density in AZO of $3.22 \times 10^{22}\,\mathrm{Ag/cm^3}$. The relative error of the thickness measurements was estimated at the level of 3%. The structural properties of the NPs were investigated by Scanning Electron Microscopy (SEM) through a field emission Zeiss Supra 25 system. The statistical parameters of NPs were derived from digital analysis of SEM images using the ImageJ software [1].

The optical functions of Si films were determined with ellipsometry before and after the annealing step, which resulted in desirable reduction of the bandgap, hence the red-shift of the absorption edge, as shown if Fig. 3.1. The change of optical properties originate the out-diffusion of hydrogen and partial recrystallization of the amorphous material [2]. This material is further referred to as amorphous silicon, a-Si.

In order to investigate the effect of distinct NP's, the same a-Si material has also been used as a substrate for the deposition of self-assembled arrays of colloidal gold NPs, using the wet-coating technique described by Mendes et. al [3]. Such colloidal NPs are characterized by the spherical shape and high monodispersion of size.

The optical properties were measured using a double beam UV-Vis-NIR spectrophotometer equipped with a 4-inch integrating sphere allowing to collect diffused light together or apart from the specular part, in both

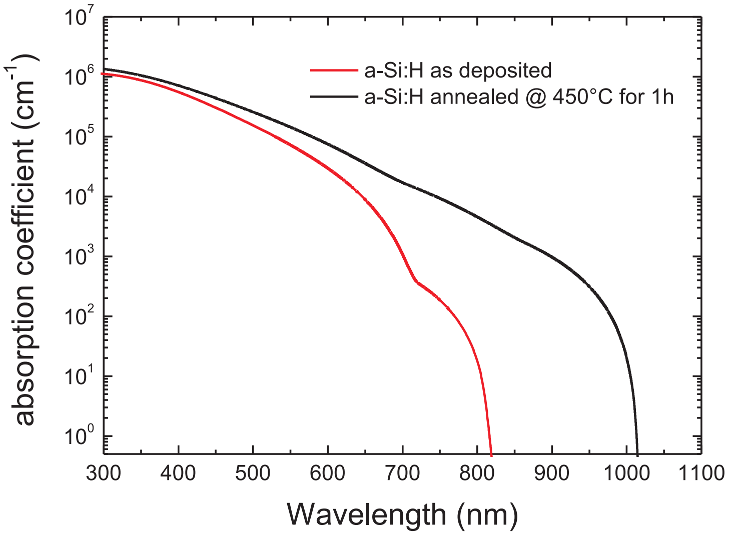

Figure 3.1: Absorption coefficient of as deposited a-Si:H film and annealed at 450°C for 1 h determined from the dielectric functions measured with ellipsometry.

reflection and transmission mode. The absorption (Abs) in the a-Si films was calculated as:

$$Abs = 100\% - T_{Total} - R_{Total} \tag{3.1}$$

where T_{Total} and R_{Total} are measured total transmission and total reflection, respectively

For simplicity we shall refer to samples with NPs using the abbreviated notation X_{y_z}, where ”X” is used to describe the substrate, ”y” is the value of the precursor film thickness in nanometers and ”z” the annealing temperature.

3.1.2 Nanoparticles fabricated by SSD

Effect of precursor film thickness

Figure 3.2 depicts the SEM images of Ag NPs formed on bare 230 nm thick a-Si film after annealing of 9.6, 12.8 and 17.0 nm thick precursor film for 1 h at 450°C together with the corresponding NPs' size (in-plane diameter)

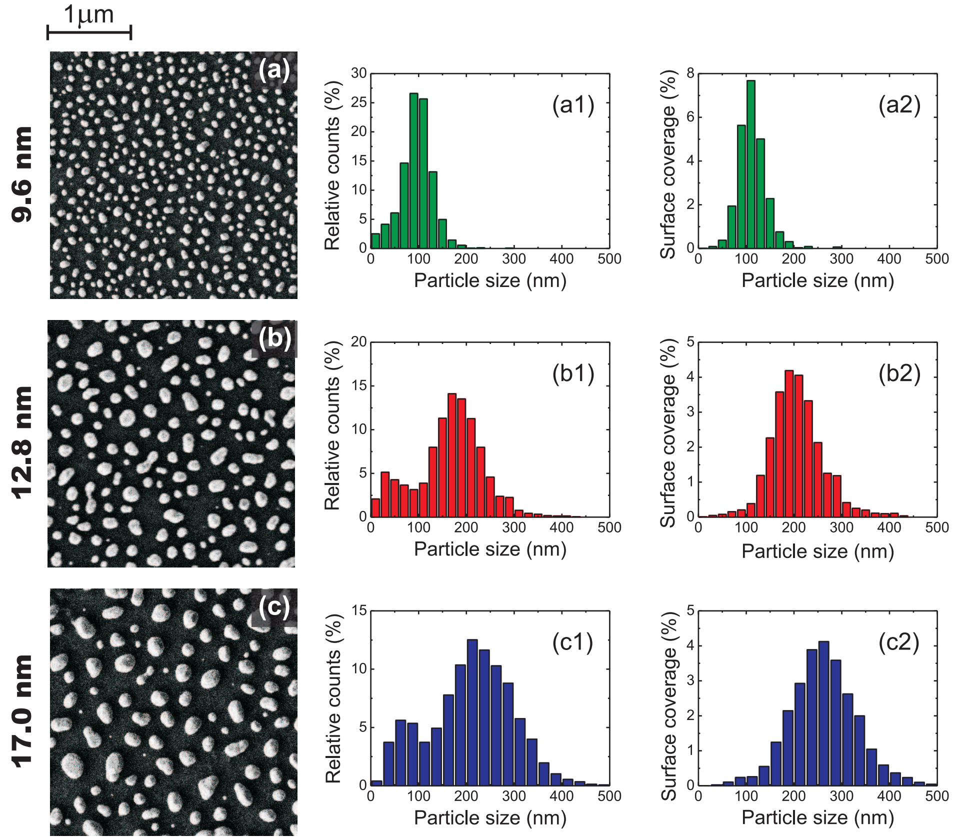

Figure 3.2: SEM images of Ag NPs formed on bare 230 nm thick a-Si film after annealing of (a) 9.6 nm, (b) 12.8 nm and (c) 17.0 nm thick precursor film at 450°C for 1 h. The corresponding NPs' size (in-plane diameter) and surface coverage (SC) distributions are shown in (a1, b1, c1) and (a2, b2, c2), respectively.

Table 3.1: Statistical parameters of NPs formed on bare 230 nm thick a-Si film after annealing of 9.6, 12.8, and 17.0 nm thick (t_{Ag}) precursor film for 1 h at 450°C. The parameters were determined from Gaussian peak fittings to size and surface coverage distributions shown in Fig. 3.2.

t_{Ag}	Average size		Surface coverage		
	small NPs	big NPs	Mean size	FWHM	Total
nm	nm		nm		%
9.6	-	98 ± 1	109.5 ± 0.6	58	24.3
12.8	41 ± 3	180 ± 1	200 ± 1	104	25.3
17.0	64 ± 2	229 ± 1	260 ± 1	146	26.1

and surface coverage (SC) distributions. The statistical parameters of NPs, determined from a Gaussian single- or double-peak fitting to the size and surface coverage distributions are summarized in Table 3.1. The smallest NPs investigated in the experiment were formed from 9.6 nm thick Ag film with an average size of 98 ± 1 nm, which is approximately the lowest limit of the NPs' size range suitable for applications in PV (see section 2.3). A notable uniformity of the nanostructure is confirmed by the narrow distributions of NPs' sizes and SC. Once the thickness of precursor film is increased, the NPs become bigger and the distribution of sizes broadens significantly. The average sizes obtained from 12.8 and 17.0 nm thick Ag film were 180 ± 1 and 229 ± 1 nm, respectively. In addition, a fraction of small NPs appears in the structure originating a second peak in the NPs' size histogram (Figs. 3.2(b1) and 3.2(c1)). The peak vanishes, however, in the SC histograms (Figs. 3.2(b2) and 3.2(c2)), which indicates that the optical properties of the nanostructures should be dominated by the big NPs. The total SC changes only slightly from 24.3% for sample a-Si$_{9.6\_450}$ to 26.1% for sample a-Si$_{17.0\_450}$.

The evolution NPs' in-plane shape is illustrated in Fig.3.3 by the histograms of an aspect ratio (AR) of ellipses fitted to the NPs' shape. In case of sample a-Si$_{9.6\_450}$ the NPs are slightly elongated with the average AR of 1.2. With increasing t_{Ag} the NPs become more elongated which exhibits in the broadening of the AR distribution and the increase of mean value of AR.

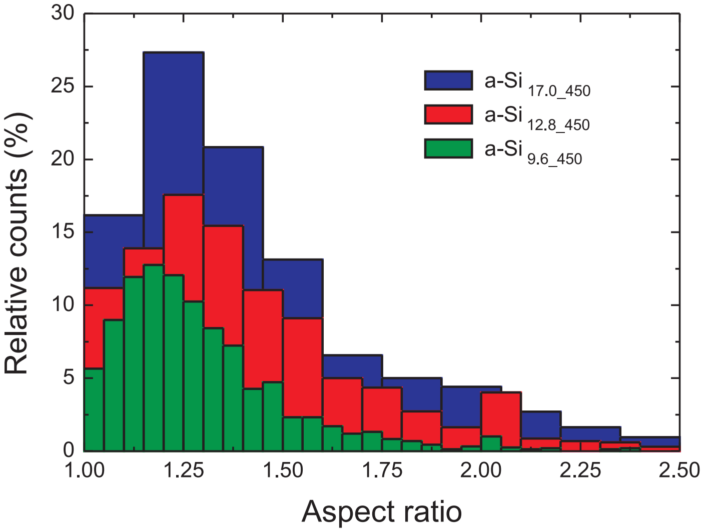

Figure 3.3: Aspect ratio (AR) histograms of NPs formed on bare 230 nm thick a-Si film after annealing of 9.6, 12.8, and 17.0 nm thick precursor film for 1 h at 450°C.

The absorption spectra of samples a-$\mathrm{Si}_{9.6\_450}$, a-$\mathrm{Si}_{12.8\_450}$ and a-$\mathrm{Si}_{17.0\_450}$ in comparison with the reference bare 230 nm thick a-Si film are depicted in Fig. 3.4. The measurements were performed in the rear-side illumination configuration shown schematically in the inset. The incorporation of Ag NPs results in significant increase of Abs, especially in the NIR part of the spectrum corresponding to the light trapping window of the a-Si material investigated here. The big NPs of samples a-$\mathrm{Si}_{12.8\_450}$ and a-$\mathrm{Si}_{17.0\_450}$ were found to provide notably higher improvements than the small ones of samples a-$\mathrm{Si}_{9.6\_450}$. The total Abs enhancements are 35.8%, 59.68% and 62.5% for NPs formed from 9.6 nm, 12.8 nm and 17.0 nm thick Ag film, respectively. The Abs in blue-green spectral region has the same values for all samples as these wavelengths are strongly absorbed in the volume of silicon already in the first pass through the material and as such, the incident light does not interact with the NPs.

The distinct peaks observed in Abs spectra at around 560 nm and 680 nm originate from thin film (Fabry-Perot) interference [4]. The presence of NPs

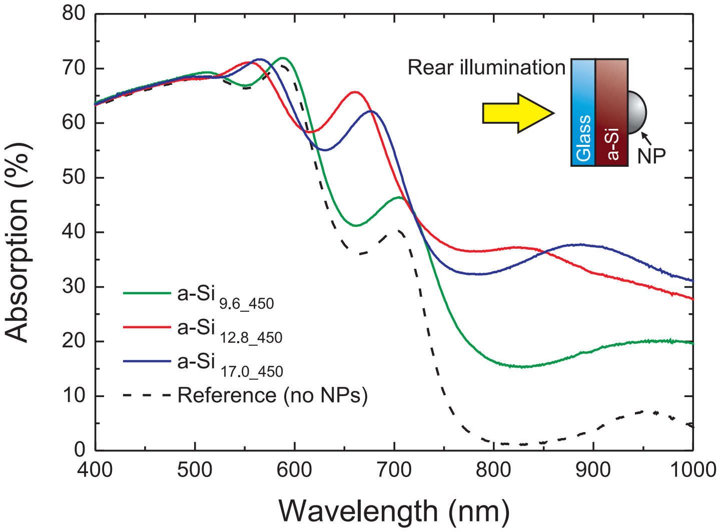

Figure 3.4: Absorption spectra of a 230 nm thick a-Si covered with Ag NPs formed from 9.6, 12.8 and 17.0 nm thick precursor film annealed at 450°C for 1 h. The inset illustrates schematically the investigated structure and the illumination direction.

should not pronouncedly affect the interference pattern as the interaction between the incident light and NPs results either in incoherent scattering, or in parasitic absorption in the NPs. However, the resonant nature of plasmonic interactions result in resonant enhancements of Abs, which consequently may slightly affect the position of interference peaks. In addition, the coherent reflection at a-Si/Ag interface can still occur and give rise to the specular reflection, with respect to bare film, influencing mostly the peak intensity. Nonetheless, the shifts observed in the measurements are chiefly attributed to the variations in a-Si film thickness estimated at ±10 nm by the fitting of experimental spectra with Abs calculated using transfer matrix formalism.

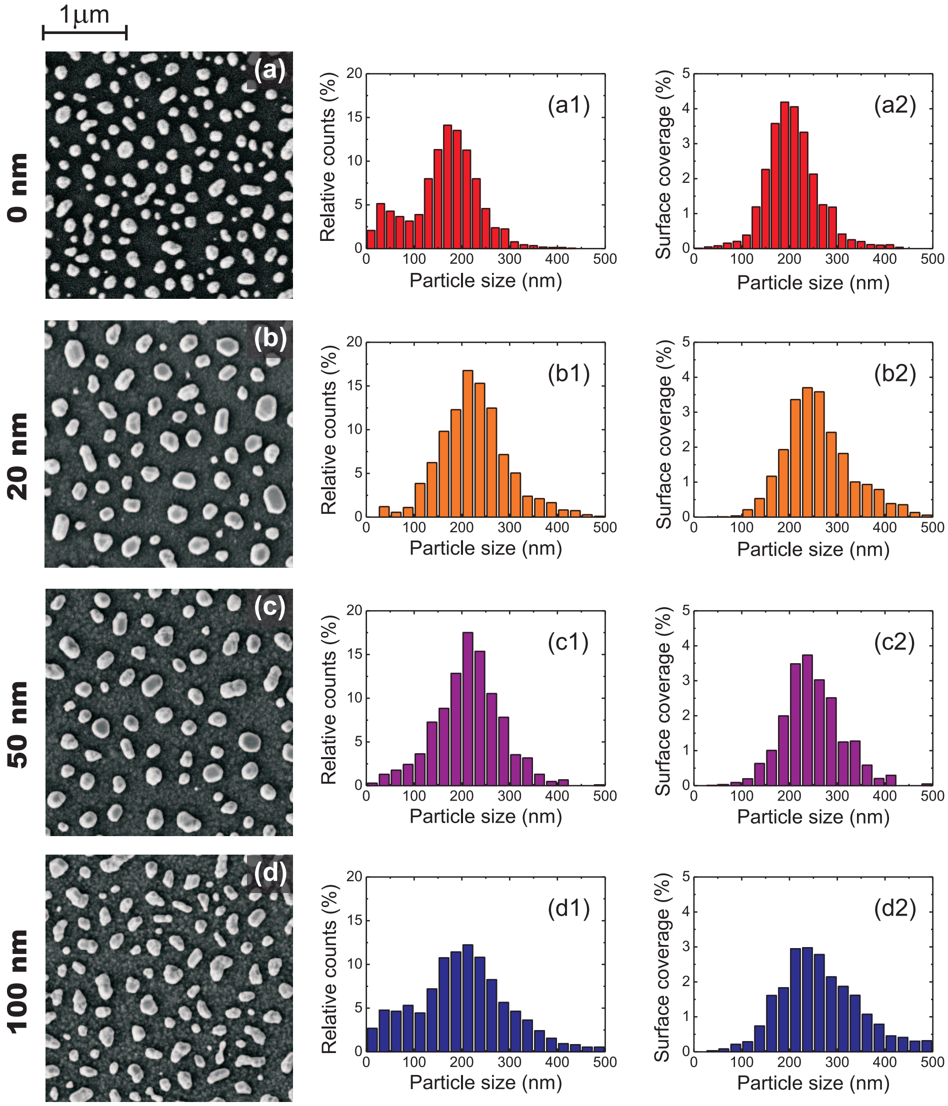

Figure 3.5: SEM images of Ag NPs formed on (a) bare a-Si film and on a-Si film covered with (b) 20, (c) 50, and (d) 100 nm thick AZO spacer layer after annealing of 12.8 nm thick Ag precursor film at 450°C for 1 h. The corresponding NPs' size (in-plane diameter) and surface coverage (SC) distributions are shown in (a1, b1, c1, d1) and (a2, b2, c2, d2), respectively.

Table 3.2: Statistical parameters of NPs formed on 230 nm thick a-Si film covered with 20, 50, and 100 nm thick AZO spacer layer after annealing of 12.8 nm thick precursor film for 1 h at 450°C. The parameters were determined from Gaussian peak fittings to size and surface coverage distributions shown in Fig. 3.5.

t_{AZO}	Average size		Surface coverage		
	small NPs	big NPs	Mean size	FWHM	Total
nm	nm		nm		%
0	41 ± 3	180 ± 1	200 ± 1	104	25.3
20	-	220 ± 2	246 ± 1	129	22.6
50	-	217 ± 2	242 ± 1	126	20.4
100	44 ± 6	207 ± 3	250 ± 1	172	23.0

Effect of AZO spacer layer

Figure 3.5 depicts the morphological changes of NPs fabricated on bare a-Si film and on a-Si film covered with 20, 50, and 100 nm thick AZO spacer layer. The corresponding statistical parameters describing the nanostructures are listed in table 3.2. In comparison with the NPs formed on uncovered a-Si substrate, the underlying AZO layer results in a formation of considerably larger NPs without any significant fraction of small NPs. This can be attributed to the higher surface energy of AZO as well as higher surface diffusion of Ag atoms on AZO. The average size of he NPs formed on 20 and 50 nm thick AZO layer remain almost unchanged at around 220 nm. Formation of NPs on thicker AZO spacer of 100 nm results in notably less uniform nanostructure, in terms of both shape and size distributions, however still with similar average sizes. For the discussion of the optical properties it is important to notice that the sizes of NPs formed from 12.8 nm precursor film on AZO and from 17 nm film on bare a-Si are approximately the same.

The dependence of absorption spectra on the thickness of AZO spacer layer for NPs formed from 12.8 nm thick precursor film annealed at 450°C for 1 h is shown in Fig. 3.6. The inset illustrates schematically the sample structure and the rear-side illumination configuration used for measurements. The incorporation of AZO results in notable decrease of *Abs* in the NIR part of the spectrum, relative to the case of NPs placed directly on a-Si,

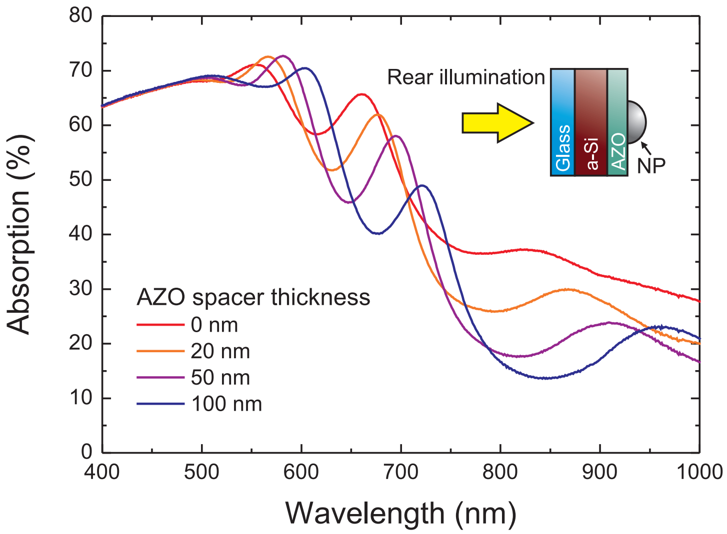

Figure 3.6: Absorption spectra of a 230 nm thick a-Si covered with AZO film with thickness ranging from 0 to 100 nm and Ag NPs formed from 12.8 nm thick precursor film annealed at 450°C for 1 h. The inset illustrates schematically the investigated structure and the illumination direction.

despite the fact that NPs formed on AZO are considerable bigger. Furthermore, the absorption decreases rapidly with increasing distance between silicon and NPs and saturates above 50 nm. The total *Abs* enhancement was found to decrease from 44.6 to 34.8% with the AZO thickness increased from 20 to 100 nm. Finally, the increase of AZO thickness results in the red-shift of the interference fringes, which also proves that a coherent reflection at AZO/Ag interface occurs and it is enhanced in comparison with AZO/air.

3.1.3 Colloidal nanoparticles

In order to study the absorption enhancement provided by distinct NP's cross-section shape, the self-assembled arrays of colloidal gold NPs were deposited on the same a-Si material using the wet-coating technique [3]. The chemically synthesized colloidal NPs are characterized by the spheri-

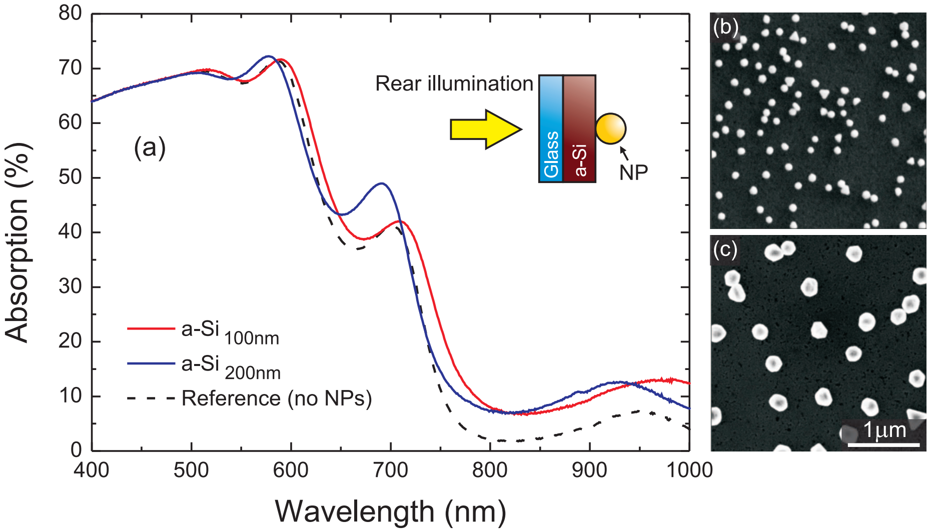

Figure 3.7: (a) Absorption spectra of a 230 nm thick a-Si with 100 and 200 nm diameter colloidal Au NPs. Corresponding NPs' morphology is shown in the SEM images (b) and (c), respectively. The inset illustrates schematically the investigated structure and the illumination direction.

cal shape and high mono-dispersion of their physical properties, which is advantageous to minimize the inhomogeneous broadening of the collective response in functional materials and allows for a precise matching between measured and simulated optical properties.

The absorption spectra of a 230 nm thick a-Si with 100 and 200 nm diameter Au NPs is shown in Fig. 3.7(a). The corresponding spatial distribution of NPs, as well as high mono-dispersion of NPs' shapes and sizes, is shown in Figs. 3.7(b) and Fig. 3.7(c) for 100 and 200 nm diameter NPs, respectively. The total surface coverage of 8% was obtained for both NP sizes with two subsequent depositions. Unexpectedly, the *Abs* spectra were found to vary only slightly with the NPs' size, providing the total absorption enhancements of 13.5% and 10.9% for 100 and 200 nm diameter, respectively. According to the Mie calculations the 100 nm Au NPs placed on the a-Si/Air interface, described by the effective medium model, have a broad spectral resonance centered at 860 nm. The much broader response of 200 nm NPs results in only minor dependence of the scattering efficiency on the illumination wavelength in the range of interest and about 20% lower absolute values in comparison with 100 nm NPs.

3.1.4 Discussion

The particles were fabricated on the rear side of the a-Si film and the Abs spectra were measured in the rear illumination configuration so that the NPs interact with incident light in the same way as they were incorporated in thin-film superstrate solar cells. Such configuration is advantageous as: (i) NPs interact only with light that has not been fully absorbed in the first pass through a-Si, basically wavelengths above 550 nm, which due to the spectral separation of scattering and absorption peaks minimizes the parasitic losses in the short wavelength range; (ii) the intensity of back-scattered light is much higher in the rear-side illumination condition (see section 2.5 and [5]). Furthermore, the particles can in principle provide efficient light trapping in flat silicon film without the need for the texturing, therefore, resulting in no deterioration of the electrical performance of material due to the creation of defects and increased surface recombination.

Coupling efficiency

An important parameter for the application of plasmonic NPs in PV is the efficiency of light coupling into a thin layer of high refractive index semiconductor. It describes the fraction of photons scattered into the substrate at angles large enough to trap them inside the silicon as guided modes, therefore, allowing for an effective absorption [6, 7]. The light scattered at angles smaller than the critical angle for total internal reflection, in any of the multiple scattering events, can escape from the Si slab and be measured as diffuse reflection (R_{Diff}). Since the interaction of light with NP results either in incoherent scattering or absorption, the R_{Diff} is not affected by the inference with incident light, thus, providing an insight into the optical response of the NPs. The comparison between Abs and R_{Diff} for NPs formed from 17.0 nm thick Ag film on bare a-Si and from 12.8 nm thick film on a-Si covered with 20 nm thick AZO is plotted in Fig. 3.8. Importantly, the two samples contain NPs with approximately the same average size and as such, the main difference between them is the AZO spacer layer. The measurement of R_{Diff} allows for rough estimation of the plasmonic resonance

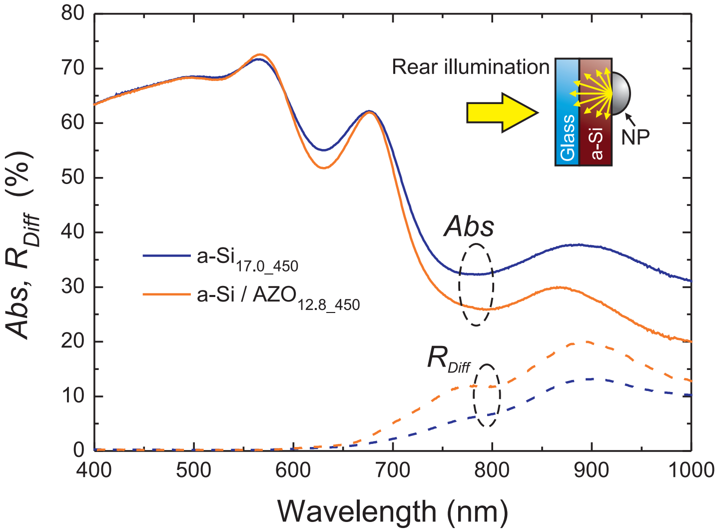

Figure 3.8: Absorption (Abs) and diffused reflection (R_{Diff}) spectra of a 230 nm thick a-Si with Ag NPs formed from 17.0 nm thick precursor directly on silicon (a-Si$_{17.0\_450}$) and from 12.8 nm thick precursor on 20 nm thick AZO spacer (a-Si/AZO$_{12.8\_450}$) layer after annealing at 450°C for 1 h. The inset illustrates schematically the illumination condition.

position at around 900 nm. Since the peak in R_{Diff} corresponds to the peak in Abs, the latter one can be attributed to the plasmonic resonance rather than to the thin film interference.

The increased distance between silicon and NPs results in reduction of the total absorption and in the increase of the amount of diffused light which is not absorbed in the silicon, despite the fact that has been scattered by the NPs. Furthermore, the difference in R_{Diff} between the two samples is exactly equal their difference in Abs in the $680 - 860$ nm wavelength range. These two observations reveal that: (i) the decrease of the coupling efficiency originates from the narrowing of the angular distribution of scattered light with increased distance from high refractive index material; and (ii) in the medium-absorbance regime the scattered light is efficiently absorbed in the volume of a-Si, and that the parasitic losses start to become more pronounced above 900 nm.

Although the absolute coupling efficiency, in terms of absorption enhancement, cannot be measured directly because of the inseparable parasitic losses, the relative changes of total absorption give valuable insight into the dependence of the coupling on several parameters investigated in this work: the AZO spacer layer thickness, the NPs' average size, and the NPs' cross-section shape. The comparison of Abs enhancement, integrated in the $400 - 1000$ nm wavelength range over bare a-Si film, provided by different samples is summarized in Fig. 3.9. For NPs placed directly on silicon, the absorption enhancement has been found to increase significantly with the average size increased from 98 to 180 nm and to saturate with a further increase of the size up to 229 nm. Furthermore, the coupling efficiency has been found to decrease significantly with increasing thickness of AZO spacer layer and saturate to above 50 nm. This reveals that, since the coupling efficiency depends on the overlap between the particle near field and the high refractive index material [6], with the distance above 50 nm the NPs do not experience the presence of silicon and their optical response become similar to the case of NPs deposited on AZO. The observed trends stay in qualitative agreement with the computational results of Beck et. al. [6].

Comparison between SSD and colloidal NPs provide an experimental evidence of the discrepancy in coupling efficiency achievable with spherical and hemispherical NPs, confirming the theoretical predictions of Catchpole et. al. [8], which show that the maximum path length enhancement is about three times lower for 100 nm sphere that the hemisphere with the same diameter, and drops further with increasing sphere diameter.

Useful vs. parasitic absorption

The absorption of incident long-wavelength photons can originate either in the a-Si, resulting from the longer optical path-length of light scattered by the NPs, or in the NPs themselves. Thus, a valid question is whether the enhancement observed in the experiment is provided by the useful or by the parasitic absorption.

According to optical simulations of Beck et. al. [6], the angular distribution of light scattered by a silver nanodisk placed directly on silicon is similar to the one of an ideal lambertian case given by the cosine law. Furthermore, Catchpole et. al. [8] demonstrated that the scattering occurs predominantly towards the high refractive index material, and that cylinders and hemispheres with the same diameter have almost identical scattering

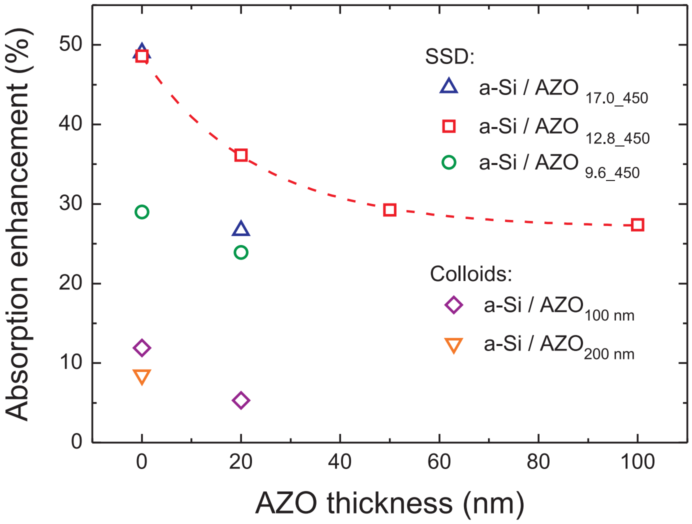

Figure 3.9: Total absorption enhancement, integrated over the 400 − 1000 nm wavelength range, of a 230 nm thick a-Si with: (i) Ag NPs formed from precursor film of 9.6, 12.8, and 17.0 nm annealed at 450°C for 1 h with the AZO spacer layer thickness varying from 0 to 100 nm; (ii) 100 and 200 nm diameter colloidal Au NPs. The enhancements are normalized to the bare a-Si film.

properties. Therefore, the theoretical useful absorption (A_T) provided by the discrete arrays of hemispherical Ag nanoparticles approximated by the lambertian scatterers can by expressed as a linear combination of the specular and diffused parts, given by the absorption of a flat a-Si film and the lambertian limit, as:

$$A_T(\lambda) = (1 - R_D(\lambda))A_{Spec}(\lambda) + R_D(\lambda)A_{Diff}(\lambda), \tag{3.2}$$

with a parameter $R_D(\lambda)$ describing the amount of light backscattered to the substrate, depending on the surface coverage of the NPs, their scattering cross-sections and the ratio of forward to back-scattering. The $A_{Spec}(\lambda)$ is the absorption of a flat a-Si film calculated numerically with the scattering matrix formalism using experimentally determined dielectric functions, while the $A_{Diff}(\lambda)$ represents the maximum absorption provided by the lam-

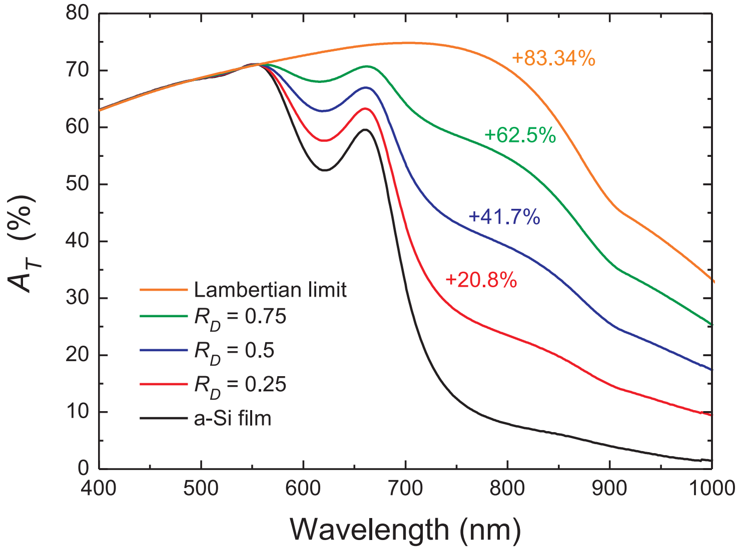

Figure 3.10: Theoretical useful absorption (A_T) provided by an array of ideal lambertian scatterers placed at the rear surface of a 230 nm thick a-Si calculated as a linear combination of bare flat film and the lambertian limit (equation 3.2) with the parameter R_D describing the amount backscattered light. Values of absorption enhancement over the flat reference are indicated for each curve.

bertian surface used as a back mirror, calculated analytically according to the approach of Green [9] and corrected by the reflections at air/glass and glass/a-Si interfaces to accurately represent the investigated structure. The resonant nature of plasmonic resonance results in a resonant spectral behavior of the $R_D(\lambda)$ function. Nonetheless, due to large NPs' sizes, the averaging over a NPs' size distribution, and the high refractive index of a-Si, a pronouncedly broad resonance is expected for the investigated nanostructures. Therefore, for the sake of simplicity, the theoretical useful absorption was calculated for constant values of R_D of 0.25, 0.5, and 0.75 and plotted together with the flat reference and lambertian limit in Fig. 3.10. This reveals that a considerable enhancement of useful absorption (indicated for each curve in Fig. 3.10) is achievable with an array of discrete particles, which does not fully scatter the incident radiation.

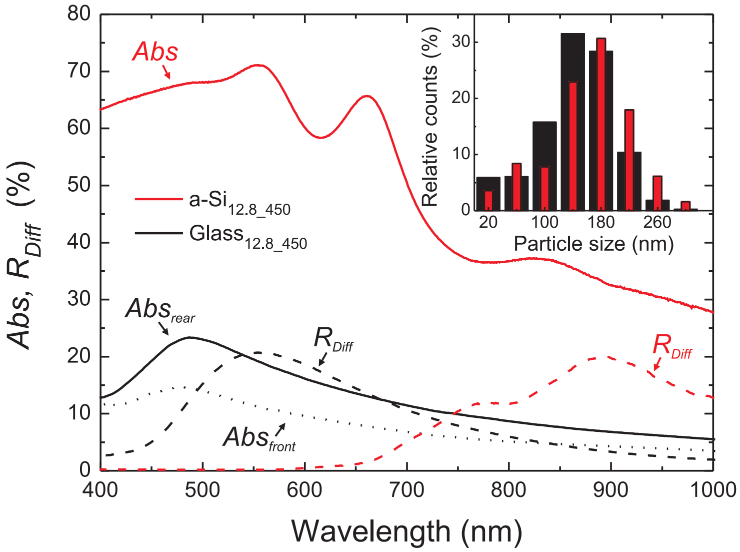

Figure 3.11: Absorption (Abs) and diffuse reflection (R_{Diff}) spectra of Ag NPs formed from 12.8 nm thick precursor film annealed at 450°C for 1 h on 230 nm thick a-Si (a-Si$_{12.8\_450}$) and on corning glass substrate (Glass$_{12.8\_450}$). The absorption of sample Glass$_{12.8\_450}$ is shown for both front- and rear-side illumination configuration. The remaining spectra were acquired in the rear-side configuration. The inset plot shows the distributions of NPs' sizes for the two samples.

According to the theoretical calculations presented in section 2.3 and widely available in the literature [6, 8, 10, 11], the parasitic absorption of NPs bigger than 100 nm is small compared to their scattering efficiency, which results in a significant enhancement of useful absorption. On the other hand, a notable discrepancy between the theoretical models and experimentally determined optical properties of NPs is found (section 2.4). The high optical losses are attributed to the presence of small particles in the nanostructure, the irregularly shaped NPs with sharp features, the inter-particle interactions, the sulfidation of NPs in atmospheric air, as well as the polycrystalline nature, defects and impurities present in the material forming the NPs.

The contribution of useful and parasitic absorption in the investigated structure is inseparable by the conventional optical spectroscopy technique. Nonetheless, the problem can be qualitatively analyzed by the comparison with the reference sample, fabricated in the same process, consisting of NPs formed on a transparent, low-absorbing glass substrate. Such comparison, in terms of Abs and R_{Diff} spectra, is depicted in Fig. 3.11 for sample a-Si$_{12.8\_450}$. As shown in the inset plot, both samples exhibit fairly similar distribution of NPs' sizes, which justifies the aforementioned comparison. The resonance intensities of Abs and R_{Diff} for the reference sample have similar values of 23% and 21%, respectively, and both characteristics decrease steadily toward near infrared reaching Abs of 5% at 1000 nm. However, a pronounced broadening and red-shift of the optical characteristics as well as spectral separation of Abs and R_{Diff} peaks is expected when NPs are placed in the vicinity of a high refractive index material. The measurement of R_{Diff} confirms spectral matching between the plasmonic resonance and the light trapping window of a-Si. Since the R_{Diff} is attenuated by the multi-pass through the a-Si, and it does not contain the part that was coupled to the guided modes one can conclude that scattering is enhanced in case of NPs placed directly on a-Si compared to the reference sample. In addition, according to the arguments given in section 2.5.2 the difference between absorption measured in the rear-side and in the front-side illumination configuration can be attributed to the geometry of the measurement system in which the light scattered at high angles, and coupled to the glass substrate by the total internal reflection, is accounted for absorption. Based on the given arguments, the total parasitic losses in the investigated structures can be reasonable estimated at 10 to 20% in the low absorbance regime ($800 - 1000$ nm).

It has been suggested that although the absorption cross-section of single NPs is indeed low, the considerable overall losses of weakly absorbed near-infrared light propagating through the a-Si slab arise from multiple interactions with the NPs [5, 12]. This effect become more pronounced with decreasing absorption coefficient, hence increasing illumination wavelength, and can be responsible for the high absorption measured close to the bandgap of a-Si.

3.2 Nanoparticles incorporated in substrate configuration

3.2.1 Sample preparation

In order to investigate the light trapping in substrate configuration thin film solar cells, self-assembled silver nanoparticles were incorporated in three distinct arrangements, depicted schematically in Fig. 3.12, which are considered as different stages of completion of a plasmonic back reflector.

The NPs were fabricated by solid-state dewetting (SSD) of 12 nm thick Ag film annealed at 400°C for 1 h in nitrogen atmosphere on (i) bare soda-lime glass (sample S_{NPs}), (ii) 50 nm thick aluminium doped zinc oxide (AZO) coated glass (sample $S_{\mathrm{AZO\_NPs}}$), and (iii) a stack of 100 nm flat Ag back reflector (BR) and 50 nm thick AZO spacer layer (sample $S_{\mathrm{BR\_NPs}}$). The reference samples without NPs (S_{AZO} and S_{BR},respectively) were fabricated along in the same processes. The depositions of Ag and AZO films were carried out with RF magnetron sputtering at a working pressure of 2.5×10^{-3} mbar in Ar atmosphere with a RF power density of 1 and 2.16 W/cm^2, respectively.

Thicknesses of Ag and AZO layers were determined using Rutherford Backscattering Spectrometry (RBS, 2.0 MeV He$^+$ beam) assuming the Ag density of 5.85×10^{22} Ag/cm^3 and Zn density in AZO of 3.22×10^{22} Ag/cm^3. The relative error of the thickness measurements was estimated at the level of 3%. The surface morphologies were investigated by Field Emission Scanning Electron Microscopy (SEM - Zeiss Supra 25 microscope) and Atomic Force Microscopy (AFM - Bruker Dimension Icon microscope in PeakForce mode). The optical properties of the NPs, in terms of total and diffuse reflection (R_{Total} and R_{Diff}, respectively), were measured using a Varian Cary 500 double-beam scanning UV-Vis-NIR spectrophotometer equipped with a 4-inch integrating sphere.

A 0.9 μm thick μc-Si:H layer was deposited on top of the five structures shown in Fig. 3.12 by Plasma Enhanced Chemical Vapor Deposition (PECVD) with a power density of 0.06 W/cm^2, a working pressure of 70 Pa, a flow of SiH_4 of 4 sccm, and a dilution ratio H_2/SiH_4 of 32, while keeping the samples' surface at 310°C. Film thickness was verified with an Alpha-step 100 profilometer.

Raman spectra of the μc-Si:H films were acquired at 785 nm, with low excitation intensity of 10 mW and accumulation time of 1 s, using a Ren-

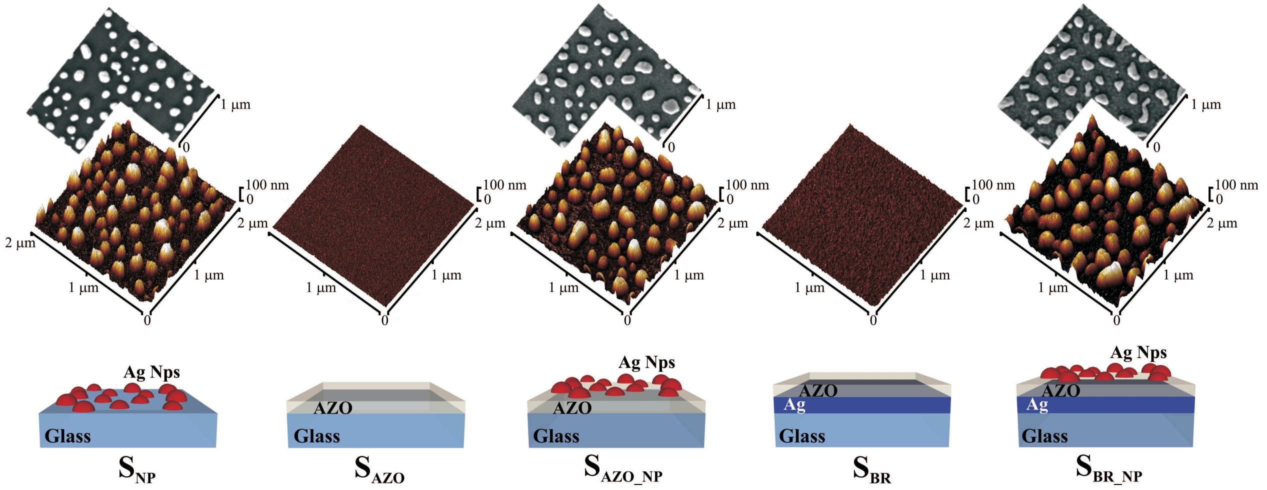

Figure 3.12: Schematic illustrations and corresponding surface morphologies of the distinct substrate configurations, with self-assembled Ag nanoparticles, for the investigation of light trapping in μc-Si:H thin films subsequently deposited on top of them. $\mathrm{S_{NPs}}$ - NPs on bare soda-lime glass; $\mathrm{S_{AZO}}$ - reference AZO coated glass; $\mathrm{S_{AZO\_NPs}}$ - NPs on AZO coated glass; $\mathrm{S_{BR}}$ - reference Ag back reflector coated with AZO; $\mathrm{S_{BR\_NPs}}$ - NPs on Ag back reflector coated with AZO. NPs were fabricated in the same deposition process from 12 nm thick Ag precursor film annealed at 400°C for 1 h. The thicknesses of all AZO films is 50 nm.

ishaw InVia Raman spectrometer. The absorption of light in the investigated structures was measured by highly sensitive photothermal deflection spectroscopy (PDS) [13] and Fourier-transform photocurrent spectroscopy (FTPS) [14]. Both techniques exhibit superior sensitivity over transmission/reflection spectroscopy and have extensively been used to analyze electronic defects in semiconductors [15, 16]. For the PDS spectroscopy a Fluorinert Electronic Liquid FC-72 with low refraction index of 1.25 was used in order to simulate conditions similar to air ambient (obtained absorption values were corrected taking into account reflection at the liquid/silicon interface). In order to collect the FTPS signal an arrangement with coplanar front electrode made of electrolyte and a transparent conductive oxide sandwich structure was used.

3.2.2 Structural and optical properties of NPs

The structural and optical properties of samples S_{NPs} and $S_{\mathrm{AZO\_NPs}}$ have already been discussed during the comparison of NP formation on glass and AZO substrate in section 2.5. In addition, a detailed study of the effect of the fabrication parameters on the morphology and optical properties of plasmonic back reflectors (sample $S_{\mathrm{BR\_NPs}}$) is included in section 4.1.1.

The morphology of NPs fabricated in different configurations analyzed by SEM and AFM is depicted in Fig. 3.12. The average size of NPs, determined from SEM images, was found to increase from 139 ± 2 nm to 169 ± 2 nm for the two substrates. As a result of the same underlying layer in SSD process, the NPs' morphologies of samples $S_{\mathrm{AZO\_NPs}}$ and $S_{\mathrm{BR\_NPs}}$ are expected to be fairly similar, though the NPs shapes were found to be slightly less uniform for the case of $S_{\mathrm{BR\_NPs}}$. The AFM analyses reveal that NPs have approximately hemispherical shape when formed on glass and tend to flatten out on AZO. The maximum heights were in both cases close to 100 nm.

Figure 3.13 depicts the optical properties, in terms of total and diffuse reflection measured in the front-side illumination configuration, of the five different substrates. An important parameter determining the optical performance of a sample for light trapping is the diffuse reflection, as it describes the amount of scattered photons which have an increased probability to be absorbed in the solar cell due to the enhanced optical path length. As expected, the two reference sample without NPs, S_{AZO} and S_{BR}, show negligible R_{Diff}. The NPs deposited on glass and AZO provide maximum diffuse reflection of about 10 and 8% at 550 and 680 nm, respectively. The

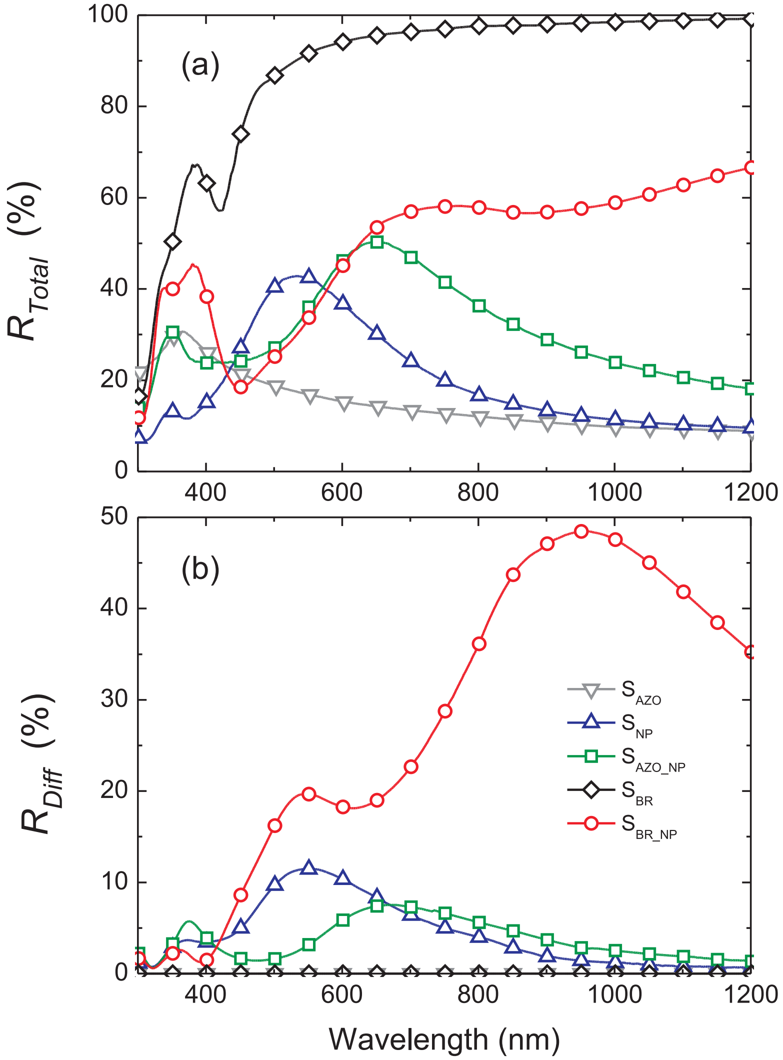

Figure 3.13: (a) Total and (b) diffuse reflection of the five distinct substrate configurations depicted in Fig. 3.12

R_{Diff} is however substantially enhanced in the wavelength range suitable for light trapping in μc-Si solar cells ($500-1100$ nm) when the NPs are coupled with flat back reflector (sample $\mathrm{S_{BR\_NPs}}$). This reveals that the mirror not only reflects the transmitted diffuse light coming from the NPs, but also originates a constructive interaction with the particles that increases their scattered power relative to the case when they are immersed in a homogeneous medium. At the same time, also the dissipative interaction of NPs with incident light (parasitic absorption) are enhanced resulting in the decrease of the total reflection with respect to almost 100% R_{Total} of the reference mirror (sample $\mathrm{S_{BR}}$).

3.2.3 Absorption enhancement

Aimed at the investigation of plasmonic light trapping for substrate configuration thin film solar cells, the five samples described in the previous section were used as substrates for the deposition of 0.9 μm thick μc-Si:H. The selected deposition conditions assure high degree of crystallinity required for the narrow bandgap, which allow for the optical absorption to extend up to 1100 nm in the near-infrared. On the other hand, the edge of complete extinction of light in a flat film deposited on AZO was measured at 500 nm.

Figure 3.14 depicts the Raman spectra of μc-Si:H films deposited on the five different substrates. The high degree of crystallinity allows also for the clear identification of the Si band in Raman spectra at approximately 520 cm^{-1}. Due to the use of glass substrate, the Raman spectrum of the amorphous Si phase is not extractable from the background signal. As discussed by Ledynský et. al. [17] the absolute intensity of the Raman signal is proportional to the path-length of excitation light in the silicon layer and to the light in/out-coupling efficiency. Furthermore, the spectrum acquired for sample $\mathrm{S_{AZO\_NPs}}$ with additional 50 nm thick AZO layer covering the NPs, and separating them from μc-Si:H, remains practically unchanged, which proves that the increase of Raman intensity is not caused by surface enhanced Raman scattering (SERS) originated from the high enhancement of the NPs' near-field at the plasmonic resonance. Therefore, the observed enhancements of Raman signal for samples containing the NPs, over the flat Si film, can be attributed to the efficient light trapping at the excitation wavelength providing an important insight into the enhancement of useful absorption.

The important issue for plasmon-induced light trapping is to scrutinize

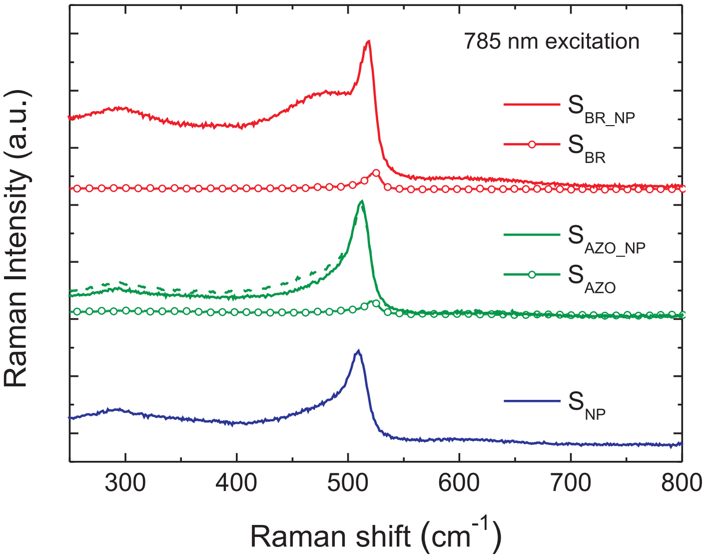

Figure 3.14: Raman spectra, measured with excitation at 785 nm, of 0.9 μm thick μc-Si:H deposited on the five different substrates depicted in Fig. 3.12. The peak at approximately 520 cm^{-1} originates from the microcrystalline phase of the films. The dashed curve refers to the sample S_{AZO_NPs} with additional 50 nm thick AZO layer covering the NPs. The curves are displaced vertically in the graph for better visualization.

between the absorption originating in the solar cell absorber layer and in the metallic NPs. Since the contributions of useful and parasitic absorptions are inseparable with conventional optical spectroscopy, a procedure involving a combination of opto-electronic spectroscopic techniques, namely PDS and FTPS, was employed in this work. The PDS signal accounts for all types of light absorption processes, while the FTPS accounts only for the light absorbed in μc-Si:H layer determined from the photo-generated current. The PDS and FTPS absorption spectra of 0.9 μm thick μc-Si:H deposited on samples S_{AZO}, S_{AZO_NPs}, and S_{BR_NPs} are plotted in Fig. 3.15. The only sources of optical losses in the reference sample are the thin AZO layer and the glass substrate, therefore both PDS and FTPS signals overlap indicating that practically all absorption occurs in silicon. Small discrepancy, on the order of 1%, is apparent above 950 nm when plotted in the logarithmic scale. It should be noted that the relatively low absolute values of absorption below 80% originate from the lack of the transparent contact deposited on top of silicon, which plays an important role as an antireflection coating.

The deposition of μc-Si:H on the substrates containing the NPs resulted in considerable enhancement of useful absorption in the entire investigated wavelength range. The parasitic losses, calculated as the difference between PDS and FTPS spectra, start to play role only for the wavelengths above 730 nm, which are already poorly absorbed in flat films, and increase significantly towards the bandgap of μc-Si:H. This behavior can be explained by assuming that the total parasitic absorption arise from multiple interactions between the incident light and the NPs. The number of such interactions for weakly absorbed near-infrared light trapped in a silicon slab (depicted schematically in the inset of Fig. 3.15) increases substantially with decreasing absorption coefficient, hence increasing illumination wavelength. Consequently, the vast number of interactions results in significant overall losses even if, as predicted by theoretical calculations [6, 10], the absorption cross-section is small compared to scattering cross-section. Therefore, in the $500 - 700$ wavelength range, where the light has a high probability to generate photo-carriers after only a few scattering events, the parasitic absorption play only minor role.

The scattering properties of particles are strongly dependent on the dielectric function of the embedding medium [10], therefore also on the distance between the NPs and high refractive index material [6, 18]. The FTPS signal of sample $\mathrm{S_{BR\_NPs}}$ with additional 50 nm thick AZO layer separating NPs and silicon (see Fig. 3.15), exhibits a significant blue-shift of the absorption edge and thus a clearly lower enhancement of useful absorption in the near infrared region. This effect can be attributed to the narrowing of the angular distribution function of scattered light, hence lower light coupling efficiency, with decreasing overlap between the NPs' near field and the silicon. The spacer layer in solar cells is required for a barrier for the diffusion of metal atoms into the silicon, thus preventing from the deterioration of the electrical properties of the doped layer and consequent degradation of the p-i-n junction. Nonetheless, the separation should be kept as thin as possible to ensure high enhancements of useful absorption.

The conformal growth of μc-Si:H films on top of the NPs results in a random texturing of their front surface. The surface morphologies were found

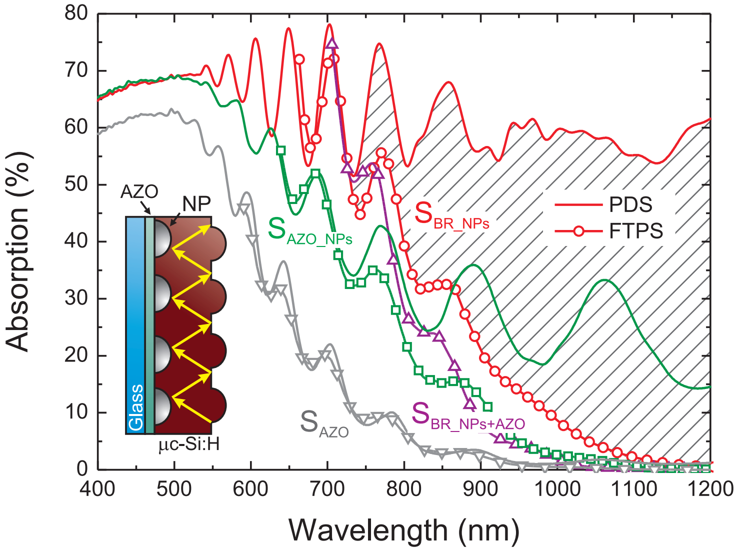

Figure 3.15: Total (PDS) and useful (FTPS) absorption spectra of 0.9 μm thick μc-Si:H deposited on samples S_{AZO}, $S_{\mathrm{AZO\_NPs}}$, and $S_{\mathrm{BR\_NPs}}$, depicted in Fig. 3.12. The FTPS absorption for sample $S_{\mathrm{BR\_NPs}}$ with additional 50 nm thick AZO layer separating NPs and silicon is shown for comparison. The marked area represents the parasitic absorption for sample $S_{\mathrm{BR\_NPs}}$ being the difference between PDS and FTPS spectra. The inset illustrates schematically light trapped in Si by total internal reflection.

to be fairly similar for the three film deposited on substrates containing NPs (S_{NPs}, $S_{\mathrm{AZO\_NPs}}$, and $S_{\mathrm{BR\_NPs}}$) having root mean square (RMS) roughness ranging from 20 to 24 nm. As such two distinct light trapping mechanisms are contributing to the overall useful absorption and Raman enhancements: (i) improved light coupling into silicon (antireflection action) provided by the surface texture, and (ii) scattering of light by the plasmonic nanoparticles. The high energy photons are entirely absorbed in their first pass through the μc-Si:H film and therefore do not reach the back side of the film and have no possibility to interact with the NPs. As such, the higher absorption measured at wavelengths shorter than 500 nm for samples with NPs can only be attributed to the front surface texture. In the light trap-

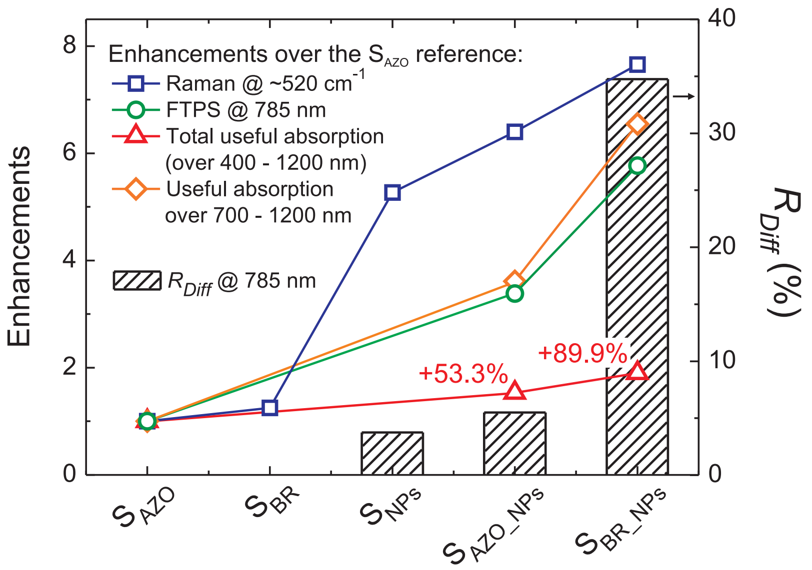

Figure 3.16: Enhancements over the reference flat film (S_{AZO}) of the Raman Si-band peak at $\sim 520\,\mathrm{cm}^{-1}$, the FTPS absorption at 785 nm, the overall useful absorption integrated over $400 - 1200\,\mathrm{nm}$, and the red-NIR part of useful absorption integrated over $700 - 1200\,\mathrm{nm}$, provided by the different substrates depicted in Fig. 3.12. The enhancements are correlated with diffuse reflection at 785 nm measured prior to the deposition of μc-Si:H.

ping window, both mechanisms can originate the observed enhancement of useful absorption and the their contributions cannot be measured separately. Nonetheless, the computational study by Kowalczewski et. al. [19] shows that small rms roughness ($< 50\,\mathrm{nm}$) results mostly in the improved absorption of the high energy photons and its effectiveness is decreasing with increasing illumination wavelength. On the other hand, the plasmonic scattering have more pronounced impact in the red and near-infrared part of the spectrum due to the pronounced red-shift of the resonance for NPs placed in the vicinity of high refractive index material.

Figure 3.16 depicts the enhancements provided by the different substrates, over the reference flat film (sample S_{AZO}), of the Raman Si-band peak at $\sim 520\,\mathrm{cm}^{-1}$, the FTPS absorption at 785 nm, the overall useful absorption integrated over 400 − 1200 nm, and the red-NIR part of useful absorption integrated over 700 − 1200 nm. The enhancements are compared to the diffuse reflection at 785 nm measured prior to the deposition of μc-Si:H films. The values of FTPS enhancement and R_{Diff} were taken at the wavelength corresponding to the excitation laser used for Raman spectroscopy. The flat back reflector coupled with a flat μc-Si:H film effectively doubles the path-length of light inside Si, which is meaningful only in the range 500 − 700 nm where specularly reflected light has still a high probability of being absorbed in the second pass through Si. Thus, the Ag mirror of sample $\mathrm{S_{BR}}$ has been found to provide minor, 1.25, enhancement of the Raman signal acquired at 785 nm. On the other hand, considerable enhancements of 6.3 and 7.6 were found for the films deposited on substrates $\mathrm{S_{AZO\_NPs}}$ and $\mathrm{S_{BR\_NPs}}$, respectively. Since the antireflection action provided by the surface texture is expected to contribute equally to light trapping in all samples containing NPs, and since the plasmonic scattering increases significantly in presence of flat back mirror, it can be concluded that the enhancements of sample $\mathrm{S_{BR\_NPs}}$ over $\mathrm{S_{AZO\_NPs}}$ are dominated by the plasmonic light trapping. For sample $\mathrm{S_{AZO\_NPs}}$ the contributions of the two light trapping mechanisms are inseparable by simple optical spectroscopy, though it can be argued that due to significant difference of R_{Diff} between $\mathrm{S_{AZO\_NPs}}$ and $\mathrm{S_{BR\_NPs}}$, the enhancements result, in majority, from the texturing. Furthermore, the enhancements of useful absorption in 700 − 1200 nm wavelength range and FTPS at 785 nm correlate well with the increase of diffuse reflection, which proves that the increase of useful absorption in red-NIR part of the spectrum originates mostly from the plasmonic scattering. This claim is also confirmed by the blue-shift of the useful absorption edge observed for sample $\mathrm{S_{BR\_NPs}}$ with a 50 nm thick AZO layer separating NPs and silicon. Finally, the deposition of 0.9 μm thick μc-Si:H on self-assembled Ag NPs coupled with a flat mirror resulted in significant enhancement of the useful absorption, in the entire investigated spectral range, of 89.9%.

3.3 Conclusions

In this chapter, an absorption enhancement provided by self-assembled silver nanoparticles incorporated in thin silicon films in substrate and superstrate configuration is investigated.

The structural properties of NPs formed on bare a-Si film, with various precursor film thicknesses and AZO spacer layers, were investigated and correlated with the absorption enhancement in silicon film. The coupling efficiency has been found to (i) increase with NPs' average size and saturate above 180 nm, (ii) to decrease with increasing thickness of the spacer between silicon and NPs and to saturate above 50 nm, (iii) to be significantly smaller for spherical than for hemispherical NPs. Obtained results confirm qualitatively the theoretical predictions found in the literature [6, 8].

A novel procedure employed in this work, involving a combination of opto-electronic spectroscopic techniques, namely PDS and FTPS, allowed for the quantification of useful and parasitic absorption in 0.9 μm thick μc-Si:H deposited on a plasmonic back reflector. It has been found that the optical losses in the NPs are insignificant in the $500 - 730$ nm wavelength range, beyond which they increase rapidly with increasing illumination wavelength. This is explained by the substantial increase of the number of interactions between NPs and long-wavelength photons, due to the rapid drop of semiconductor's absorption coefficient, which accounts for the overall losses. Nonetheless, a significant broadband useful absorption enhancement of 89.9% has been achieved, which can be attributed to both the random front surface texture, originated from the conformal growth of Si on top of the NPs, and to the scattering of light by the plasmonic NPs.

References

[1] C. A. Schneider, W. S. Rasband, and K. W. Eliceiri, "NIH Image to ImageJ: 25 years of image analysis," *Nature Methods*, vol. 9, p. 671675, 2012.

[2] S. Kageyama, M. Akagawa, and H. Fujiwara, "Dielectric function of a-Si:H based on local network structures," *Phys. Rev. B*, vol. 83, p. 195205, 2011.

[3] M. J. Mendes, S. Morawiec, F. Simone, F. Priolo, and I. Crupi, "Colloidal plasmonic back reflectors for light trapping in solar cells," *Nanoscale*, vol. 6, no. 9, pp. 4796–4805, 2014.

[4] R. Santbergen, H. Tan, M. Zeman, and A. H. M. Smets, "Enhancing the driving field for plasmonic nanoparticles in thin-film solar cells," *Optics Express*, vol. 22, no. S4, pp. A1023–A1028, 2014.

[5] A. M. Pennanen and J. J. Toppari, “Direct optical measurement of light coupling into planar waveguide by plasmonic nanoparticles,” *Optics Express*, vol. 21, no. S1, pp. A23–A35, 2013.

[6] F. J. Beck, S. Mokkapati, and K. R. Catchpole, “Light trapping with plasmonic particles: beyond the dipole model,” *Opt. Express*, vol. 19, no. 25, pp. 25 230–25 241, 2011.

[7] P. N. Saeta, V. E. Ferry, D. Pacifici, J. N. Munday, and H. A. Atwater, “How much can guided modes enhance absorption in thin solar cells?” *Opt. Express*, vol. 17, no. 23, pp. 20 975–20 990, 2009.

[8] K. R. Catchpole and A. Polman, “Design principles for particle plasmon enhanced solar cells,” *Applied Physics Letters*, vol. 93, no. 19, 2008.

[9] M. A. Green, “Lambertian light trapping in textured solar cells and light-emitting diodes: analytical solutions,” *Progress in Photovoltaics: Research and Applications*, vol. 10, no. 4, pp. 235–241, 2002.

[10] T. L. Temple and D. M. Bagnall, “Broadband scattering of the solar spectrum by spherical metal nanoparticles,” *Progress in Photovoltaics: Research and Applications*, vol. 21, no. 4, pp. 600–611, 2013.

[11] A. Paris, A. Vaccari, A. Cal Lesina, E. Serra, and L. Calliari, “Plasmonic scattering by metal nanoparticles for solar cells,” *Plasmonics*, vol. 7, no. 3, pp. 525–534, 2012.

[12] C. S. Schuster, S. Morawiec, M. J. Mendes, M. Patrini, E. R. Martins, L. Lewis, I. Crupi, and T. F. Krauss, “Plasmonic and diffractive nanostructures for light trapping an experimental comparison,” *Submitted to Optica.*

[13] W. B. Jackson, N. M. Amer, A. C. Boccara, and D. Fournier, “Photothermal deflection spectroscopy and detection,” *Appl. Opt.*, vol. 20, no. 8, pp. 1333–1344, Apr 1981.

[14] J. Holovsky, “Fourier transform photocurrent spectroscopy on non-crystalline semiconductors,” in *Fourier Transforms - New Analytical Approaches and FTIR Strategies*, G. Nikolic, Ed. InTech, 2011.

[15] A. Poruba, M. Vaněček, J. Meier, and A. Shah, "Fourier transform infrared photocurrent spectroscopy in microcrystalline silicon," *Journal of non-crystalline solids*, vol. 299, pp. 536–540, 2002.

[16] S. De Wolf, J. Holovsky, S.-J. Moon, P. Loper, B. Niesen, M. Ledinsky, F.-J. Haug, J.-H. Yum, and C. Ballif, "Organometallic halide perovskites: Sharp optical absorption edge and its relation to photovoltaic performance," *The Journal of Physical Chemistry Letters*, vol. 5, no. 6, pp. 1035–1039, 2014.

[17] M. Ledinsk, E. Moulin, G. Bugnon, K. Ganzerov, A. Vetushka, F. Meillaud, A. Fejfar, and C. Ballif, "Light trapping in thin-film solar cells measured by raman spectroscopy," *Applied Physics Letters*, vol. 105, no. 11, 2014.

[18] S. Pillai, F. J. Beck, K. R. Catchpole, Z. Ouyang, and M. A. Green, "The effect of dielectric spacer thickness on surface plasmon enhanced solar cells for front and rear side depositions," *Journal of Applied Physics*, vol. 109, no. 7, 2011.

[19] P. Kowalczewski, M. Liscidini, and L. C. Andreani, "Light trapping in thin-film solar cells with randomly rough and hybrid textures," *Optics express*, vol. 21, no. 105, pp. A808–A820, 2013.

Chapter 4

Plasmonic solar cells

The first part of this chapter reports a successful implementation of a plasmonic light trapping scheme implemented in a thin film a-Si:H solar cell in plasmonic back reflector (PBR) configuration. The optical properties of the PBRs are systematically investigated according to the morphology of the self-assembled silver nanoparticles (NPs), which can be tuned by the fabrication parameters. By analyzing sets of solar cells built on distinct PBRs, it is shown that the photocurrent enhancement achieved in the a-Si:H light trapping window ($600-800\,\mathrm{nm}$*) stays in linear relation with the PBRs diffuse reflection. The best-performing PBRs allow a pronounced broadband photocurrent enhancement in the cells which is attributed not only to the plasmon-assisted light scattering from the NPs but also to the front surface texture originated from the conformal growth of the cell material over the particles. As a result, remarkably high values of* J_{sc} *and* V_{oc} *are achieved in comparison to those previously reported in the literature for the same type of devices.*

In the second part an attempt on implementation of the plasmonic light trapping in the industrial a-Si/μ*c-Si double junction solar cells is presented. The effect of annealing on the electrical performance is tested, and reveals that the fill factor, and hence the efficiency, increases at moderate annealing temperatures. The implementation of metallic NPs resulted in the decrease of external quantum efficiency (EQE) due to the high parasitic absorption in the NPs and corrugated back reflector.*

4.1 Broadband photocurrent enhancement in a-Si:H solar cells with plasmonic back reflectors

4.1.1 Plasmonic back reflectors

Sample preparation and characterization

Plasmonic back reflectors (PBRs), schematically shown in Fig. 4.1(a), were fabricated on soda-lime glass substrates by sequential deposition of a 100 nm thick Ag mirror, a 40 nm thick aluminum-doped zinc oxide (AZO) spacer layer, and a thin precursor Ag film (t_{Ag}), using RF magnetron sputtering. The sputtering of the precursor Ag film was performed with a relatively high power of 1 $\mathrm{Wcm^{-2}}$ and low a working pressure of 1×10^{-2} mbar, at a rate of 0.8 nm/s. AZO layers were deposited with a power of 2.8 $\mathrm{Wcm^{-2}}$ at a working pressure of 10×10^{-3} mbar. The deposition was followed by annealing in flowing nitrogen, in which self-assembled NPs are formed by solid-state dewetting (SSD) from the topmost thin Ag layer. In order to embed the NPs, a coating of 80 nm AZO was deposited as the last fabrication step.

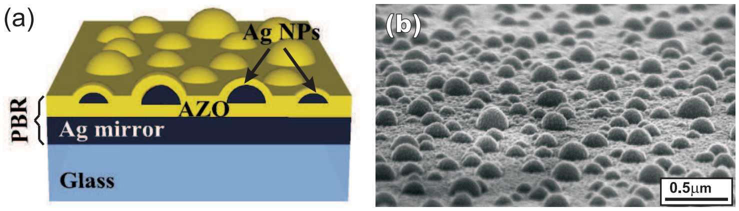

Figure 4.1: (a) Schematic drawing of a plasmonic back reflector (PBR) with the structure: Glass substrate/100 nm Ag mirror/40 nm AZO spacer/Ag NPs/80 nm AZO cover. (b) 70° tilted SEM image of the surface morphology of a PBR with NPs formed from a 8 nm thick Ag film annealed at400°C for 1 h, covered with a 80 nm AZO layer.

The NP structures investigated in this work were formed from 8 and 12 nm thick Ag films annealed in a variety of conditions: temperature ranging from 200 to 500°C and time ranging from 0.5 to 4 h. Reference BRs without NPs were fabricated in the same processes by partially covering the samples during the deposition of the Ag precursor film, in order to avoid NPs formation. A deposition procedure allowing for high uniformity and high, ±0.35 nm, precision of Ag film thickness among up to 9 substrates processed in one deposition run was developed for this work. Such approach enables a fair comparison between samples fabricated in the same process.

The thicknesses of the Ag and AZO layers were determined from Rutherford Backscattering Spectrometry (RBS, 2.0 MeV He^+ beam) in high resolution mode. The morphology of the NPs was investigated by Field Emission Scanning Electron Microscopy (SEM Zeiss Supra 25 microscope). The distributions of NPs were determined by digital analysis of SEM images conducted with the ImageJ software [1]. The surface morphology of a PBR with NPs formed from a 8 nm Ag precursor film is shown in the tilted SEM of Fig. 4.1(b). The optical properties of the PBRs, in terms of total and diffuse reflection (R_{Total} and R_{Diff}, respectively), were measured using a Varian Cary 500 double-beam scanning UV-Vis-NIR spectrophotometer equipped with a 4-inch integrating sphere.

Structural and optical properties

The morphology of the NPs has a strong impact on the optical properties of the PBRs and can be tuned by several parameters, such as the thickness of the precursor Ag film, annealing temperature and annealing time. It is generally desirable to prevent the formation of small (diameters < 60 nm) or irregularly-shaped NPs, as they are known to increase the parasitic absorption. At the same time, big NP sizes (heights > 200 nm) are not desirable as they can degrade the electrical properties of the cells due to the roughness induced in the Si layers [2]. The impact of the AZO spacer layer thickness on the scattering and parasitic absorption was recently investigated by Sesuraj et. al. [3] who reported an optimum value in the range of $40 - 50$ nm, depending on the size of the NPs. Tan et. al. [2] reported that an AZO cover layer of at least 60 nm flattens out the sharp surface features caused by the NPs, preventing them from deteriorating the quality of the a-Si:H cell layers.

For typical a-Si:H solar cells with ~ 300 nm thick intrinsic region, the wavelength range in which light trapping can provide significant photocurrent gain extends from 600 to 800 nm, which is the range between the full extinction of light in a single pass through the cell and the bandgap of the amorphous silicon. The main optical quantity that describes the suitability of the PBRs for light trapping is their diffuse reflection (R_{Diff}), as it determines the amount of light scattered away from the specular direction and,

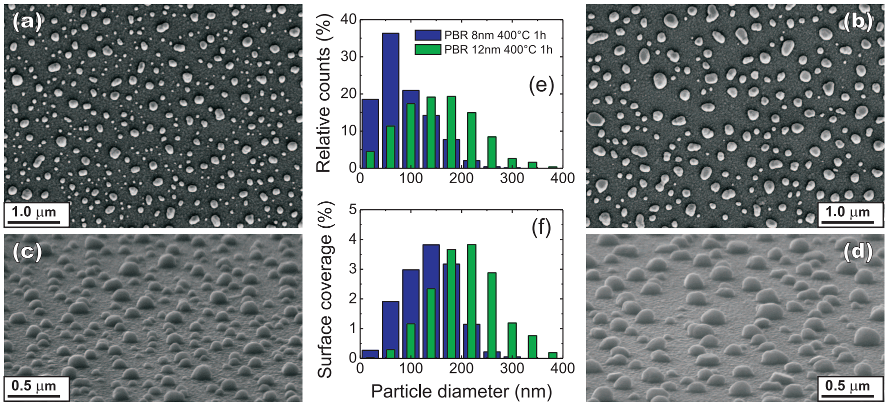

Figure 4.2: (a-b) Planar and (c-d) 70° tilted SEM micrographs of uncovered NPs formed, respectively, from 8 and 12 nm thick Ag films annealed at 400°C for 1 h. (e) Histogram of relative counts (counts normalized to the total number of NPs) and (f) histogram od surface coverage, as a function of the NPs in-plane diameter corresponding to the NPs presented in the micrographs.

thus, the amount of photons that have an increased probability to generate photocurrent and contribute to the absolute increase of EQE. The contribution of the PBRs specular reflection (R_{Total} - R_{Diff}) is only significant at the wavelengths ($550 - 650$ nm) that are not fully absorbed during the first pass through the cell but have high probability of being absorbed in the second pass after the specular reflection. However, due to the rapid decrease of the absorption coefficient for longer wavelengths, in the near bandgap region ($650 - 800$ nm) only the R_{Diff} plays a role since the light requires path length enhancements much higher than the cell thickness to be absorbed.

Figure 4.2 depicts the morphology, in planar and 70° tilted views, of the NPs formed from 8 (left-hand side - (a) and (c)) and 12 nm (right-hand side - (b) and (d) thick Ag films annealed in the same process (400 °C for 1 h). From the analysis of the tilted SEM images [Figs. 4.2(c) and 4.2(d)], it was found that NPs have roughly semi-spherical cross-section shape and tend to flatten out with increasing size. The corresponding relative counts and surface coverage distributions of the NPs in-plane diameters are shown in Fig.4.2(e) and 4.2(f), respectively. Comparing the two samples, the nanostructure formed from 8 nm of Ag contains a higher number of particles with diameter lower than 80 nm. The mean surface coverage (see chapter 2), increases from 136 ± 4 to 206 ± 2 nm when the precursor film thickness is increased from 8 to 12 nm. Thicker Ag films would result in less uniform NP geometries with bigger NP sizes, which can be disadvantageous due to the increased roughness that they produce in the solar cell material.

Figure 4.3 depicts the spectral behavior of the total and diffuse reflection of a reference flat back reflector and two PBRs with NPs formed from 8 and 12 nm thick Ag films, annealed in the same conditions (400°C for 1 h), before and after the final deposition of the AZO cover layer. As expected, the reference BR shows nearly 100% R_{Total} and almost negligible R_{Diff} over the a-Si:H light trapping spectral window. The PBR with uncovered NPs formed from 8 nm of Ag shows a broad single peak resonance with maximum at 800 nmm, while the 12 nm one shows a double-peak behavior with maxima at 500 and 1050 nm. The embedment of the NPs in AZO results in, first, the decrease of R_{Total}, second, the increase of R_{Diff}, and third, the spectral broadening of R_{Diff}. Unexpectedly, the R_{Diff} and R_{Total} of both PBRs become similar in the light trapping window after covering with AZO. The differences, however, are evident in the NIR region as the R_{Diff} plateau of the 12 nm PBR extends 300 nm further to longer wavelengths, from 800 to 1400 nm.

The distinct behavior of the PBRs with NPs formed from 8 and 12 nm of Ag originates from the distinct NPs morphology. As the 12 nm structure contains bigger NPs, the broad dipolar resonance peak is redshifted relative to the 8 nm one, and the quadrupole mode is more pronounced resulting in the R_{Diff} peak at $400 - 500$ nm. The higher number of small NPs present in the 8 nm sample causes higher parasitic absorption, thus, the values of R_{Total} are lower than those of the 12 nm sample, for both covered and uncovered NPs. The effects related to the embedment of the NPs in the AZO are chiefly attributed to the change in effective refractive index of the material surrounding the NPs, which redshifts and increases both the scattering (higher R_{Diff}) and the absorption (lower R_{Total}) cross sections of the NPs [4, 5]. As discussed in section 2.3, this effect is more pronounced for NPs smaller that 100 nm. Therefore, due to the presence of significant number of NPs with sizes around 100 nm in both samples short wavelength slope of LSP resonance is similar in both cases. On the other hand, notably broader size distribution of NPs formed from 12 nm result in significantly broader R_{Diff} plateau.

Figure 4.4 depicts the comparison between NPs formed from 12 nm thick

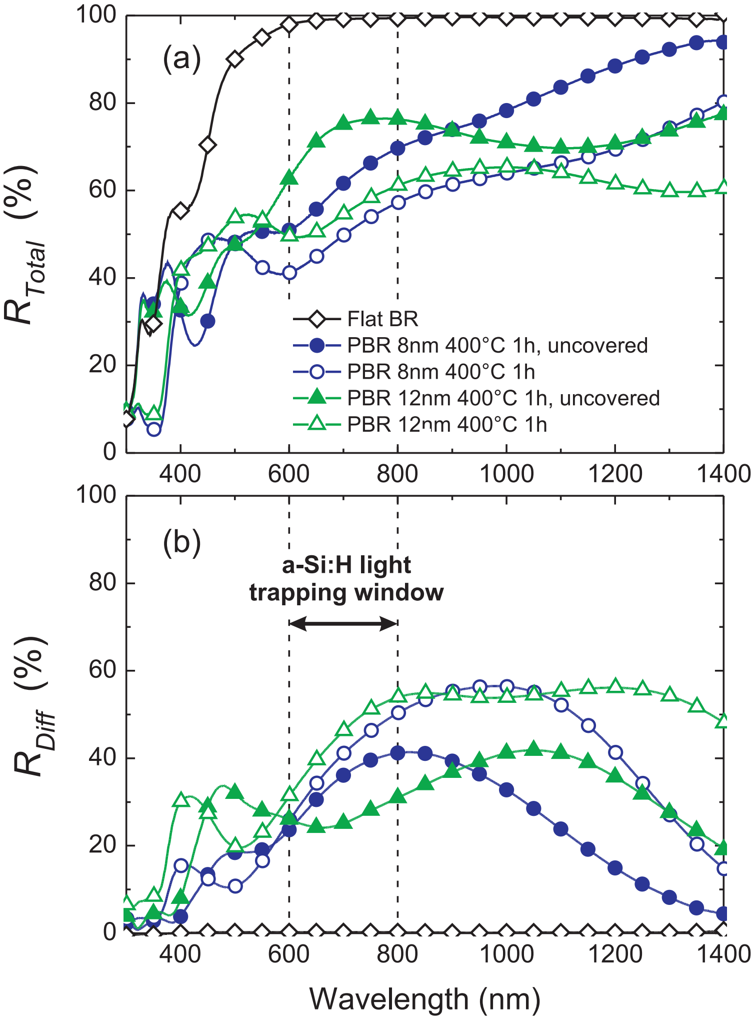

Figure 4.3: (a) Total and (b) diffuse reflection of the plasmonic back reflectors (PBRs) with NPs formed from 8 (circles) and 12 nm (triangles) thick Ag films annealed at 400°C for 1 h, before (solid symbols) and after (open symbols) the deposition of the AZO cover layer. The R_{Total} and R_{Diff} of a flat BR reference (without NPs) are also shown (open diamonds) for comparison. The wavelength range important for light trapping in a-Si:H (600 – 800 nm) solar cells is indicated by the vertical dashed lines.

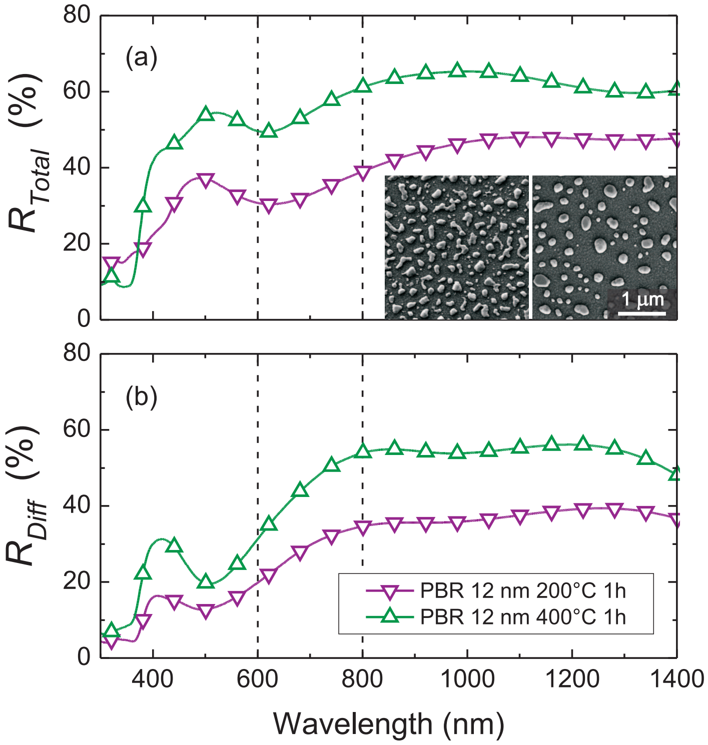

Figure 4.4: (a) Total and (b) diffuse reflection of the plasmonic back reflectors (PBRs) with NPs formed from 12 nm thick Ag film annealed at 200°C and 400°C for 1 h. The inset shows the SEM images of the corresponding samples, with 200°C on the left and 400°C on the right. The light trapping wavelength range of a-Si:H (600 − 800 nm) solar cells is indicated by the vertical dashed lines.

Ag film after annealing at 200°C and 400°C for 1 h. First of all, samples fabricated at lower temperature exhibit significantly worse performance in both R_{Total} and R_{Diff} in the whole investigated spectral region. It originates from the irregularly shaped NPs and high surface coverage obtained at low annealing temperatures. As shown in the SEMs in the inset of Fig. 4.4, a pronounced change in nanostructure morphology from elongated islands to round NPs is observed with the temperature increased form 200 (left-hand side) to 400°C (right-hand side). In addition, the reduction in the number of small particles and decline of the surface coverage is observed. This reveals the requirement of the elevated temperatures for NP formation, in accordance with the previous study discussed in section 2.4. Such high temperatures forbid the implementation of SSD-formed NPs as a post-process on top of thin film silicon cells, since the SiH bonds are damaged at temperatures $\sim 200°C$. Therefore, the main advantage of PBR configuration is that the a-Si:H p-i-n structure is not affected by the annealing step performed prior to the deposition of solar cell.

Figure 4.5 depicts the annealing time dependent evolution of the NPs' morphology formed from 8 nm thick Ag film annealed at 400°C for 0.5, 1, and 4 h, and the corresponding changes of their optical response. The extended annealing time clearly favors the formation of more uniform distributions of sizes and shapes of NPs resulting in desirable higher total and importantly diffuse reflection of the PBR and slight blue-shift of the resonance peak. Comparison between the three samples reveals that NPs smaller than 60 nm contribute most significantly to parasitic absorption in the spectral range important for light trapping in a-Si:H solar cells. The samples annealed for 0.5 and 1 h contain similar number of small particles and thus both have comparable R_{Total} in the visible range. In contrary, the small NPs are almost not present in the sample with annealing time extended to 4 h resulting in lower parasitic absorption and hence higher R_{Total} in the $400 - 800$ nm range. The lower parasitics in red-NIR region can be attributed to more regular NP shape, lower surface coverage and possible improvement of NPs' crystallinity. The later claim is supported by the observation of the polycrystalline nature of as deposited NPs, fabricated by both stencil deposition [6] and deposition of ultra-thin film below the percolation threshold [7, 8]. Furthermore, according to the free electron model, the dissipative interactions of electrons with crystal defects and grain boundaries are more pronounced with increasing illumination wavelength, as discussed in section 1.3.1.

Similar evolution of nanostructure morphology and corresponding optical response was observed for NPs' formed from 12 nm, as shown in Fig. 4.6. With short annealing time irregular nanostructures are formed, however, notably better than the ones obtainable at low annealing temperatures. As the thermal budget is increased, desirable round NPs tend to form. Furthermore, the surface coverage and the number of small particles decreases leading to a structure practically without NPs smaller than 80 nm obtained with annealing time prolongated up to 4 h. The changes in NPs' morphology

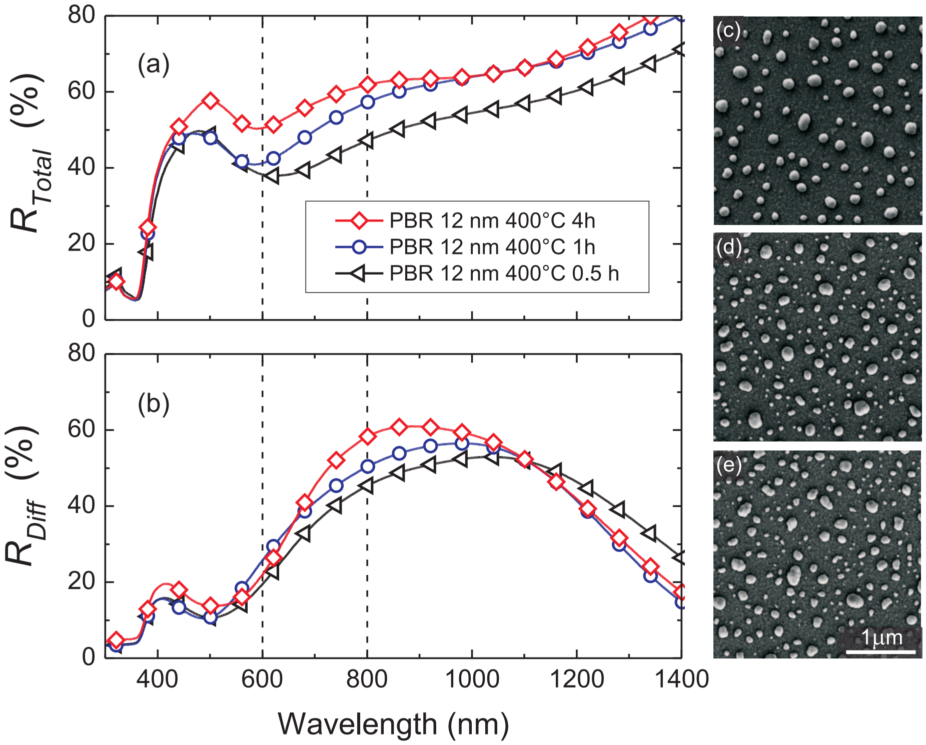

Figure 4.5: (a) Total and (b) diffuse reflection of the plasmonic back reflectors (PBRs) with NPs formed from 8 nm thick Ag film annealed at 400°C for 0.5, 1, and 4 h. Corresponding NPs' morphology is shown in the SEM images (c), (d), and (e), respectively. The light trapping wavelength range of a-Si:H ($600-800$ nm) solar cells is indicated by the vertical dashed lines.

result in the improvement of their optical performance, namely reduced parasitic absorption seen in the increase of R_{Total} over the entire investigated spectral range. The slight reduction of R_{Diff} in the $600-800$ nm range can be attributed to little lower number of particles with sizes around 100 nm. The most pronounced improvements of both total and diffuse reflections were observed with annealing time increased from 0.5 to 1 h, which results from the fact that the rate of morphological changes saturate approaching the thermal equilibrium condition.

At the LSP resonance frequencies, the ratio of R_{Diff} to R_{Total} exceeds

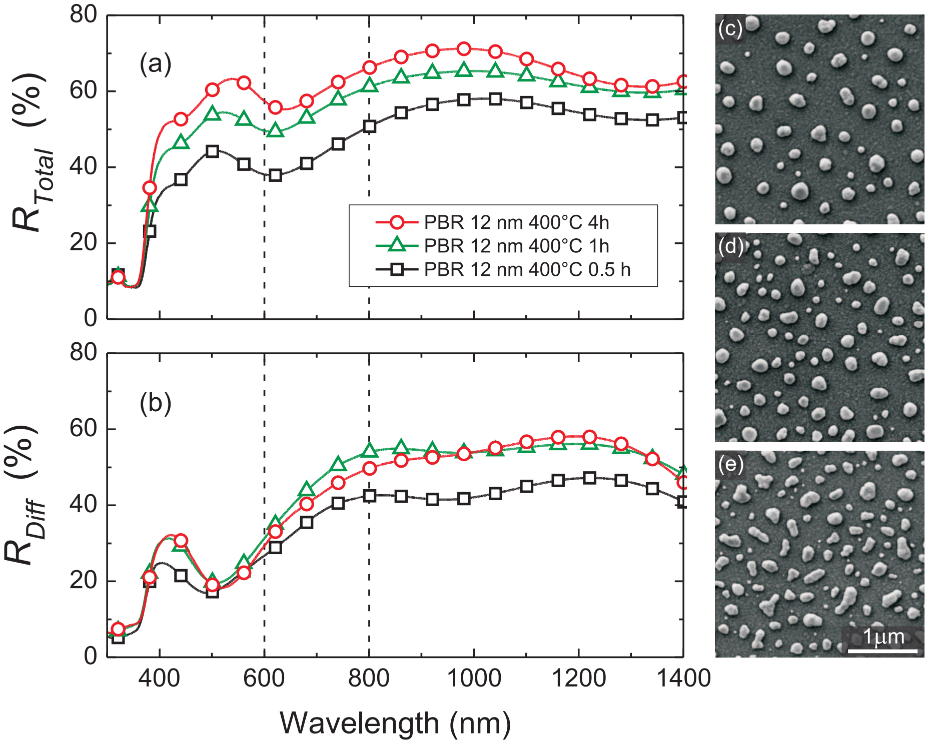

Figure 4.6: (a) Total and (b) diffuse reflection of the plasmonic back reflectors (PBRs) with NPs formed from 12 nm thick Ag film annealed at 400°C for 0.5, 1, and 4 h. Corresponding NPs' morphology is shown in the SEM images (c), (d), and (e), respectively. The light trapping wavelength range of a-Si:H (600 − 800 nm) solar cells is indicated by the vertical dashed lines.

90% for all previously discussed samples, which proves that practically all the incident photons interact with the NPs since almost all the light that is not absorbed is reflected diffusively from the PBRs. Therefore, the main factor limiting the performance of the PBRs is the parasitic absorption. In this respect, there is a significant discrepancy between theoretical calculations and experimental results since, according to single-particle electromagnetic modeling, Ag NPs with sizes above 100 nm should exhibit dominant scattering and negligible absorption cross section [4, 9–11], as discussed in section 2.3. Though the origin of the unexpectedly high absorption remains unclear, it can be attributed to dissipative interactions between the NPs themselves and between the NPs and the mirror, the roughness and sharp features of the NPs, and the possible polycrystalline nature of the NPs material [6].

Average reflections

The suitability of a particular PBR for application in thin film a-Si:H solar cells depends on its optical properties which can be characterized by the average total reflection, $\langle R_{Total}\rangle$, and the average diffuse reflection, $\langle R_{Diff}\rangle$, in the light trapping wavelength range from λ_1 to λ_2:

$$\langle R_X\rangle_{\lambda_2-\lambda_1} = \frac{\int_{\lambda_1}^{\lambda_2} R_X \mathrm{d}\lambda}{\lambda_2-\lambda_1} \tag{4.1}$$

where X corresponds to Total or Diff.

The dependence of $\langle R_{Total}\rangle_{600-800\,\mathrm{nm}}$ and $\langle R_{Diff}\rangle_{600-800\,\mathrm{nm}}$ on annealing time is shown in Fig. 4.7 for the PBRs with NPs formed from 8 and 12 nm thick Ag films annealed at 200, 400 and 500°C. First of all, samples fabricated at 200°C exhibit significantly worse performance, in both $\langle R_{Total}\rangle_{600-800\,\mathrm{nm}}$ and $\langle R_{Diff}\rangle_{600-800\,\mathrm{nm}}$, than those fabricated at elevated temperatures of 400 and 500 °C. As discussed previously, such lower performance originates from the irregular nanostructures, which are obtained at low annealing temperatures revealing the need to use a high temperature for NP formation.

The saturation behavior of $\langle R_{Total}\rangle_{600-800\,\mathrm{nm}}$ and $\langle R_{Diff}\rangle_{600-800\,\mathrm{nm}}$ for the annealing time exceeding 1 h is observed for all the samples, except that fabricated from a 8 nm thick Ag film annealed at 500°C. Furthermore, the 12 nm samples show systematically higher values of total reflection than the 8 nm ones. The highest temperature of 500°C used for NP formation was found to significantly increase the $\langle R_{Total}\rangle_{600-800\,\mathrm{nm}}$ and decrease the $\langle R_{Diff}\rangle_{600-800\,\mathrm{nm}}$ of the 12 nm samples, mostly due to the spectral shift of the plasmonic resonance towards the NIR. A high value of diffuse reflection was obtained for the PBR with NPs formed from 8 nm of Ag annealed at 500 °C for 1 h, despite its rapid decrease of performance with increasing annealing time due to the possible out-diffusion of silver.

The optical performance of the PBRs analyzed in this section will be affected when they are implemented in solar cells, since the scattering properties of the NPs plus mirror system change when they are placed in the

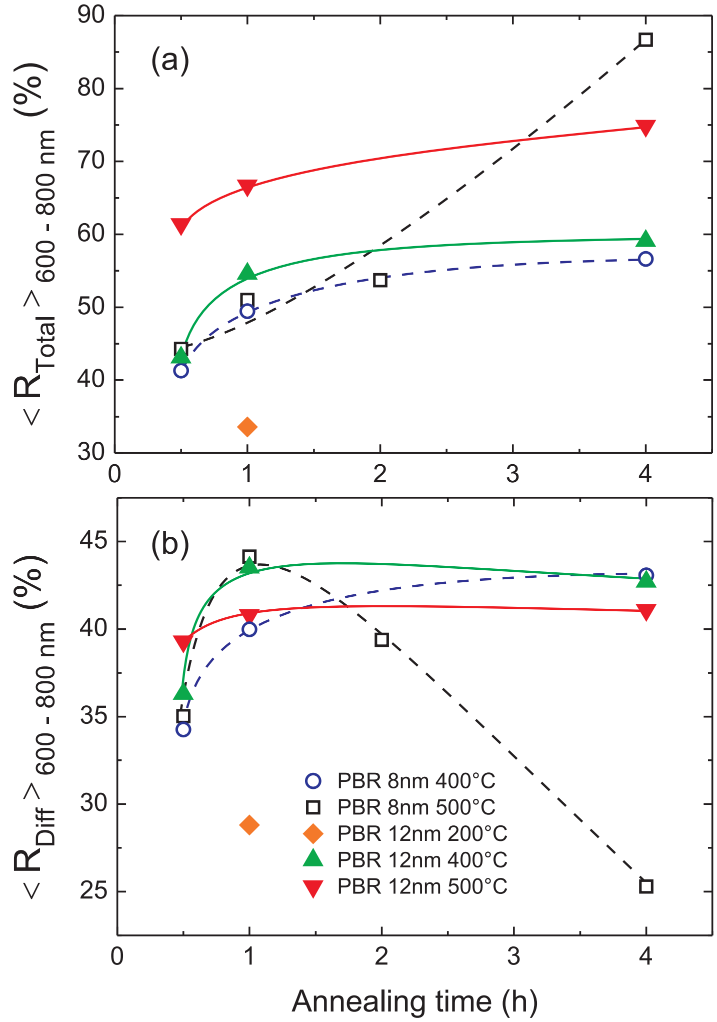

Figure 4.7: Annealing time dependence of the average (a) total and (b) diffuse reflection in the 600 − 800 nm wavelength range for the plasmonic back reflectors (PBRs) with NPs formed from 8 (open symbols) and 12 nm (solid symbols) thick Ag films annealed at 200, 400 and 500°C. The absolute differences in $\langle R_{Total} \rangle_{600-800\,\mathrm{nm}}$ and $\langle R_{Diff} \rangle_{600-800\,\mathrm{nm}}$ observed between PBRs fabricated in distinct batches, with the same fabrication parameters, were below 2.3%, which gives main error associated to the data points in the plots.

vicinity of a high refractive index material (silicon). The cell material generates additional back-reflected fields interacting with the NPs which can alter their polarizability and, consequently, the PBRs scattering spectra. Despite these effects, in previous studies of PBRs implemented in thin film Si cells [2, 12, 13] it has been observed that the reflection spectra of the PBR structures alone correlate with the light extinction and quantum efficiency enhancement spectra achieved when they are coupled to the cells. As such, the results presented in Fig. 4.7 constitute reasonable quantities for a preliminary evaluation of the PBRs, to determine the preferential fabrication parameters.

4.1.2 Solar cell fabrication and characterization

To investigate the plasmonic light trapping in TF silicon solar cells, several PBRs with distinct optical performance were selected as substrates for the fabrication of n-i-p a-Si:H solar cells. The PBRs were characterized optically prior to the deposition of silicon and their average reflections are plotted in Fig. 4.7. Reference cells without NPs were fabricated in the same process on substrates containing only the flat Ag mirror and the AZO layers.

The n-i-p a-Si:H solar cells were deposited on the PBRs at a temperature of 170°C using a multi-chamber plasma-enhanced chemical vapor deposition (PECVD) system, followed by the sputter deposition of the indium doped zinc oxide (IZO) front contact. Finally, in order to improve the electrical performance, all the cells are annealed in low vacuum at 150°C for 2 h. The structure of the a-Si:H n-i-p solar cells deposited on the PBRs is schematically shown in Fig. 4.8(a) and in cross SEM (20° tilt angle) in Fig. 4.8(b). It consists of a stack of 33 nm n-type amorphous, 300 nm intrinsic amorphous, 13 nm p-type nanocrystalline and 7 nm p-type amorphous Si:H. For the front contact, a 240 nm thick indium doped zinc oxide (IZO) layer was used.

The devices are characterized by measuring the J-V curves, under one sun illumination (AM1.5G, $100\,\mathrm{mWcm^{-2}}$) in a Spire Sun Simulator 240A, and by evaluating the external quantum efficiency (EQE) in short-circuit condition in the $350 - 800$ nm wavelength range with a 10 nm wavelength interval between each measured data point. The open-circuit voltage (V_{oc}) and fill factor (FF) of the cells are extracted from the J-V curves, and the short-circuit current density (J_{sc}) is determined from the integration of the EQE convoluted with the AM1.5G photon flux.

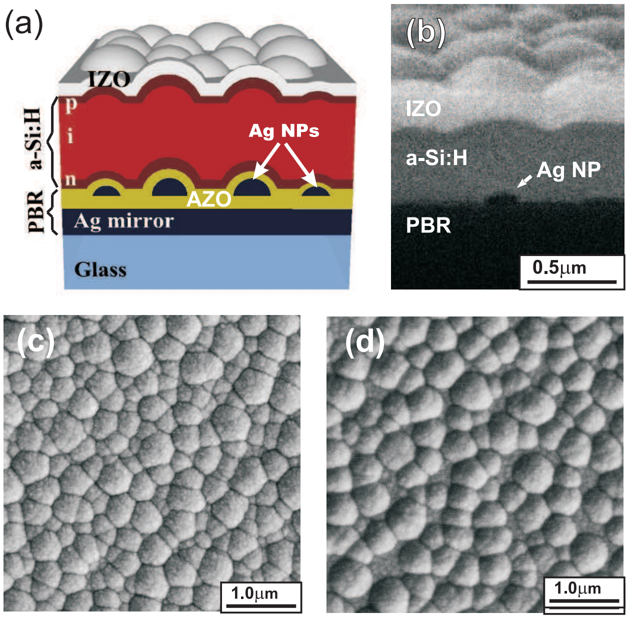

Figure 4.8: Structure of a-Si:H n-i-p solar cell with plasmonic back reflector (PBR) shown (a) schematically and (b) in SEM cross section at a tilt angle of 20°. (c-d) SEM of the honeycomb-like surface texture of the top IZO layer of the devices fabricated with NPs formed from 8 and 12 nm thick Ag films annealed at 500°C for 1 h and 400°C for 4 h, respectively.

The conformal growth of silicon and IZO on top of the NPs resulted in the random honeycomb-like surface texture shown in Figs. 4.8(c-d) for two of the best-performing PBRs, 8 nm 500°C 1 h (c) and 12 nm 400°C 4 h (d), respectively. The surface of the cell with NPs formed from 8 nm of Ag is denser and exhibits smaller features, in agreement with the NPs morphology observed by SEM. The rms roughness determined by atomic force microscopy (AFM) was of 25 and 28 nm for the top surface of, respectively, the 8 and 12 nm cells of Figs.4.8(c) and 4.8(d).

4.1.3 Photocurrent enhancement

The EQE characteristics of the cells fabricated on these two PBRs and on a flat BR reference are shown in Fig. 4.9. Both PBRs provide a broadband EQE enhancement relative to the reference cell, not only in the red-NIR

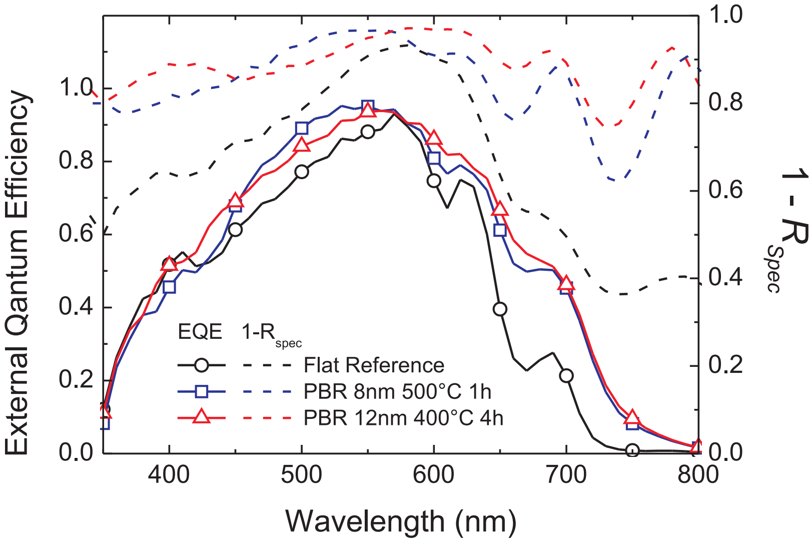

Figure 4.9: External quantum efficiency (EQE) and $1 - R_{Spec}$ (R_{Spec} is the specular reflection at normal incidence) curves of best performing solar cells, fabricated on PBRs with NPs formed from 8 and 12 nm thick Ag films, in comparison with a reference cell with a flat back reflector only.

light trapping window (600-800 nm) but also in the blue-green spectral range (430-570 nm). Therefore, two distinct light trapping mechanism contributing to the overall enhancement can be identified. The improvement in the short wavelength range originates from the texture of the solar cells front surface, as in this spectral region all the incident light is absorbed in the Si layers during the first pass without interacting with the NPs. The light coupling, and hence the antireflection properties provided by the honeycomb-like texture are more efficient than the one given by reference flat IZO layer [14]. An important insight on the light trapping effects is provided by the cell's reflection, which describes the absorption in the device. As the dimensions of the solar cells fabricated in this work were below the minimum measurable sample size allowed by the integrating sphere setup used for optical characterization, the specular reflection at normal incidence (R_{Spec}) has been determined and plotted together with EQE curves in Fig. 4.9. This

Table 4.1: Electrical parameters of the solar cells fabricated on two PBRs with NPs formed from 8 and 12 nm thick Ag films, in comparison with the reference cell deposited on a flat back reflector (EQE curves shown in Fig. 4.9). The $J_{sc\ 600-800\,\mathrm{nm}}$ is the current density obtained from integrating the EQE curve, convoluted with the AM1.5G photon flux, only in the $600-800$ nm wavelength range.

	V_{oc} V	J_{sc} mA/cm^2	$J_{sc\ 600-800\,\mathrm{nm}}$	FF	η %
Flat reference	0.848	12.88	3.60	0.396	4.33
PBR 8 nm 500°C 1 h	0.862	15.48	5.52	0.390	5.20
PBR 12 nm 400°C 4 h	0.854	15.75	5.85	0.403	5.42

shows a reasonably good spectral correlation between $1-R_{Spec}$ and EQE illustrating the antireflection properties of the cells surface texture. However, as the diffuse component of the reflection is neglected, the $1-R_{Spec}$ curves give an overestimation of the total absorption in the cells, which might be significant in the red-NIR range of low absorption in a-Si:H.

For wavelengths longer than 600 nm, the EQE enhancement can have contributions from both the surface texture and the plasmon-assisted scattering from the Ag NPs; and the impact of the two mechanisms cannot be measured separately. However, previous computational studies indicate that moderate surface roughness should only significantly increase absorption in Si thin films for wavelengths roughly below 500 nm [15], whereas Ag NP structures can provide pronounced absorption enhancement only at longer wavelengths [10, 11]. Therefore, and considering the diffusion properties of the PBRs analyzed in section 4.1.1, the main light trapping effect leading to the observed photocurrent gains in the red-NIR range (600-800 nm) is attributed to LSP-assisted scattering.

The electrical parameters of the cells are listed in Table 4.1. The J_{sc} value of 15.75 mA/cm^2 and V_{oc} of 0.85 V measured for the devices fabricated on the PBR with 12 nm Ag, annealed at 400°C for 4 h, are among the highest values reported for plasmonic light trapping in a-Si:H solar cells with self-assembled NPs [2, 12, 13] due to the high photocurrent enhancement provided by such PBR, without degrading the V_{oc} of the cells. A total J_{sc}

enhancement of 22.3% and 62.5% for the J_{sc} over the $600 - 800\,\mathrm{nm}$ range was achieved.

The devices suffer, however, from low values of fill factor, caused by both high series resistance (R_S) and low shunt resistance (R_{SH}). The high R_S should be mainly caused by the relatively high resistivity ($7.2 \times 10^{-4}\,\Omega\mathrm{cm}$) of the IZO top contact, compared to that($10^{-4}\,\Omega\mathrm{cm}$) of state-of-art TCOs [16], and possible defects in the TCOs and doped Si layers. The low R_{SH} should result from process-induced shunting paths in the n-i-p junction created during the PECVD deposition, and possible damaging of the p-type layer during the sputtering of IZO. For these reasons, only moderate conversion efficiencies (η) were attained. Nevertheless, it is important to underline that no deterioration of the FF was observed between the reference and the NP-enhanced cells. Even though the solar cell fabrication conditions are not fully optimized, it is demonstrated that the implementation of the PBRs leads to a considerable increase of the photocurrent.

4.1.4 Correlation between optical and electrical properties

Figure 4.10 depicts the relation between the optical performance of PBRs, in terms of $\langle R_{Diff} \rangle_{600-800\,\mathrm{nm}}$, and the J_{sc} enhancement in the corresponding wavelength range, based on more than 40 solar cells. Each symbol corresponds to the average value of a set of 4 to 6 cells, while the error bars indicate the maximum and the minimum enhancement of the set. A linear relation between the $J_{sc\ 600-800\,\mathrm{nm}}$ enhancement and $\langle R_{Diff} \rangle_{600-800\,\mathrm{nm}}$ was found for both 8 and 12 nm PBRs with approximately the same slope (2.75 ± 0.09 and 2.8 ± 0.4, respectively). The 8 nm PBRs, however, show systematically lower enhancement than the 12 nm ones originating mainly from the lower total reflection, and hence higher parasitic absorption, in the 8 nm structures. Furthermore, the 8 nm samples exhibit lower values of R_{Diff} over the $600 - 700\,\mathrm{nm}$ wavelength range, where light trapping effects contribute more pronouncedly to the generated photocurrent. The clear linear relations shown in Fig. 4.10 prove that the EQE enhancement observed in the $600 - 800\,\mathrm{nm}$ region originates mainly from the scattering of light by the NPs sustaining plasmonic resonances. In addition, the extrapolation of the linear fits indicates that values of $\langle R_{Diff} \rangle_{600-800\,\mathrm{nm}}$ higher than 24.5% and 22.5%, respectively for 8 and 12 nm PBRs, are required to compensate the intrinsic losses of light in the NPs and produce a positive $J_{sc\ 600-800\,\mathrm{nm}}$ enhancement. This reveals the importance of the trade-off between benefi-

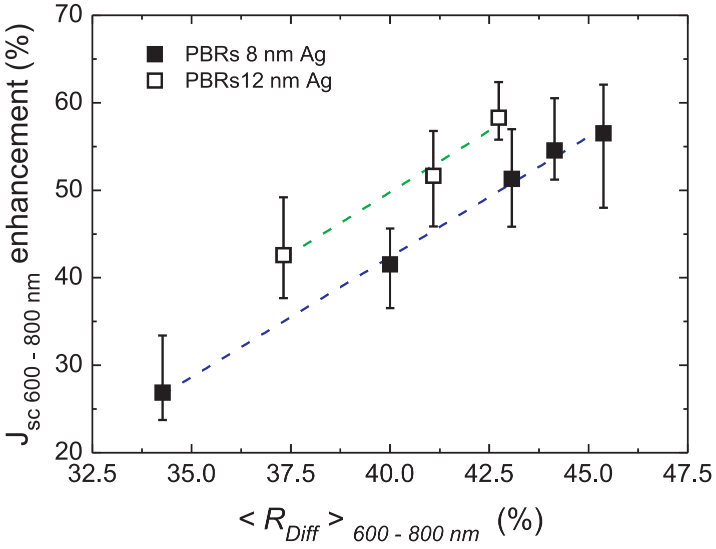

Figure 4.10: Plot of short circuit current density enhancement as a function of the average diffused reflection ($\langle R_{Diff} \rangle$) of the PBRs in the 600−800 nm wavelength range, corresponding to the light trapping window of a-Si:H solar cells.

cial effects of scattering and negative effects of parasitic absorption on the solar cells photocurrent.

The high EQE enhancement, of around 60% in the $600-800$ nm wavelength range, can be attributed to two main factors. First, a more optimized performance of the PBRs, due to improved physical properties (sizes, shapes) of the NP structures, resulting from the investigation of a broader range of fabrication parameters (Ag film thickness, annealing temperature and time). Second, the Ag deposition method employed in this work, using sputtering with relatively high power and low pressure instead of the commonly-used thermal evaporation process [2, 12, 13, 17, 18], enabling the growth of precursor films with better crystallinity and fewer number of voids due to the high kinetic energy of sputtered species and, thus, higher surface mobility of adatoms [19–21]. This results in less dissipative interactions with defects and grain boundaries (parasitic absorption) at the plasmonic resonances due to the improved material quality of the self-assembled NPs [6].

4.1.5 Conclusions

In conclusion, optical properties of plasmonic back reflectors with self-assembled silver nanoparticles, formed by solid-state dewetting with distinct fabrication conditions, and their impact on the performance of n-i-p a-Si:H solar cells is reported. The method used in this work to deposit the precursor Ag films by sputtering is distinct from the conventionally-used thermal evaporation process. This should allow a better crystalline quality of the NPs material and thus less energy dissipation at the LSP resonances. The PBRs produced in this way provide broadband quantum efficiency enhancement in the visible and NIR range which is attributed both, to the cells front surface texture induced by the NPs shape, and to the plasmon-assisted scattering.

The best-performing solar cells were obtained with a PBR containing NPs formed from a 12 nm thick Ag film annealed at 400°C for 4 h. Such PBR provided a pronounced 22.3% enhancement of J_{sc} (and 62.5% for the photocurrent in the $600 - 800$ nm range), which allowed the achievement of high absolute values of $J_{sc} = 15.75\,\mathrm{mA/cm^2}$ and $V_{oc} = 0.854\,\mathrm{V}$ relative to those reported so far for plasmon-enhanced a-Si:H solar cells. Although the devices suffer from low values of fill factor, no deterioration occurs due to the presence of the NPs since the PBR-enhanced cells have similar FF as the reference cells without particles.

The EQE response of more than 40 solar cells, deposited on distinct types of PBRs, was analyzed and correlated to the previously-measured light scattering properties of the PBRs. This allowed the determination of a linear relation between the average diffuse reflection of the PBRs, in the $600 - 800$ nm wavelength range, and the corresponding J_{sc} enhancement. This reveals that the identification and the minimization of the parasitic absorption in the NPs is a crucial point for further improvement of plasmonic light trapping.

4.2 Attempt on implementation of plasmonic light trapping in the industrial a-Si/μc-Si double junction solar cells

4.2.1 Sample preparation

Customized double junction a-Si/μc-Si solar cells were obtained from the industrial partner 3SUN. The investigated device structure, shown schematically in the inset of Fig. 4.11, consists of a randomly textured fluorine doped tin oxide (FTO) front contact, 300 nm thick a-Si:H p-i-n top cell, 1.7 μm thick μc-Si:H p-i-n bottom cell and 1.7 μm thick boron doped zinc oxide (BZO) back contact. Active layers were deposited by the production line plasma enhanced chemical vapor deposition system (PECVD) in superstrate configuration. Devices investigated here differ from the standard ones, in which the back contact consists of a thin AZO layer and silver back reflector. Single solar cells were cut from a panel of monolithically integrated devices.

Self-assembled silver NPs were fabricated on the back side of the cells by solid-state dewetting of 12 nm thick Ag film annealed at 200°C for 2 h in the flow of nitrogen. Subsequently, the NPs were covered with a 50 nm thick aluminum doped zinc oxide (AZO) layer and a 100 nm thick silver back reflector.

Thicknesses of Ag and AZO layers were determined using Rutherford Backscattering Spectrometry (RBS, 2.0 MeV He^+ beam) assuming the Ag density of 5.85×10^{22} Ag/cm^3 and Zn density in AZO of 3.22×10^{22} Ag/cm^3. The optical properties were measured using a double beam Varian Cary 500 UV-Vis-NIR spectrophotometer equipped with an integrating sphere. The structural properties of the NPs were investigated by Scanning Electron Microscopy (SEM) - a field emission Zeiss Supra 25 system. The electrical performance of the solar cells were characterized with equipment dedicated for R&D on these specific devices.

4.2.2 Optical characterization

Solar cells investigated here are highly optimized, in terms of silicon layer thicknesses and texture of the front contact, according to the trade-ff between the maximum absorption of sunlight and electrical properties of the materials, as the deposition of silicon on rough substrates results in creation of defects in the films, which acting as non-radiative recombination centers

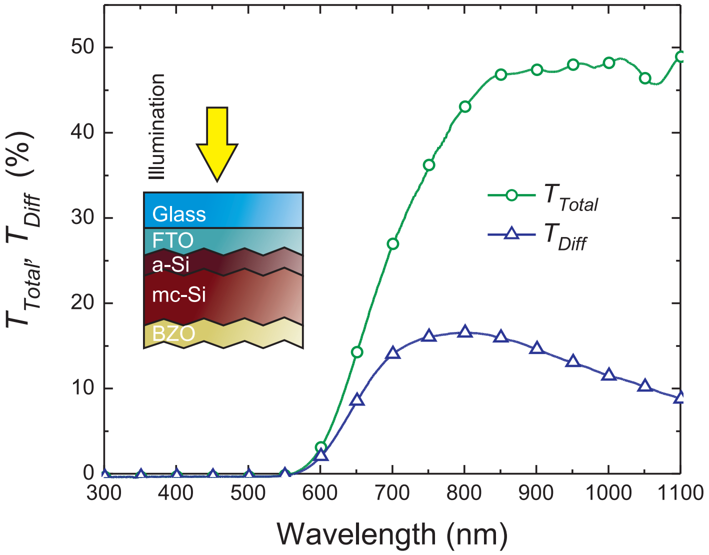

Figure 4.11: Total (T_{Total}) and diffuse (T_{Diff}) transmission of the a-Si/μc-Si solar cell. The inset illustrates schematically the structure of investigated solar cell.

or shunting paths deteriorate the electrical performance of the device. Thus a valid question is whether there is a room for further improvements by enhanced light trapping.

Fig. 4.11 depicts the total and diffuse transmission of the a-Si/μc-Si cell, which is the illumination spectrum for metallic NPs located at the rear side of the cell. About 35% of light in the $800 - 1100$ nm range is transmitted specularly and can be diffused by the NPs for enhanced useful absorption. However, any parasitic absorption would also influence the part of light that has already been diffused at the front interface.

4.2.3 Effect of annealing conditions

The relatively good electrical properties of hydrogenated amorphous and microcrystalline silicon, compared to other non-crystalline semiconductors, originate from the passivation of dangling bonds defects with atomic hydrogen incorporated from the precursor gases (mixture of SiH_4 and H_2) in the PECVD deposition. The hydrogen-silicon bonds break in elevated temperatures, which results in substantial increase of non radiative recombination and reduced conductivity, therefore deposition is usually carried out at temperatures lower than 180°C.

The effect on annealing on the performance of a-Si/μc-Si solar cells was tested in three annealing conditions: at 180°C for 2 h, at 250°C for 15 min, and at 250°C for 2 h. Devices without Ag back reflector were used for the test. In Fig. 4.12, the changes of electrical parameters (J_{SC}, V_{OC}, FF, efficiency, R_S, and R_{SH}) between as deposited and annealed state are plotted for each annealing condition. The J_{SC} and V_{OC} were found to decrease with increasing thermal budget. In particular long annealing at 250°C resulted in a drop of 0.18 V in V_{OC} and 2.2 mA/cm^2 in J_{SC}. Nonetheless, an unexpected increase of FF originating an overall increase of efficiency was found for annealing at 180°C - the temperature close the deposition condition. The improvement of FF results clearly from the decrease of series resistance, which in addition has a stronger impact than the simultaneous decrease of parallel resistance. The increase of FF obtained for short annealing at 250°C cannot be, however, fully trusted as it originated an unproportionally small decrease of R_{SH} in comparison with the other two samples.

4.2.4 Implementation of NPs

The implementation of metallic NPs, formed from 12 nm thick Ag film annealed at 180°C for 2 h, resulted in decrease of external quantum efficiency (EQE) of the a-Si/μc-Si solar cell depicted in Fig. 4.13. This is attributed to significant parasitic absorption in the NPs originating from irregularly shaped particles and high surface coverage obtained with low annealing temperature annealing, as shown in the SEM in Fig. 4.13. Additional optical losses can arise from the corrugations of the back reflector resulted from the conformal deposition of AZO and Ag on the NPs, as well as from the rough MOCVD-deposited BZO. The parasitics absorption influences only the bottom as the current produced by the top comes almost entirely from the light absorbed in the first pass through the device. On the other hand, the annealing has a notably more pronounced impact on the top cell, since a-Si:H is more sensitive to hydrogen out-diffusion. Nonetheless, the drop of EQE in the top cell does not fully contribute to the drop of the over-

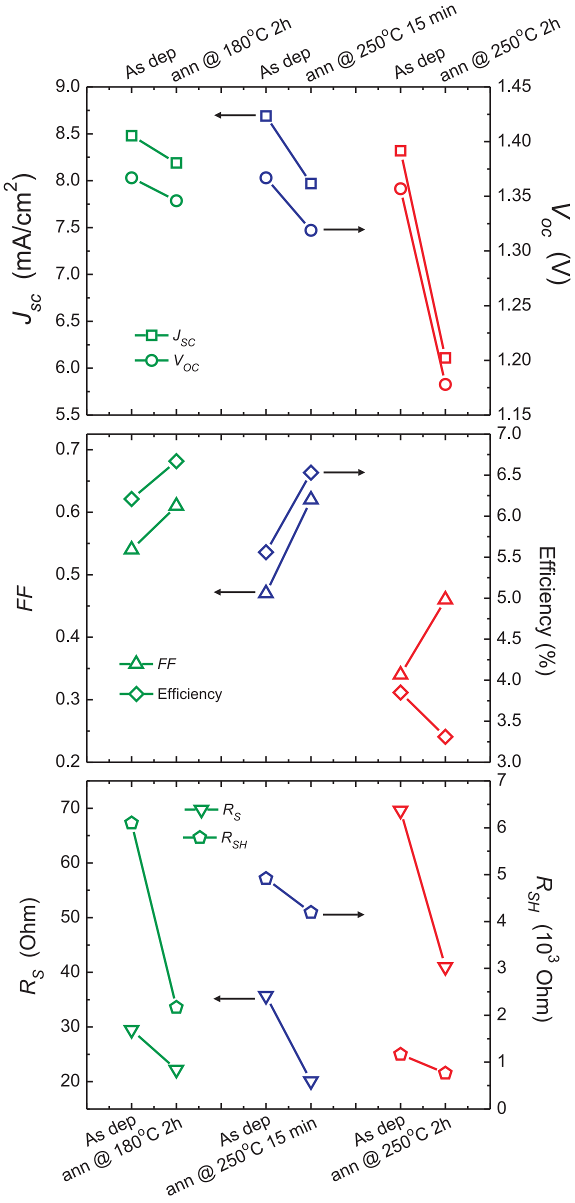

Figure 4.12: Effect of annealing at 180°C for 2 h, at 250°C for 15 min, and at 250°C for 2 h on the performance of a-Si/μc-Si solar cells. For each annealing condition the changes of J_{SC}, V_{OC}, FF, efficiency, R_S, and R_{SH} between as deposited and annealed state are plotted.

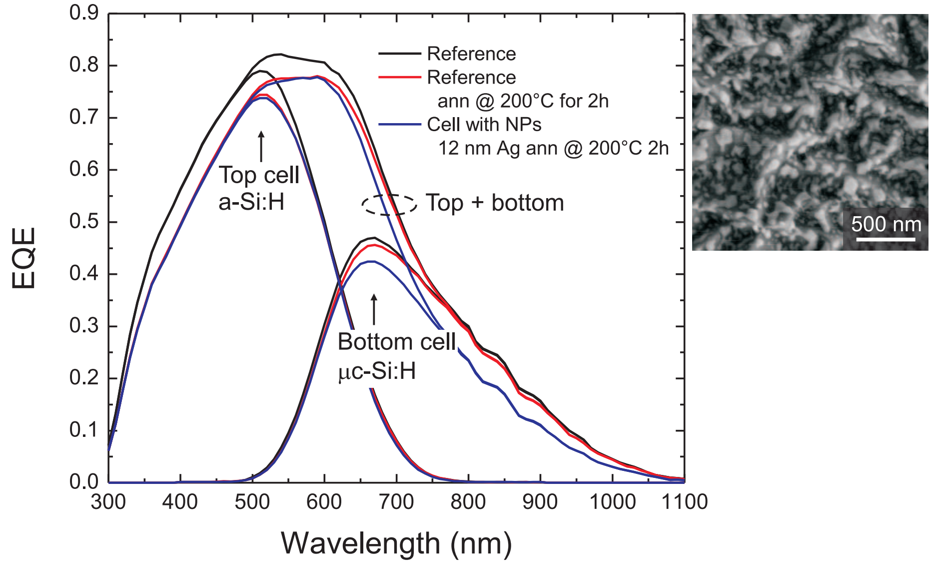

Figure 4.13: External quantum efficiency (EQE) of the a-Si/μc-Si solar cell with NPs formed from 12 nm thick Ag film annealed at 280°C for 2 h in comparison with annealed and not annealed reference devices. The SEM image shows the morphology of the NPs formed on the BZO back contact.

all performance since, due to the current matching requirement, the total current of the reference device was limited by the bottom cell. Therefore, with additional beneficial effect of increased FF compensating the drop of photo-current, the efficiency decreased by a factor of 1.12 for the cell with NPs relative to the not annealed reference.

4.2.5 Conclusions

High parasitic absorption hindered the implementation of plasmonic light trapping in the industrial level a-Si/μc-Si solar cell, which are already well optimized devices with light trapping provided by the random texture of the front contact. It should also be noted that no improvements in performance over the random texture were ever demonstrated with metallic NPs.

Nonetheless, as it is still an ongoing activity, several points should be addressed in the future designs to enable desired enhancements and/or cost reduction. First, the NPs should be located as close to the silicon as possible to ensure efficient coupling of light; second, the AZO cover should be thicker to fallen out the sharp corrugations in the back reflector which acting as hot spots contribute to the parasitic absorption; third, the roughness of the front contact can be reduced in order to gain better quality of silicon films, while exploiting light trapping provided by the NPs. However, the crucial point to minimize both, the parasitic absorption and annealing-related deterioration of the electrical properties of silicon, is to develop a fabrication method allowing for regularly shaped NPs with appropriate sizes in temperature not exceeding 200°C.

References

[1] C. A. Schneider, W. S. Rasband, and K. W. Eliceiri, “NIH Image to ImageJ: 25 years of image analysis,” *Nature Methods*, vol. 9, p. 671675, 2012.

[2] H. Tan, R. Santbergen, G. Yang, A. Smets, and M. Zeman, “Combined optical and electrical design of plasmonic back reflector for high-efficiency thin-film silicon solar cells,” *Photovoltaics, IEEE Journal of*, vol. 3, no. 1, pp. 53–58, 2013.

[3] R. Sesuraj, T. Temple, and D. Bagnall, “Optical characterisation of a spectrally tunable plasmonic reflector for application in thin-film silicon solar cells,” *Solar Energy Materials and Solar Cells*, vol. 111, no. 0, pp. 23 – 30, 2013.

[4] T. L. Temple and D. M. Bagnall, “Broadband scattering of the solar spectrum by spherical metal nanoparticles,” *Progress in Photovoltaics: Research and Applications*, vol. 21, no. 4, pp. 600–611, 2013.

[5] M. J. Mendes, E. Hernández, E. López, P. García-Linares, I. Ramiro, I. Artacho, E. Antolín, I. Tobías, A. Martí, and A. Luque, “Self-organized colloidal quantum dots and metal nanoparticles for plasmon-enhanced intermediate-band solar cells,” *Nanotechnology*, vol. 24, no. 34, p. 345402, 2013.

[6] C. Pahud, O. Isabella, A. Naqavi, F.-J. Haug, M. Zeman, H. P. Herzig, and C. Ballif, "Plasmonic silicon solar cells: impact of material quality and geometry," *Optics Express*, vol. 21, no. S5, pp. A786–A797, 2013.

[7] H. Takele, H. Greve, C. Pochstein, V. Zaporojtchenko, and F. Faupel, "Plasmonic properties of Ag nanoclusters in various polymer matrices," *Nanotechnology*, vol. 17, no. 14, p. 3499, 2006.

[8] G. Xu, M. Tazawa, P. Jin, and S. Nakao, "Surface plasmon resonance of sputtered Ag films: substrate and mass thickness dependence," *Applied Physics A*, vol. 80, no. 7, pp. 1535–1540, 2005.

[9] M. J. Mendes, S. Morawiec, F. Simone, F. Priolo, and I. Crupi, "Colloidal plasmonic back reflectors for light trapping in solar cells," *Nanoscale*, vol. 6, no. 9, pp. 4796–4805, 2014.

[10] K. R. Catchpole and A. Polman, "Design principles for particle plasmon enhanced solar cells," *Applied Physics Letters*, vol. 93, no. 19, 2008.

[11] F. J. Beck, S. Mokkapati, and K. R. Catchpole, "Light trapping with plasmonic particles: beyond the dipole model," *Opt. Express*, vol. 19, no. 25, pp. 25 230–25 241, 2011.

[12] C. Eminian, F.-J. Haug, O. Cubero, X. Niquille, and C. Ballif, "Photocurrent enhancement in thin film amorphous silicon solar cells with silver nanoparticles," *Progress in Photovoltaics: Research and Applications*, vol. 19, no. 3, pp. 260–265, 2011.

[13] H. Tan, R. Santbergen, A. H. M. Smets, and M. Zeman, "Plasmonic light trapping in thin-film silicon solar cells with improved self-assembled silver nanoparticles," *Nano Letters*, vol. 12, no. 8, pp. 4070–4076, 2012.

[14] J. Zhu, C.-M. Hsu, Z. Yu, S. Fan, and Y. Cui, "Nanodome solar cells with efficient light management and self-cleaning," *Nano Letters*, vol. 10, no. 6, pp. 1979–1984, 2010.

[15] P. Kowalczewski, M. Liscidini, and L. C. Andreani, "Light trapping in thin-film solar cells with randomly rough and hybrid textures," *Optics Express*, vol. 21, no. S5, pp. A808–A820, 2013.

[16] S. Calnan and A. Tiwari, "High mobility transparent conducting oxides for thin film solar cells," *Thin Solid Films*, vol. 518, no. 7, pp. 1839 – 1849, 2010.

[17] Z. Ouyang, X. Zhao, S. Varlamov, Y. Tao, J. Wong, and S. Pillai, "Nanoparticle-enhanced light trapping in thin-film silicon solar cells," *Progress in Photovoltaics: Research and Applications*, vol. 19, no. 8, pp. 917–926, 2011.

[18] H. Tan, L. Sivec, B. Yan, R. Santbergen, M. Zeman, and A. H. M. Smets, "Improved light trapping in microcrystalline silicon solar cells by plasmonic back reflector with broad angular scattering and low parasitic absorption," *Applied Physics Letters*, vol. 102, no. 15, 2013.

[19] J. A. Thornton, "High rate thick film growth," *Annual Review of Materials Science*, vol. 7, no. 1, pp. 239–260, 1977.

[20] M. Ohring, "Chapter 4 - discharges, plasmas, and ion-surface interactions," in *Materials Science of Thin Films (Second Edition)*, second edition ed., M. Ohring, Ed. San Diego: Academic Press, 2002, pp. 145 – 202.

[21] ——, "Chapter 9 - film structure," in *Materials Science of Thin Films (Second Edition)*, second edition ed., M. Ohring, Ed. San Diego: Academic Press, 2002, pp. 495 – 558.

Outlook and future perspectives

This thesis are aimed at the implementation of self-assembled plasmonic nanostructures for light trapping in thin film silicon solar cells.

First, the morphology and its correlation with optical properties of nanoparticles fabricated by solid-state dewetting (SSD) process, on glass and aluminium doped zinc oxide (AZO) coted glass substrates, was investigated. Four distinct types of morphology, obtained in specific ranges of fabrication conditions, were defined and summarized quantitatively through a structural-phase diagram of nanostructure formation. The study revealed that elevated annealing temperatures of $\sim 400°$C are essential to obtain regularly shaped NPs with sizes between 100 and 200 nm, according to theoretical predictions appropriate for the application in photovoltaics. It was verified that the main quantity for the correlation between the statistical parameters and the optical properties of the nanostructures is the surface coverage size distribution. The experiments evidenced however unexpectedly high parasitic absorption in the nanostructure indicated as the main obstacle for the applications in light trapping.

The incorporation of NPs in the rear side of silicon films, in two distinct arrangements corresponding to superstrate and substrate configuration solar cells, resulted in considerably high enhancements of absorption in the materials' light trapping windows. The efficiency of light coupling into Si film has been found to (i) increase with NPs' average size and saturate above 180 nm; (ii) to decrease with increasing thickness of the spacer between silicon and NPs and to saturate above 50 nm; and (iii) to be significantly higher for hemispherical Ag NPs fabricated by SSD than for spherical, colloidal Au NPs deposited by wet coating technique. The experimental quantification of useful and parasitic absorption, in the substrate configuration films, was enabled by a combination of PDS and FTPS optoelectronic spectroscopic techniques and revealed that the optical losses in the NPs are insignificant in the $500-730\,\mathrm{nm}$ wavelength range, beyond which they increase rapidly with increasing illumination wavelength. Furthermore, a significant broadband useful absorption enhancement of 89.9% has been achieved for silicon films deposited on plasmonic back reflector (PBR), which can attributed to both the random front surface texture, originated from the conformal growth of Si on top of the NPs, and to the scattering of light by the plasmonic NPs.

The PBR containing NPs formed from a 12 nm thick Ag film annealed at 400°C for 4 h allowed for a pronounced broadband photocurrent enhancement of 22.3% in the a-Si:H solar cells and remarkably high values of $J_{sc} = 15.75\,\mathrm{mA/cm^2}$ and $V_{oc} = 0.854\,\mathrm{V}$ achieved in comparison to those previously reported in the literature for the same type of devices. By analyzing sets of solar cells built on distinct PBRs, it has been shown that the photocurrent enhancement achieved in the a-Si:H light trapping window ($600 - 800\,\mathrm{nm}$) stays in linear relation with the PBRs diffuse reflection.

The attempt on implementation of plasmonic light trapping in the industrial a-Si/μc-Si double junction solar cells resulted in the decrease of quantum efficiency originating from the high parasitic absorption in the irregular NPs fabricated in low temperature due to the limitations set by the degradation of hydrogenated silicon films.

The results presented in this thesis reveal that the parasitic absorption can hinder the implementation of plasmonic NPs for light trapping in solar cells, and that a proper design of the plasmonic nanostructure, controlled by the fabrication parameters, as well as the device structure is essential to achieve desired photocurrent enhancements. Therefore, future work should focus on the minimization of the optical losses, by improved uniformity of the NPs and the quality of material forming the NPs. In addition, development of a fabrication method allowing for regularly shaped NPs with appropriate sizes in temperature not exceeding 200°C is crucial for application in superstrate configuration thin film silicon solar cells.

Once the parasitic absorption can be lowered to values closes to the ones predicted by the theory, plasmonic light trapping with self-assembled NPs can offer a number of advantages: (i) no need for texturing therefore no increase of surface recombination neither creation of defects in the photovoltaic material; (ii) straightforward scalability; (iii) cost-effectiveness, especially in comparison with recently proposed light trapping methods involving expensive fabrication techniques nano-imprint lithography; (iv) full compatibility with the current manufacturing technologies in photovoltaics.

Although this work focuses on thin film amorphous and microcrystalline technology, plasmonic nanstructures fabricated by solid-state dewetting can by applied in different types of solar cell. In particular, plasmonic light trapping might be promising for thin film crystalline silicon devices [1], which implement texturization of the surface.

It has been recently found that plasmonic nanostructures themselves, with no need for the semiconductor material, can be used for solar energy harvesting [2], which opens a new route for application of the self-assembled nanostructures investigated in this work.

References

[1] J. H. Petermann, D. Zielke, J. Schmidt, F. Haase, E. G. Rojas, and R. Brendel, "19transfer using porous silicon," *Progress in Photovoltaics: Research and Applications*, vol. 20, no. 1, pp. 1–5, 2012.

[2] M. T. Sheldon, J. Van de Groep, A. M. Brown, A. Polman, and H. A. Atwater, "Plasmoelectric potentials in metal nanostructures," *Science*, vol. 346, no. 6211, pp. 828–831, 2014.